

AD-A240 151



AEOSR-TR- 91 0743

Contract F49620-88-C-0052

**Alloy Modeling and Experimental Correlation for
Ductility Enhancement in Near Stoichiometric Single
Crystal Nickel Aluminide**

Final Report

Covering the Period 1 March 1988 through 28 February 1991

Prepared for
Air Force Office of Scientific Research
United States Air Force
Bolling Air Force Base, Washington DC 20332-6448

Prepared by
R.D. Field, R. Darolia, D.F. Lahrman, and A.J. Freeman

R. Darolia
Program Manager



GE Aircraft Engines

Engineering Materials Technology Laboratories
Cincinnati, Ohio 45215-6301

91-09721



Approved for public release;
distribution unlimited.

AIR FORCE OF SCIENTIFIC RESEARCH
NOTICE OF TRANSMITTAL
THIS TECHNICAL REPORT IS BEING
FORWARDED TO THE AIR FORCE
OFFICE OF SCIENTIFIC RESEARCH (AFOSR)
AND THE AIR FORCE RESEARCH
LABORATORIES (AFRL)
SEP 12 1991

REPORT DOCUMENTATION PAGE

a REPORT SECURITY CLASSIFICATION Unclassified		1b RESTRICTIVE MARKINGS	
a SECURITY CLASSIFICATION AUTHORITY		3 DISTRIBUTION / AVAILABILITY OF REPORT Approved for public release, distribution unlimited.	
b DECLASSIFICATION / DOWNGRADING SCHEDULE			
PERFORMING ORGANIZATION REPORT NUMBER(S)		5 MONITORING ORGANIZATION REPORT NUMBER(S)	
a NAME OF PERFORMING ORGANIZATION GE Aircraft Engines	6b OFFICE SYMBOL (If applicable)	7a NAME OF MONITORING ORGANIZATION AFOSR/NE	
c ADDRESS (City, State, and ZIP Code) One Neumann Way Cincinnati, Ohio 45215		7b ADDRESS (City, State, and ZIP Code) Bldg 410 Bolling AFB, D.C. 20332-6448	
a NAME OF FUNDING / SPONSORING ORGANIZATION AFOSR/NE	8b OFFICE SYMBOL (If applicable)	9 PROCUREMENT INSTRUMENT IDENTIFICATION NUMBER F49620-88-C-0052	
c ADDRESS (City, State, and ZIP Code) Bldg 410 Bolling AFB, D.C. 20332-6448		10 SOURCE OF FUNDING NUMBERS	
		PROGRAM ELEMENT NO 61102F	PROJECT NO 203675
		TASK NO A1	WORK UNIT ACCESSION NO
1 TITLE (Include Security Classification) Alloy modeling and experimental correlation for ductility enhancement in near stoichiometric single crystal nickel aluminide.			
2 PERSONAL AUTHOR(S) R. Darolia, R.D. Field, D.F. Lahrman, A.J. Freeman			
3a TYPE OF REPORT Final	13b TIME COVERED FROM 88/3/1 TO 91/2/28	14 DATE OF REPORT (Year, Month, Day) 91/7/31	15 PAGE COUNT
6 SUPPLEMENTARY NOTATION			
7 COSATI CODES		18 SUBJECT TERMS (Continue on reverse if necessary and identify by block number)	
FIELD	GROUP	SUB-GROUP	
		Nickel aluminide, ductility, anti-phase boundaries, all electron total energy band structure calculations.	
9 ABSTRACT (Continue on reverse if necessary and identify by block number)			
<p>The objective of this research was to evaluate the applicability of theoretical approaches based on first principles to understand the ductility problem in intermetallic compounds. The predictive approach is based on all electron total energy band structure calculations. Predictions were evaluated on single crystals of NiAl alloys grown at the Engineering Materials Technology Laboratories of GE Aircraft Engines.</p> <p>In the first years effort, calculations of anti-phase boundary (APB) energy in binary NiAl and the effects of ternary alloying additions on APB energy were performed. Experimental work on the effects of Cr and V additions, predicted by the calculations to reduce APB energy, was conducted. Studies aimed at exploiting the stress induced martensite transformation in NiAl to increase low temperature toughness were also conducted. Results from the calculations were found to be in good agreement with known stoichiometric effects on the transformation in binary alloys and suggested potentially beneficial ternary and quaternary alloying additions.</p>			
OVER			
20 DISTRIBUTION / AVAILABILITY OF ABSTRACT <input type="checkbox"/> UNCLASSIFIED/UNLIMITED <input checked="" type="checkbox"/> SAME AS RPT <input type="checkbox"/> DTIC USERS		21 ABSTRACT SECURITY CLASSIFICATION Unclassified	
22a NAME OF RESPONSIBLE INDIVIDUAL Dr. A. Rosenstein		22b TELEPHONE (Include Area Code) 202-767-4984	22c OFFICE SYMBOL AFOSR/NE

In the second year of the program, the investigation of the role of Cr in promoting $\langle 111 \rangle$ slip in NiAl was continued. Experiments to more fully understand this effect were performed. Additional calculations were conducted to clarify the stress induced martensite effect. Calculations aimed at understanding the role of charge density distributions and bond directionality in NiAl were also initiated. Work to determine the role of microalloying in promoting ductility in NiAl was initiated, through calculations of their effect on local charge distribution and experimental work to determine their effect on slip and fracture behavior.

In the third year, investigation of the microalloying effect was continued via calculations and experimental work. Also, studies were performed on the slip and ductility in "soft" orientations, where the preferred $\langle 100 \rangle$ slip vector operates. The nature of the change in slip vector associated with the ductile to brittle transition temperature (DBTT) for the $\langle 001 \rangle$ ("hard") orientation was determined for both stoichiometric NiAl and the Cr containing alloy.

Considerable progress was made in both the theoretical calculations and experimental area to further the understand deformation in NiAl based alloys. Correlations between the calculations and experimental work were made in many areas. However, much more work will be required to bridge the gap between first principles models of electronic structure and engineering properties such as ductility.



Accession For	
NTIS GRA&I	<input checked="" type="checkbox"/>
DTIC TAB	<input type="checkbox"/>
Unannounced	<input type="checkbox"/>
Justification	
EVALUATION	
DESCRIPTORS	
Availability Codes	
Avail and/or	
Dist	Serial
P-1	

I. Introduction

The use of low density intermetallic alloys can significantly increase the thrust-to-weight ratio of the next generation of turbine engines. For example, design studies have shown that the use of an NiAl alloy with 2/3 the density of current Ni base superalloys as turbine airfoils will reduce the rotor system weight by as much as 40%. Programs are being carried out at GE Aircraft Engines (GEAE) to develop NiAl [1], and a technology for growing single crystals of NiAl alloys has been developed.

Current sophisticated computational techniques in solid state theory have yielded encouraging results in predicting phase stability as well as quantitative thermodynamic data. The determination of anti-phase boundary (APB) and stacking fault energies, in addition to modeling of grain boundaries and the effects of alloying additions, can greatly increase our understanding of the behavior of the intermetallic compounds. Also, calculated values of elastic constants for alloys and information about the directionality of bonding can give insights into the formation energies and Peierls stresses for dislocations. The most advanced modeling approach involves all electron band structure calculations, in which the electronic structure of a metal or alloy is determined completely from first principles. These calculations yield quantitative thermodynamic data, as well as information on the stability of the compound through investigation of the total energy of the system and the role of the electron density of states (DOS) near the Fermi level. This approach can be used to predict not only the stability of one structure type over another for a particular stoichiometry, but also the effect of alloying on lattice stability and site occupancy of ternary alloying elements. Some examples of the application of this technique are in the determination of anti-phase boundary energy (APBE) in Ni₃Al [2] and phase stability in Al₃X systems [3].

This investigation was performed to assess the predictive capabilities of theoretical models in determining mechanical behavior of intermetallic compounds and to refine these models based on correlation with experimental results. A coordinated effort between the theorists and experimentalists is required to solve the complex problems associated with intermetallics. This report summarizes the results from all three years of this program.

II. Approach

A unique feature of the technical approach was the use of single crystals of NiAl alloys. The use of single crystals provides several distinct advantages: 1) it eliminates complications associated with grain boundaries, so that the effect of alloying modifications on the intrinsic properties of NiAl can be unequivocally understood, 2) it provides information on single crystals oriented in certain specific crystallographic orientations to understand orientation dependence of properties, and 3) it lends an insight into bond directionality of crystallographic structures of interest. Single crystals specimens having specific crystallographic directions such as $\langle 001 \rangle$, $\langle 011 \rangle$, or $\langle 111 \rangle$ were machined from single crystals grown in the $\langle 001 \rangle$ orientation. These were tested in tension

and compression at various temperatures and the deformation structures evaluated using analytical electron microscopy (AEM) techniques.

The modeling technique, "all electron total energy band structure calculations", is being developed and used at Northwestern University on binary, ternary, and some quaternary NiAl alloys. The calculations have addressed four aspects of the ductility problem in NiAl. The first is concerned with the energy of the anti-phase boundaries which would need to be created in order to form $\langle 111 \rangle$ superdislocations in the NiAl structure. Specifically, calculations have been made on the effect of APB formation on $\{110\}$ and $\{112\}$ planes on the electronic structure of the compound using a supercell technique. These two sets of planes were chosen since they are the most common slip planes in the disordered bcc structure and the latter is observed in low temperature compression of $[001]$ oriented NiAl specimens. Second, the relative stability of the B2 NiAl structure and the $L1_0$ martensite structure has also been calculated to address the martensitic reaction in NiAl as a possible source of room temperature toughness. Third, the effect of charge distribution and bond directionality in NiAl has been addressed, based on recent work in the TiAl and Ti_3Al compounds [4,5]. Fourth, the effect on local electronic structure of certain elements, found to improve ductility in "soft" oriented NiAl alloys when added at low levels, was investigated.

III. Background

The need for high temperature, low density materials for applications in aircraft engines has led to renewed interest in intermetallic compounds. Although many of these compounds have high melting temperatures and low specific gravities, they often suffer from lack of low temperature ductility. NiAl, with the CsCl (B2) structure, is considered a good candidate for development partially due to its simple crystal structure and small slip vectors. The shortest lattice translation vector in the B2 structure is $\langle 100 \rangle$, which does not provide enough independent slip systems to satisfy Von Mises criterion for ductility in polycrystalline material. In single crystals, there is no resolved shear stress on systems with the $\langle 100 \rangle$ slip direction for $\langle 001 \rangle$ oriented specimens. Superpartials based on the bcc $1/2\langle 111 \rangle$ Burgers vector, separated by an anti-phase boundary (APB), are possible and do represent the majority of dislocations in some B2 compounds (eg. CuZn [6,7]). Several attempts have been made to predict active slip systems in B2 compounds using input parameters such as ordering temperature (to calculate APB energy), elastic constants, and atomic radii [8-11]. All of these studies predict that the $\langle 100 \rangle$ slip direction is preferred in NiAl.

The predominance of $\langle 100 \rangle$ slip in NiAl has been well established [9,12-15]. The preferred slip plane for the compound is generally considered to be $\{110\}$ at room temperature. Most investigators have considered the $\{100\}$ to be an alternate slip plane with a slightly higher critical resolved shear stress (CRSS) [13-15]. However, no systematic study of CRSS values for the two planes can be found in the open literature. Due to the very high critical resolved shear stress (CRSS) for $\langle 111 \rangle$ versus $\langle 100 \rangle$ slip, $\langle 111 \rangle$ slip has been clearly demonstrated only when

compression testing is performed along a $\langle 001 \rangle$ axis (where the Schmid factor for $\langle 100 \rangle$ slip is zero) and only at or below room temperature [16]. Even then, bending stresses and local inhomogeneities can result in kinking, which has been established as a $\langle 100 \rangle$ slip phenomenon [17,18]. Increased ductility at higher temperatures in $\langle 001 \rangle$ oriented single crystals has been generally considered to result from either the operation of $\langle 111 \rangle$ and/or $\langle 110 \rangle$ slip [13,15] or to the activation of climb mechanisms involving $b = \langle 100 \rangle$ dislocations [12]; however, no conclusive evidence for either mechanism has been presented.

An possible alternative means of deformation in NiAl is associated with the martensitic transformation which occurs in Ni rich compositions [19-22]. Strains from a stress induced transformation or deformation within the martensitic phase itself may be able to accommodate deformation in an NiAl alloy.

IV. Results

A. Results From Calculations

1. APB Energy

One of the factors believed to limit ductility in NiAl is the availability of only three independent slip systems, with the $\langle 100 \rangle$ slip direction, and thus the failure to meet Von Mises criterion of a minimum of five independent systems to accommodate an arbitrary shape change. The introduction of dislocations with $\langle 111 \rangle$ Burgers vectors (the slip direction for the disordered bcc structure on which the B2 structure of NiAl is based) would relieve this limitation and therefore has been one of the goals of this study on ductility enhancement in NiAl. Lowering of the anti-phase boundary energy (APBE) could result in the formation of $\langle 111 \rangle$ superdislocations, two $1/2\langle 111 \rangle$ superpartials separated by an APB, as observed in other B2 systems such as CuZn [6,7]. Reduction of the formation energy of $\langle 111 \rangle$ superdislocations would provide an ample number of slip systems and, provided the Peierls stress was low enough to give sufficient mobility, might well promote ductility in NiAl.

APBE values for $1/2\langle 111 \rangle\{110\}$ and $1/2\langle 111 \rangle\{112\}$ APB's in stoichiometric NiAl were calculated using the linear muffin-tin orbital (LMTO) method. Calculations were performed for supercells containing 4, 6, 8 and 10 layers of $\{110\}$ and $\{112\}$ planes, corresponding to unit cells with 8, 12, 16, 20, atoms, respectively. Two APB planes were required in each supercell in order to establish a repeatable unit. The distance between the two APB planes increased with increasing cell size. In these first calculations, no relaxation of the atomic positions was allowed at the APB interface. The cells for the $1/2\langle 111 \rangle\{112\}$ APBE calculations are monoclinic, while those for the $1/2\langle 111 \rangle\{110\}$ are orthorhombic. The quite different first and second nearest neighbors in the $1/2\langle 111 \rangle\{110\}$ and $1/2\langle 111 \rangle\{112\}$ APB's and in the original B2 cell make the lattices behave differently.

Calculations were also performed on the B2 structure using the normal cubic two atom unit cell as well as three orthorhombic and three monoclinic cells based on the APB cells, but with the APB defect omitted. Schematics of the six layer cells with and without the $1/2\langle 111 \rangle\{110\}$ APB are shown in Figure 1. Differences in the calculated results from the seven different cells are within the precision of the method, confirming the credibility of the APBE calculations. By comparing the total energy for the cells with and without the APB, an APBE of around 880 mJ/m² was calculated (listed in Table I). As the distance between the APB layers is increased, the APBE values decrease gradually. This result is expected due to diminished interactions between the APB layers. To test convergence of the calculations, APBE's calculated using 8 layers and 10 layers for the $1/2\langle 111 \rangle\{112\}$ case were compared and the value was found to be only slightly smaller for the larger cell. This suggests that the interactions between two APB's only extend for a few atomic layers. After this, two consecutive APB's can be considered to be totally independent. Thus, values obtained for the 10 layer supercell should represent the extrapolated values, ie. those of a single APB in an infinite lattice.

Table I Calculated APBE Values as a Function Of Supercell Size

number of layers in supercell	<u>APBE (mJ/m²)</u>	
	$1/2\langle 111 \rangle\{110\}$	$1/2\langle 111 \rangle\{112\}$
4-layers	1130	1050
6-layers	1000	950
8-layers	880	890
10-layers	880	885

The APBE values calculated for NiAl are extremely high when compared to the experimentally determined [23] and calculated [2] values for an APB on a $\{100\}$ plane in Ni₃Al (140 mJ/m²). They are also considerably larger than those calculated for NiAl by other, simpler methods [10,11]. The energies for the $1/2\langle 111 \rangle\{112\}$ and $1/2\langle 111 \rangle\{110\}$ APB's are comparable. As in the APBE case, the energies for breaking a Ni-Al bond $\{1/2(E_{\text{Ni-Ni}} + E_{\text{Al-Al}}) - E_{\text{Ni-Al}}\}$ also exhibit a decreasing trend with increasing number of layers. The bond breaking energies for $1/2\langle 111 \rangle\{112\}$ are slightly larger than those for $1/2\langle 111 \rangle\{110\}$ (13.9 vs. 12.0 mRy for the 8-layer cells). It should be noted that only the first nearest neighbors were considered when calculating the bond breaking energies. Therefore these values are systematically underestimated, since the second and higher nearest neighbors also contribute to bond breaking energy.

An analysis of the results, including calculated layer by layer densities of states (DOS), reveals that the introduction of an APB into the B2 structure greatly increases the height of the strongest higher energy Ni d - Ni d hybridization DOS peak. The hybridization between the Ni d

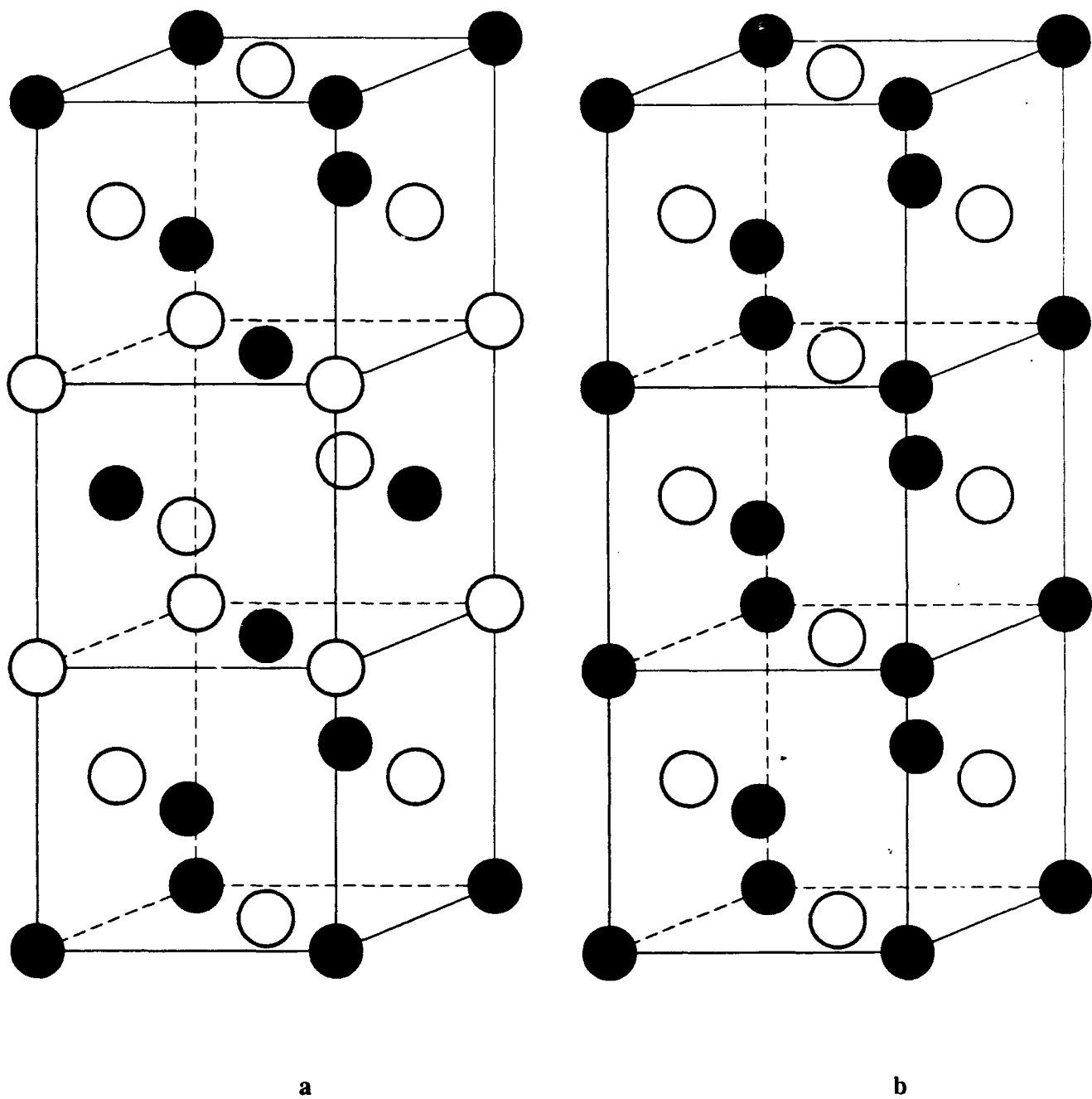


Figure 1. Schematics of the six layer cells used a) with and b) without the $\frac{1}{2}\langle 111 \rangle \{110\}$ APB

and the Al p component is much stronger than the corresponding combination of Ni d - Ni d and Al p - Al p. This gives the very high value for APBE. Either weakening the stronger Ni d - Al p bond or strengthening the Ni d - Ni d and the Al p - Al p bonds should lower the APBE. From a consideration of the DOS, it is expected that the addition of a transition metal with fewer d electrons will shift the d peaks of the transition metal upward, resulting in a weaker transition metal d and Al p hybridization effect. Therefore, the $1/2\langle 111 \rangle\{110\}$ APBE was calculated for alloys in which Al or Ni are partially replaced by Cr, Mn, or V.

For the 4 layer cell, the upper and lower APB's reside on the same plane, resulting in a "double APB". To avoid this situation while still retaining reasonable calculative speed, a 6 layer APB cell was selected for the ternary alloy calculations. Based on the results from the stoichiometric NiAl alloy, it is expected that the $\{110\}$ and $\{112\}$ APBE values will follow the same trends. Therefore, calculations were performed only for the $1/2\langle 111 \rangle\{110\}$ APB. The maximum effect on the APB interface was sought by placing the ternary additions on both APB interface planes to replace either Ni or Al on those two planes.

Table II Calculated APBE Values as a Function of Ternary Alloying Addition

composition	APBE (mJ/m ²)
Al ₆ Ni ₆	1000
Al ₆ Ni ₄ Mn ₂	740
Al ₆ Ni ₄ Cr ₂	510
Al ₆ Ni ₄ V ₂	250
Al ₄ Ni ₆ Cr ₂	250
Al ₄ Ni ₆ V ₂	550

The calculated APBE values are listed in Table II. The results demonstrate that if the ternary addition is substituted for Ni, the APBE is dramatically lower with a ternary addition which has fewer d electrons, as expected from the consideration of the calculated DOS for APB's in pure NiAl. Substitution of the ternary elements for Al leads to different results. Although, the APBE values with ternary additions are substantially lower than that calculated for pure NiAl, alloying with Cr is calculated to have a stronger effect on lowering APBE than alloying with V. From these results, it can be seen that the addition of Cr to the APB interface plane lowers the APBE substantially if Cr is substituted for Al. A comparable decrease in APBE is expected if V is substituted for Ni.

In the calculations described above, the ternary element was placed on the APB plane. The position of the ternary element (ie. with respect to the distance from the APB) has been found to dramatically affect the calculated APB energy. To explore this effect, as well as the effect of

stoichiometry on APB energy in B2 compounds, FeAl and NiAl systems were studied for a 40% Al composition. Excess Ni (Fe) atoms were placed on the second and first (110) layer away from the APB interface (designated $M_{12}Al_8$ (I) and $M_{12}Al_8$ (II), respectively), and on the APB plane itself ($M_{12}Al_8$ (III)).

Results for these calculations are summarized in Table III. The APB energy for stoichiometric FeAl was found to be about 500 mJ/m². This is to be compared with (i) the crude estimate of Mendiratta et al [11] (175 mJ/m²) using Potter's scheme [10], (ii) the unpublished result by Inden (160 mJ/m²) and (iii) the extrapolated value (233 mJ/m²) from the work of Crawford et al [24]. The discrepancy is probably due to the crudeness of the earlier estimates as well as the neglect of atomic relaxation at the APB interface in the current study.

Table III. APB energies for stoichiometric FeAl and NiAl, and for $Ni_{0.6}Al_{0.4}$ and $Fe_{0.6}Al_{0.4}$.

<u>Configuration</u>	<u>APBE (mJ/m²)</u>
Fe ₆ Al ₆	510
Fe ₁₀ Al ₁₀	490
Fe ₁₂ Al ₈ (I)	490
Fe ₁₂ Al ₈ (II)	480
Fe ₁₂ Al ₈ (III)	15
Ni ₁₀ Al ₁₀	880
Ni ₁₂ Al ₈ (I)	870
Ni ₁₂ Al ₈ (II)	870
Ni ₁₂ Al ₈ (III)	55

The calculated APB energies for FeAl from the supercells with 12 atoms (6 layers) and 20 atoms (10 layers) only differ by about 4%, compared to about 12% for NiAl. This indicates a faster convergence rate for the APB energy with respect to the number of layers between two consecutive APB's in FeAl than in NiAl, which probably implies weaker interactions between APB's in FeAl than in NiAl.

By comparing the total energies of the $M_{12}Al_8$ (I,II,III) supercells with and without APB's, three APB energies for $Ni_{0.6}Al_{0.4}$ ($Fe_{0.6}Al_{0.4}$) were obtained corresponding to three different APB locations relative to the excess Ni (Fe) atoms. It is interesting to see the large differences in these three APB energies for both compositions. The APB energies with the first and second choices of site occupancy for excess Ni (Fe) atoms are not changed greatly from the corresponding stoichiometric cases, showing an insensitivity of the APB energy in both FeAl and NiAl to changes in layers other than the APB interface. By contrast, in the last case (III), the APB energy is reduced by more than one order of magnitude from the stoichiometric value; this gives rise to an even greater effect than the reduction of APB energy in NiAl with ternary additions.

These results for the different site occupancy of the excess Ni (Fe) atoms once again emphasize the dominance of the local environment on determining the electronic structure and associated mechanical properties. It is clearly seen that the APB energy depends predominantly on the net changes of the first and second nearest neighbors in the supercell. With greatly reduced APB energies, the activation of $\langle 111 \rangle$ slip is obviously eased in the region where excess Ni (Fe) atoms are located. For the region with composition near stoichiometry, however, the ease of activating $\langle 111 \rangle$ slip remains about the same as that for stoichiometric NiAl (FeAl). Thus, the effect of the excess Ni (Fe) atoms is limited only to the local excess region, as far as the creation of APB's is concerned.

Specimens with the $\text{Ni}_{0.6}\text{Al}_{0.4}$ composition were tested in RT tensile in the [001] orientation. The plastic strain to failure was still negligible ($\sim 0.1\%$) and fracture stresses relatively high (490 MPa). Thus evidence of softening of $\langle 111 \rangle$ slip was not observed; however, anti-site defect hardening is well known to increase strength in Ni rich compositions. No compression testing was performed (to obtain some plastic deformation), so that the presence of $\langle 111 \rangle$ dislocations in [001] oriented specimens could not be determined. Dislocations with $\langle 111 \rangle$ Burgers vectors have been reported in extruded specimens of 58 at% Ni [25] and $\langle 111 \rangle$ slip is widely known to predominate in Fe-40 at% Al.

2. The Martensite Transformation

One possible approach for ductilization of NiAl is to exploit the martensitic reaction which is known to occur in Ni rich alloys within the NiAl stoichiometric range. The phenomenon, termed stress induced martensite (SIM) or stress induced pseudoelasticity (STRIPE), may provide an alternative deformation mechanism at low temperatures [26]. NiAl has the prerequisites for STRIPE and the related shape memory effect (SME): the martensitic reaction is thermoelastic; the parent phase is ordered; and the martensite phase is internally twinned. This effect has been observed in similar alloy systems, having the same B2 parent phase and the same martensitic phase as NiAl. Specifically, NiTi is quite ductile at room temperature, and this ductility is attributed to the STRIPE effect [27]. SME behavior has been reported in Ni-rich NiAl [21,22].

As a first step, the the total energies for NiAl and NiTi were calculated for both the B2 and $L1_0$ martensite crystal structures using the linear muffin-tin orbital (LMTO) method. If the $L1_0$ structure is found to have the lower total energy, it should be stable at 0 K, and a martensitic transformation is predicted. The fact that entropy effects are not included in the calculations means that all of the results apply at 0 K, and the M_s temperature can not be determined directly; however a larger energy difference would imply a higher M_s temperature. The total energies, heats of formation, lattice constants and bulk moduli of NiAl and NiTi (known to transform martensitically at the stoichiometric composition) in both the B2 and martensite structure have been calculated. Results for these calculations are given in Tables IV and V. The B2 structure is predicted to be stable for NiAl. This is expected, since the M_s temperature at the stoichiometric composition is

below 0 K [19,20]. For NiTi, there is some disagreement in the literature with regard to the crystal structure of the martensitic phase. Although originally identified as the L10 structure, more recent investigations have determined it to be the B19 structure [28]. Both structures were considered for NiTi. For either structure, the calculations indicate that the B2 structure is more stable than the martensite structure. This is contrary to experimental evidence, as NiTi does undergo a martensitic transformation [29]. However, the difference in energy between the two structures is smaller for NiTi than for NiAl, indicating that the martensite reaction should be relatively more likely for NiTi than for NiAl (see Table IV).

Table IV Total Energies and Heats of Formation for NiAl and NiTi
(ΔE is with respect to the B2 structure)

<u>Phase</u>		<u>Total Energy</u> (<u>Ry</u>)	<u>ΔE</u> (<u>mRy</u>)	<u>Heat of Formation</u> (<u>kcal/mole</u>)
NiTi	B2	-4740.6882	-	19.8
	L10	-4740.6727	-16	15.0
	B19	-4740.6691	-19	13.9
NiAl	B2	-3520.6066	-	33.8
	L10	-3520.5778	-29	24.8

Table V Calculated and Experimental Lattice Constants, Bulk Moduli, and DOS
Data for NiAl and TiAl

			<u>Lattice Constant</u> (<u>Å</u>)	<u>Bulk Modulus</u> (<u>GPa</u>)	<u>DOS @ Fermi Energy</u> (<u>states/Ry-f.u.</u>)
NiTi	Calc.	B2	3.00	140	37.6
		L10	3.74	160	29.2
	Exper.	B2	3.015 [30]	-	-
		B19	†	-	-
NiAl	Calc.	B2	2.88	210	11.5
		L10	3.65	170	17.3
	Exper.	B2	2.886 [30]	166 [31] 139 [32] . .	15.2 [33]

† Two sets of data are available: $a=2.885$, $b=4.622$, $c=4.120$, $\gamma=96.8^\circ$ [28]
 $a=2.884$, $b=4.665$, $c=4.110$, $\gamma=98.1^\circ$ [34]

The effect of stoichiometry on the relative stabilities of the B2 and L10 structures in NiAl was

also determined. It was found that the stability of the $L1_0$ phase increased with increasing Ni content. For the Ni rich compositions, this is consistent with existing data on the stoichiometric effect on martensitic behavior in this system [19,20]. The difference in total energy between the B2 and $L1_0$ structures, as determined by the band structure calculations, is plotted in Figure 2a. The increasing stability of the martensitic $L1_0$ phase with increasing Ni content mirrors the plot of M_s temperature as a function of stoichiometry presented in Figure 2b. The martensite structure has not been observed in Al-rich alloys. However, it is not possible to maintain the B2 structure for large deviations on the Al-rich side, since other high temperature structures intervene. Also, the deviation from stoichiometry in Al-rich alloys is accommodated by vacancies on the Ni sublattice, whereas the calculations assume a substitutional defect structure. There was an indication of the instability of the B2 structure in the Al-rich region found in the calculations, in the form of lower energies of formation for Al-rich compositions compared to Ni-rich compositions with the same deviations from stoichiometry.

The data for ternary alloy additions are presented in Table VI. Two supercell sizes were used, to obtain two different stoichiometries. For the 4 atom cell (2 B2 unit cells), a 25% ternary alloying addition is simulated, with 50% of the sites of the substituted element filled with the new atomic species. For the 8 atom cell, the ternary addition is equivalent to 12.5% element substitution, or 25% of the designated sublattice sites. Some discrepancies appear to exist between the predicted effects of specific additions for the two cell sizes. For example, a 25% V alloy (substituted for Ni) is predicted to stabilize the $L1_0$ structure, while a 12.5% alloy with the same site substitution is predicted to make the B2 structure even more stable. It is unclear whether this is a real effect, or an anomaly of the calculations.

The effect of ternary elements was considered systematically in the calculations. The data are plotted in Figure 3. For substitution on the Al sublattice, the effectiveness in stabilizing the martensitic structure was found to increase monotonically when moving across the periodic table from Ti to Mn, remain roughly constant through Cu, and decrease again upon increasing the atomic number further. Other rows demonstrated a similar trend, but the first row transition elements were found to be most effective. Thus, most alloying elements are less potent than Ni itself in promoting the martensite transformation. Ternary substitutions on the Ni sublattice (by elements which actually reside on the Ni sites) were not found to be effective.

The most promising result is that for the quaternary alloys. The substitution of both V and Nb onto the Al sites (expected to be their site preference) is found to stabilize the $L1_0$ crystal structure and, therefore, is expected to promote the martensite transformation. However, the concentration of Nb used for the calculations greatly exceeds its maximum solubility (~1-2 at%).

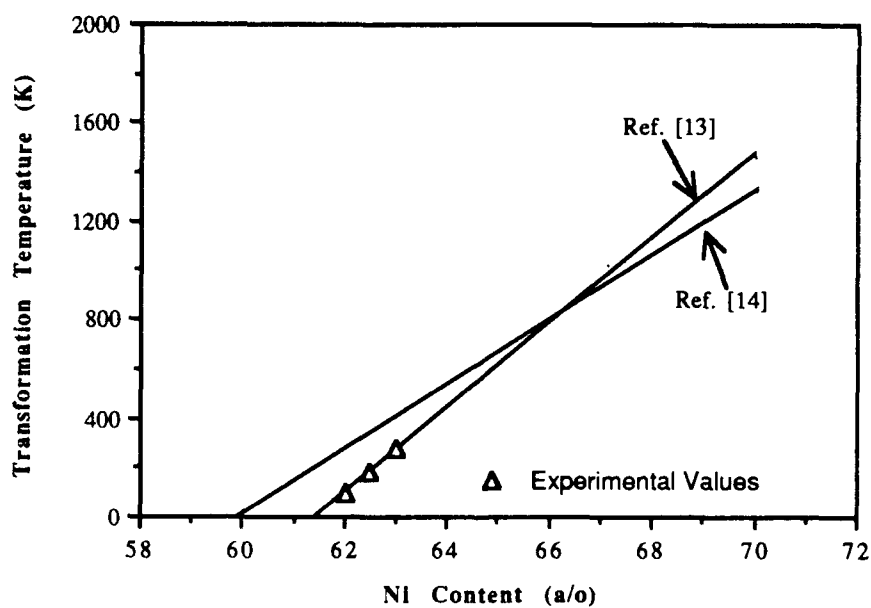
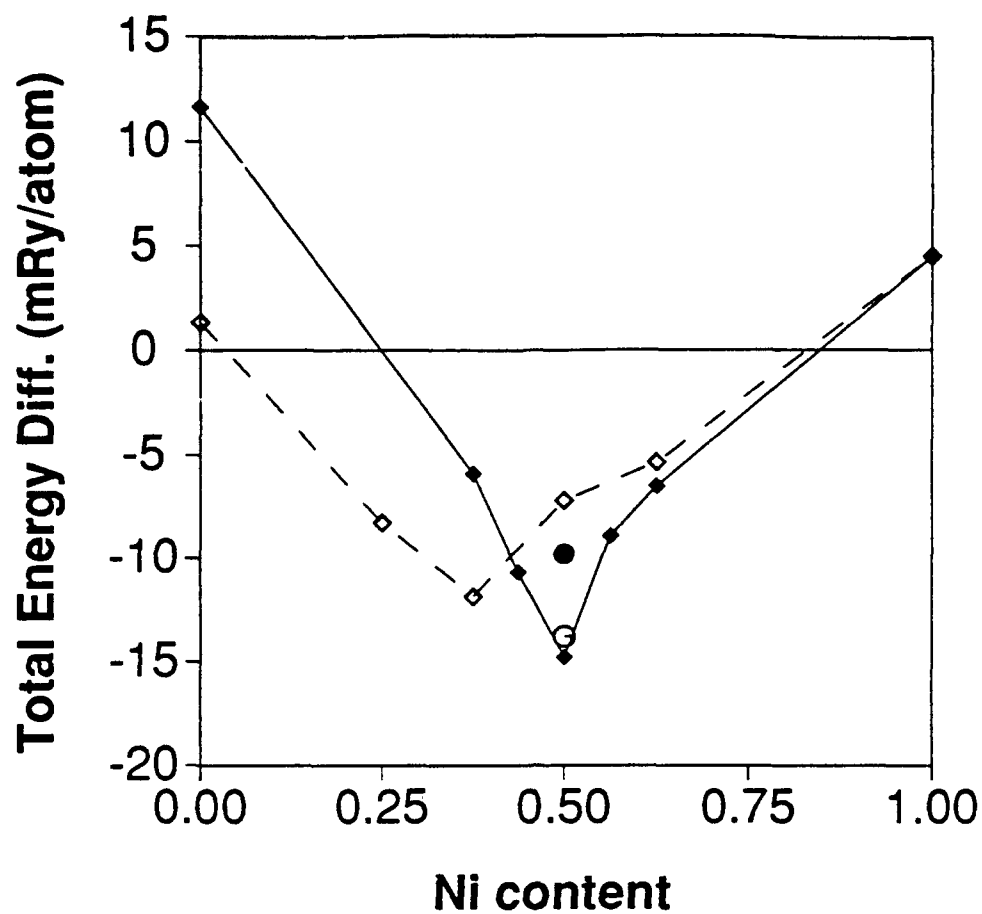


Figure 2. a) A plot of the difference in total energy between the B2 and L1₀ structures as a function of composition in binary NiAl (solid line) and NiTi (dashed line), as determined by the band structure calculations. The results from equi-atomic CoAl (empty circle) and FeAl (filled circle) are also represented. b) Comparison of experimentally determined values taken from the literature of M_s temperatures as a function of stoichiometry with those determined in the current study using ultrasonic measurements.

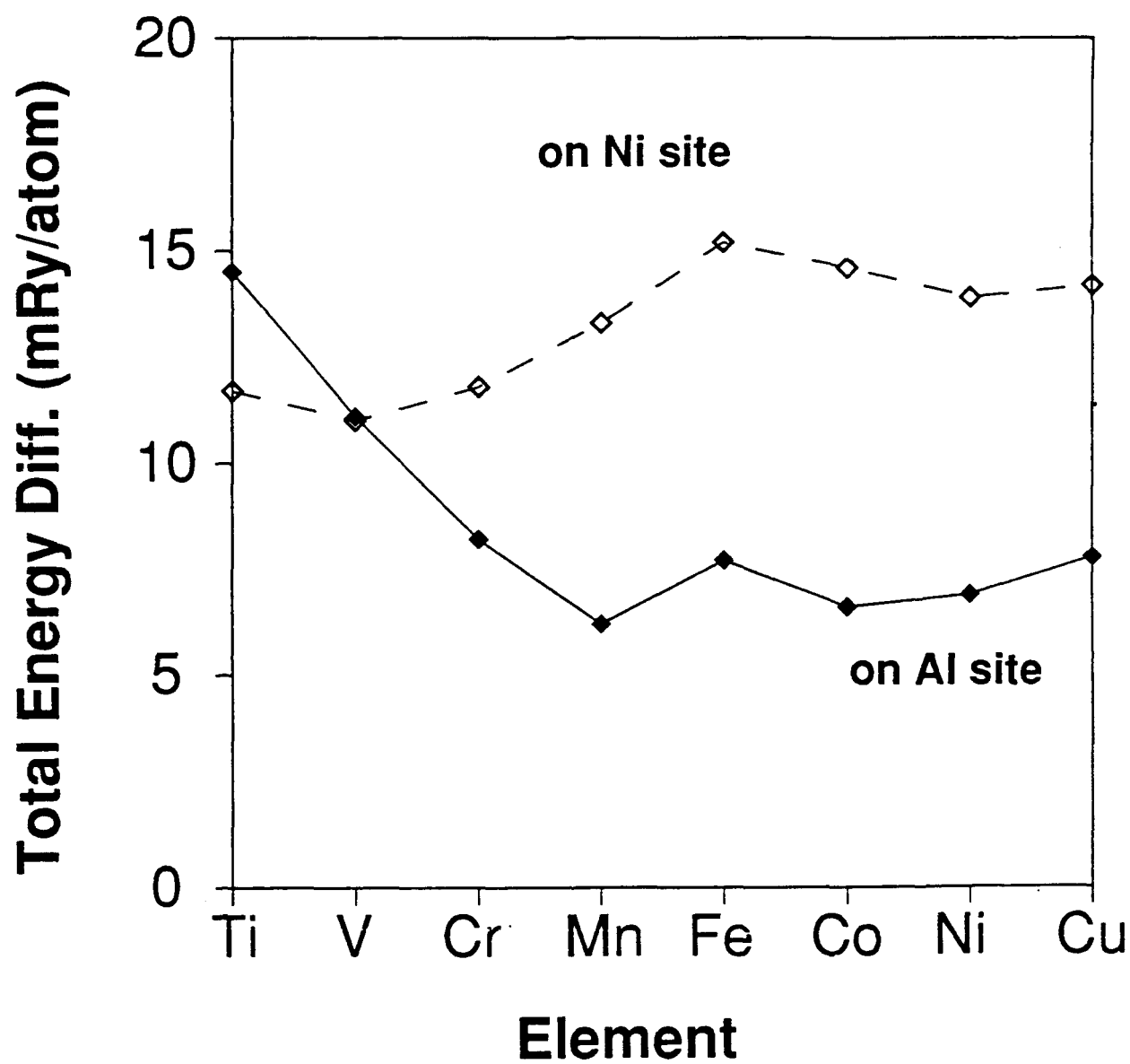


Figure 3. Difference in calculated energies between the B2 and L10 structures in NiAl with ternary additions on the Ni and Al sites.

Table VI Calculated Energies of B2 vs L1₀ Structures at 0 K (B2- L1₀ in mRy)[†]

<u>25% ternary addition on Al site</u>		<u>12.5% ternary addition on Al site</u>	
Ni ₂ TiAl	-18.4	Ni ₄ TiAl ₃	-14.5
Ni ₂ VAl	-11.1	Ni ₄ VAl ₃	-11.1
Ni ₂ CrAl	-0.3	Ni ₄ CrAl ₃	-8.2
Ni ₂ MnAl	-2.3	Ni ₄ MnAl ₃	-6.2
Ni ₂ FeAl	-6.0	Ni ₄ FeAl ₃	-7.7
-	-	Ni ₄ CoAl ₃	-6.6
-	-	Ni ₄ NiAl ₃	-6.9
-	-	Ni ₄ CuAl ₃	-7.8
-	-	Ni ₄ NbAl ₃	-142.8
<u>25% ternary addition on Ni site</u>		<u>12.5% ternary addition on Ni site</u>	
NiTiAl ₂	-5.9	Ni ₃ TiAl ₄	-11.7
NiVAl ₂	2.2	Ni ₃ VAl ₄	-11.0
NiCrAl ₂	-7.3	Ni ₃ CrAl ₄	-11.8
NiMnAl ₂	-29.1	Ni ₃ MnAl ₄	-13.3
NiFeAl ₂	-22.6	Ni ₃ FeAl ₄	-15.2
NiCoAl ₂	-25.4	Ni ₃ CoAl ₄	-14.6
-	-	Ni ₃ NiAl ₄	(-13.9)
NiCuAl ₂	-35.2	Ni ₃ CuAl ₄	-14.2
NiZnAl ₂	-29.7	-	-
NiNbAl ₂	-2.0	Ni ₃ NbAl ₄	-181.4
NiMoAl ₂	-15.5	Ni ₃ MoAl ₄	-160.7
<u>quaternary additions</u>			
Ni ₂ VNbAl ₄			10.4
Ni ₄ VNbAl ₂			3.2

[†]all energies are normalized to a 2-atom unit cell; a positive value indicates that the L1₀ martensite phase is stable

3. Charge Density Calculations

Dislocation formation and movement is governed by the nature of the bonding in the compound. Studies of charge density distributions have led to new insights into dislocation activity in TiAl and Ti₃Al compounds [4,5]. Another high temperature B2 compound which has been found to exhibit relatively high toughness and ductility is RuAl. TEM examination of polycrystalline RT compression specimens of this material has revealed the presence of <110> and <111> dislocations, in addition to the <100> Burgers vector [35].

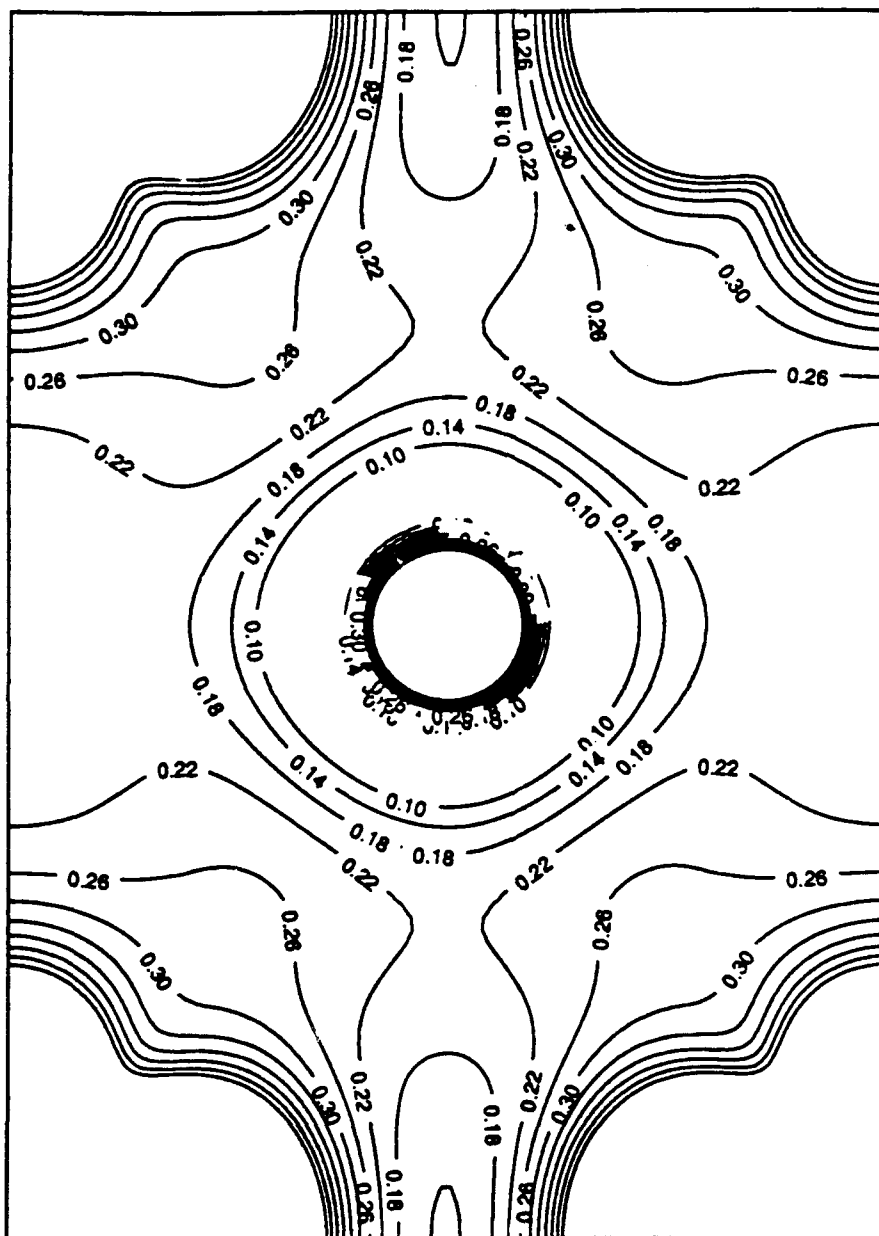
Cohesive properties and APB energies of RuAl and NiAl were studied. The equilibrium lattice constants calculated by the linear muffin-tin orbital (LMTO) method for both compositions were found to be in very good agreement with the experimental values. For NiAl the difference is less than 0.5% (0.289 versus 0.2886 nm [30]) and the calculated result for RuAl is exactly the same as the experimental result [36] (0.303 nm). The lattice constants of NiAl and RuAl calculated by the full potential linearized augmented plane wave (FLAPW) method are about 1.0 - 1.7% smaller than the experimental values. The results from the calculations show both compounds to have large bulk moduli. For NiAl it is slightly larger than experiment (see Table V); for RuAl no experimental result is available at present. NiAl has been found experimentally to have a large formation energy (28.3 kcal/mole) [37], larger than its closest neighbor aluminides such as CoAl (26.4 kcal/mole) [37] and FeAl (12.2 kcal/mole) [37]. The calculations gave results which are within 15% of experiment. The formation energy for RuAl was calculated to be fairly large (35.8 kcal/mole by LMTO and 36.2 kcal/mole by FLAPW). No experimental data are available for direct comparison.

Results for 6 layer (12 atom) supercell calculations show that the APB energy of RuAl is about 70% that of NiAl (690 versus 1000 mJ/m²). From results for larger cells in the case of NiAl, it is estimated that the APB energy for RuAl will converge to about 550 mJ/m². This result is comparable to that for FeAl (490 mJ/m²), for which the $\langle 111 \rangle$ slip direction is observed.

Calculations have also been performed using the FLAPW method to compare the charge distribution in NiAl and RuAl. Charge density plots are given in Figure 4. In NiAl, Ni-Al bonds are extremely strong and directional, with the charge density at the midpoint between the Ni-Al nearest neighbors approximately twice that for Ni-Ni. The charge transfer from Al to Ni is 0.41. In contrast, the charge distribution between Ru-Al nearest neighbors is much less directional. Here, the charge density at the midpoint between the Ru-Al nearest neighbors is approximately half that for Ru-Ru and the charge transfer from Al to Ru is only 0.04.

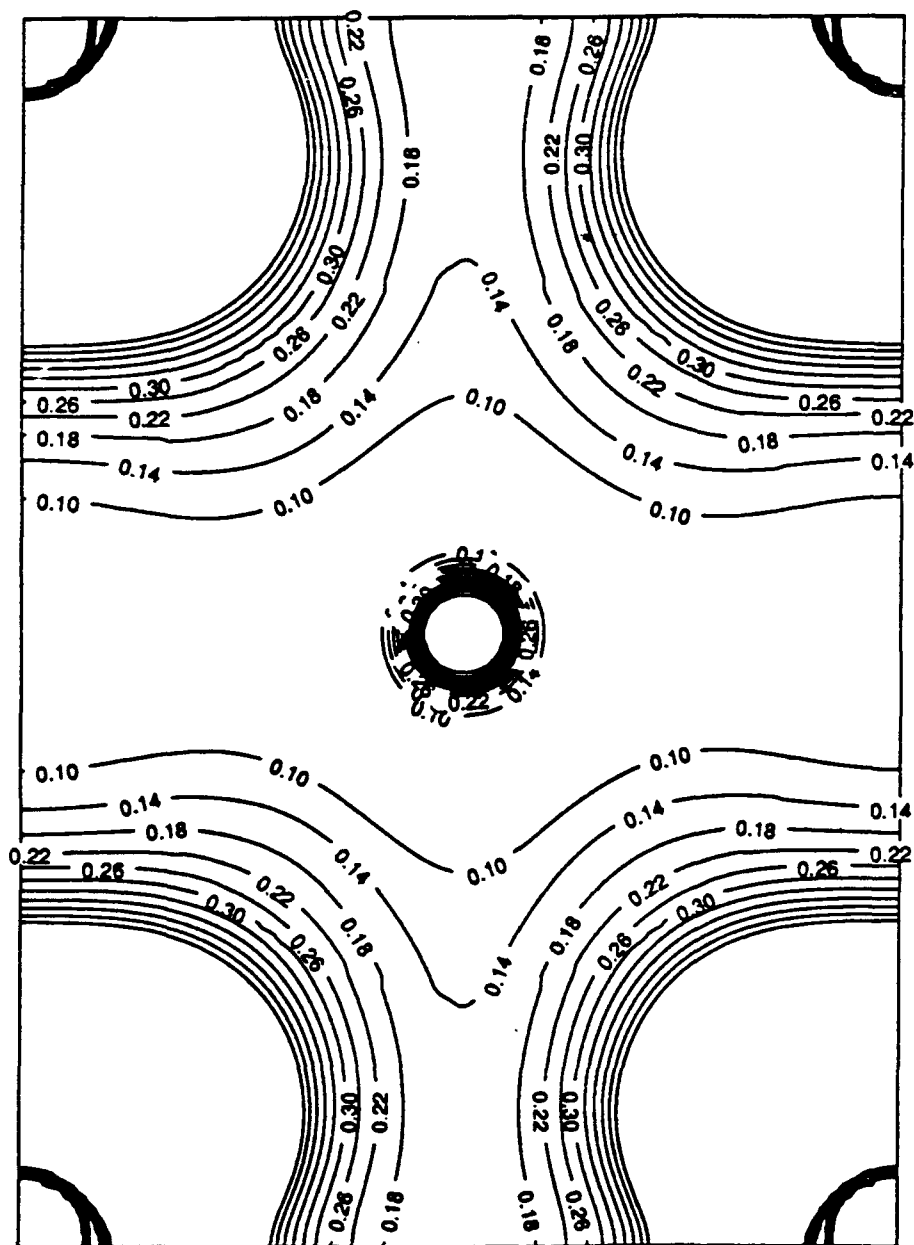
Electronic density of states (DOS) plots for NiAl and RuAl, with and without an APB, are shown in Figure 5. For the unfaulted B2 structure, the Ru d band in RuAl is much broader than is the Ni d band in NiAl, but the DOS characteristics are similar to those of NiAl. The DOS profile and the location of the Fermi energy (E_F) agrees with earlier work [38]. The Ru-d and Al-p hybridization is very strong below E_F , which lies in the bonding region. In the partial DOS, the main peak below E_F is dominated by Ru-d electrons; the Ru-s, p electrons make only a small contribution. On the other hand, between -11.0 eV and -5.0 eV there is a sharp Al-s peak. Between -5.0 eV and 1.5 eV, Al-p and Al-d have comparable contribution. Note that the DOS below the Fermi energy is more severely altered (raised) by the presence of the APB in NiAl than in RuAl. This is consistent with the higher APB energy calculated for NiAl.

Because of the experimental finding that small amounts of elements such as Mo and Ga can significantly improve tensile ductility in NiAl, preliminary calculations of the effects of these elements on the local electronic environment were conducted. Charge density plots in the vicinity of Mo and Ga atoms within an NiAl matrix are shown in Figure 6.



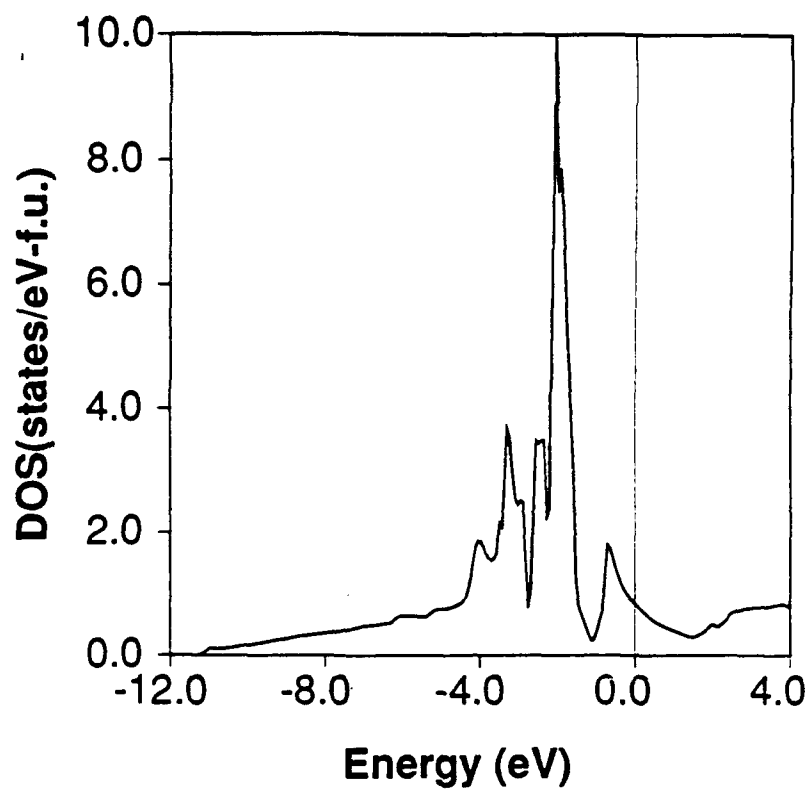
a

Figure 4. Charge density plots for the $\langle 110 \rangle$ plane as determined by Full Potential Linearized Augmented Plane Wave (FLAPW) method. The Al atom is in the center of the plot, and the Ni or Ru atoms at the corners a) NiAl b) RuAl.

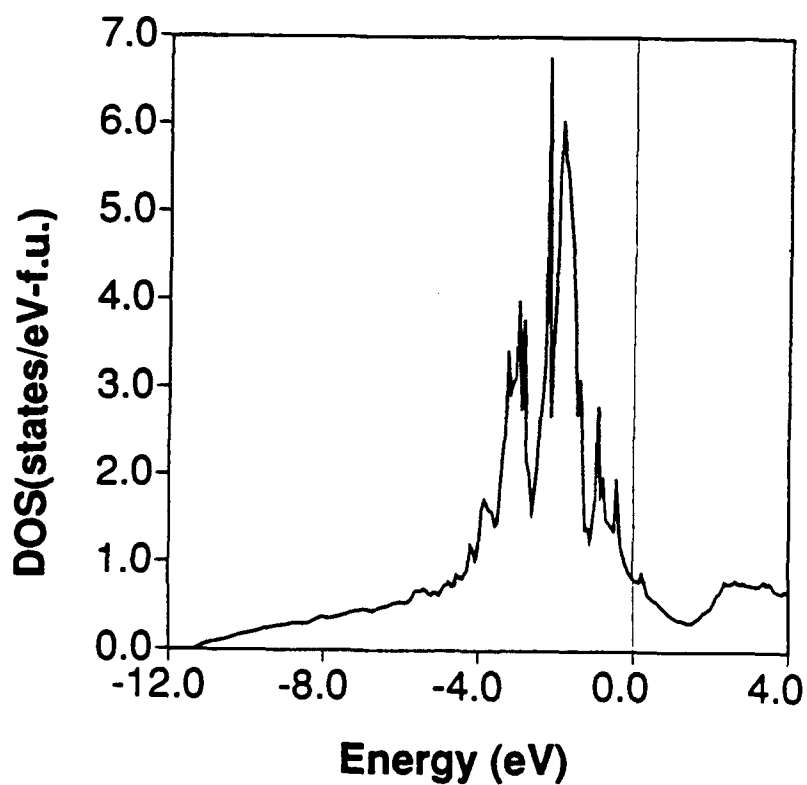


b

Figure 4 (cont.). Charge density plots for the $\langle 110 \rangle$ plane as determined by Full Potential Linearized Augmented Plane Wave (FLAPW) method. The Al atom is in the center of the plot, and the Ni or Ru atoms at the corners a) NiAl b) RuAl.



a



b

Figure 5. Calculated DOS plots for NiAl and RuAl with and without an APB. a) NiAl , b) NiAl with APB, c) RuAl, d) RuAl with APB.

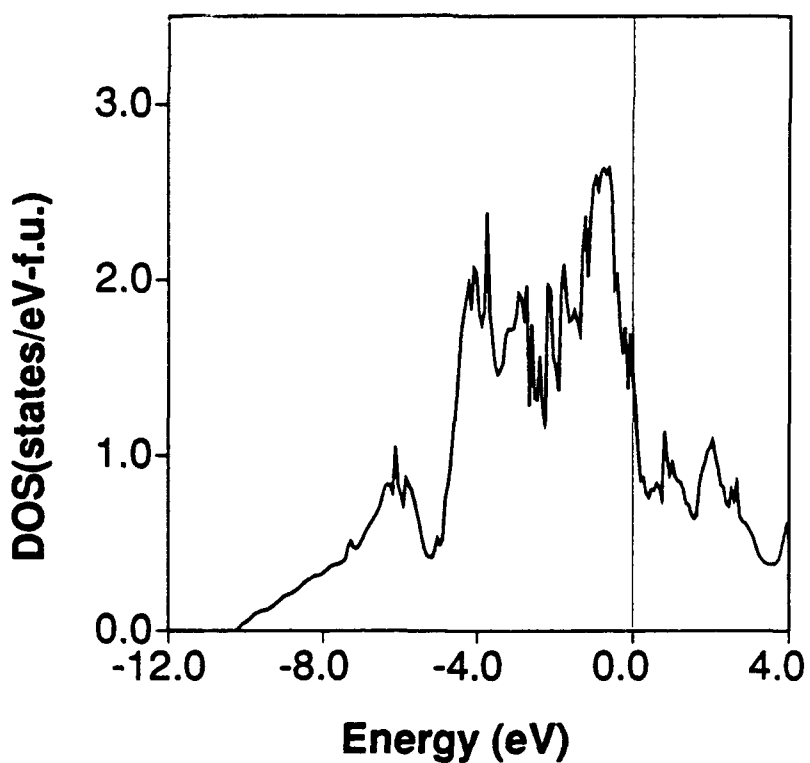
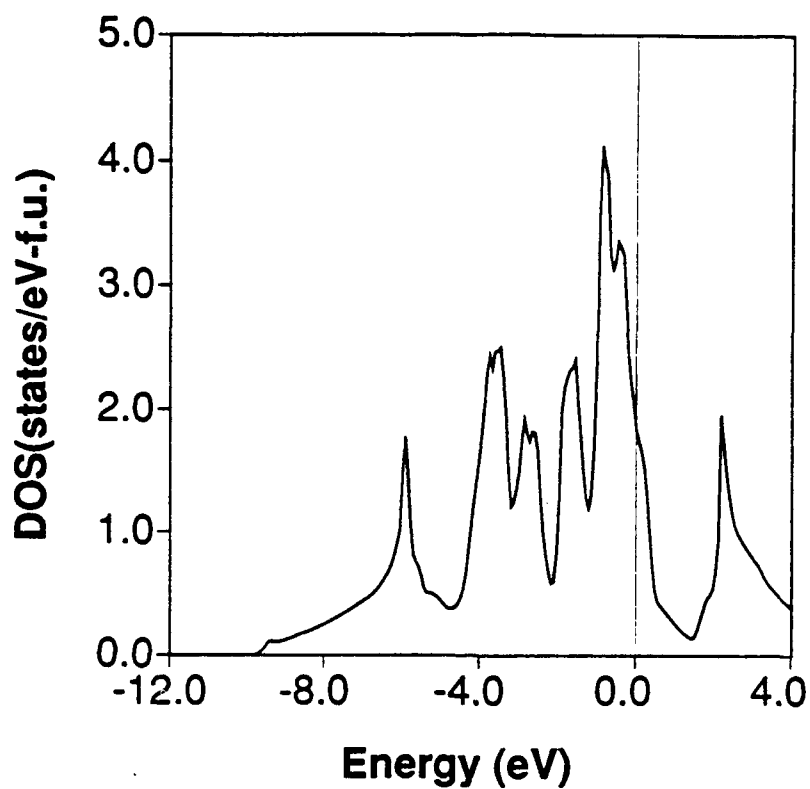
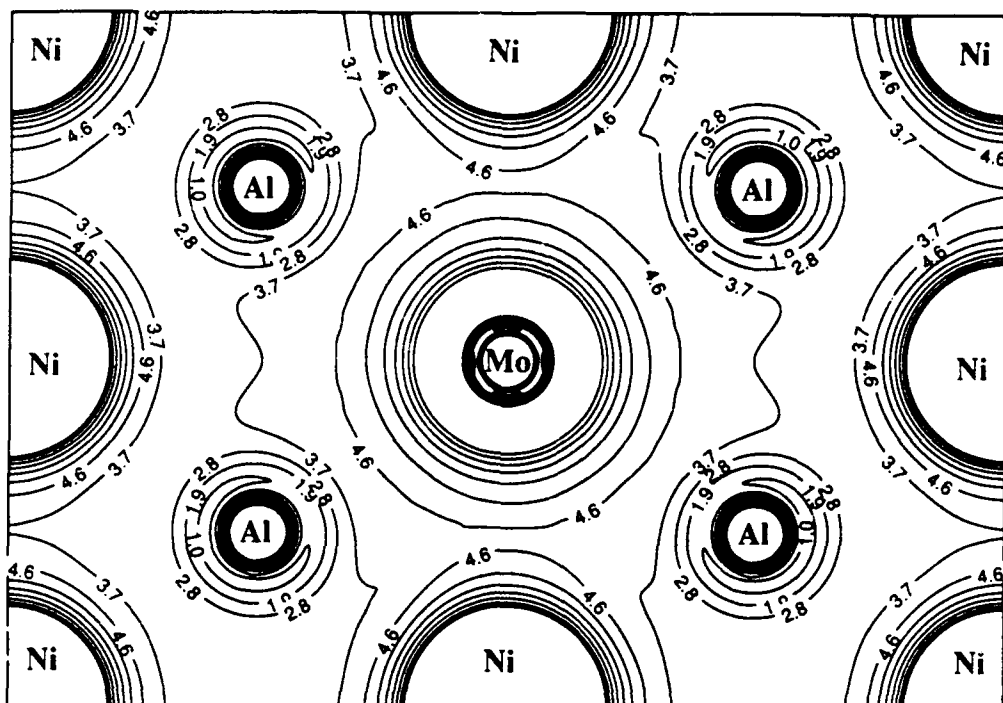
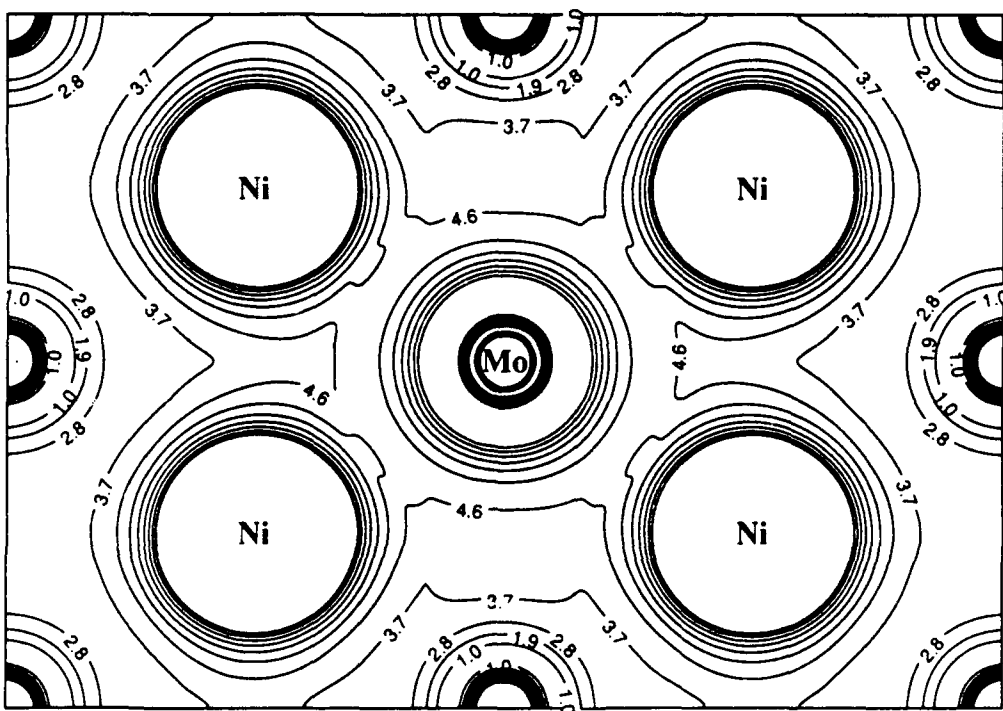


Figure 5 (cont.). Calculated DOS plots for NiAl and RuAl with and without an APB. a) NiAl , b) NiAl with APB, c) RuAl, d) RuAl with APB.

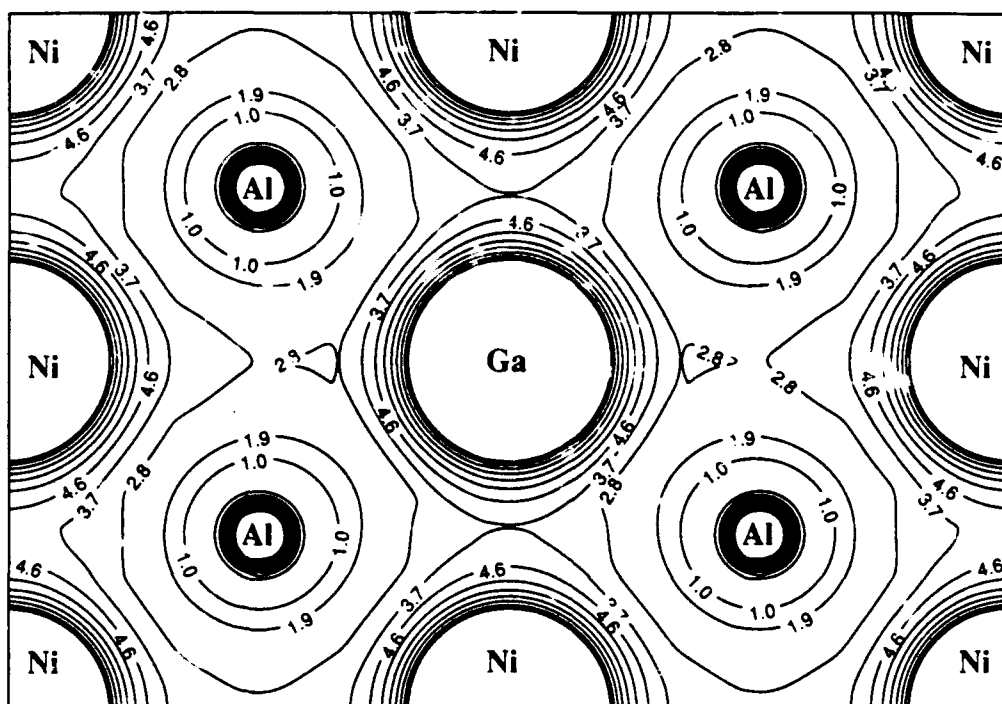


a

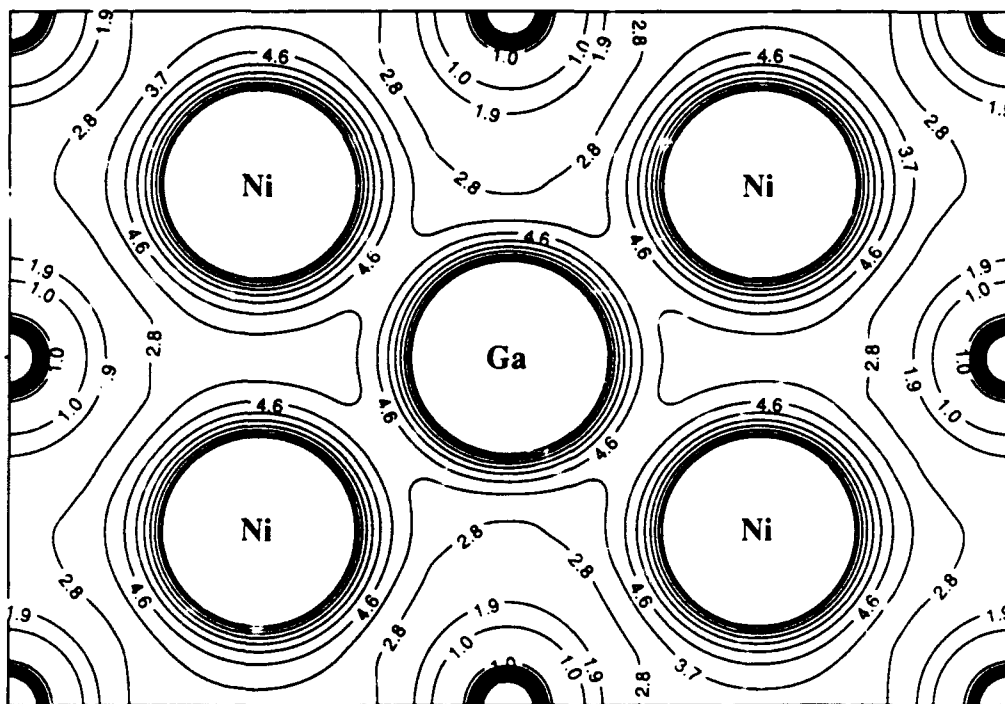


b

Figure 6. Charge density plots for the NiAl $\langle 110 \rangle$ plane as determined by Full Potential Linearized Augmented Plane Wave (FLAPW) method showing the effect of Ga and Mo on local charge distribution. a) Mo substituted for Ni, b) Mo substituted for Al, c) Ga substituted for Ni, d) Ga substituted for Al.



c



d

Figure 6 (cont.). Charge density plots for the NiAl $\langle 110 \rangle$ plane as determined by Full Potential Linearized Augmented Plane Wave (FLAPW) method showing the effect of Ga and Mo on local charge distribution. a) Mo substituted for Ni, b) Mo substituted for Al, c) Ga substituted for Ni, d) Ga substituted for Al.

B Experimental Results

1. Experimental Procedure

Single crystal slabs, 1" x 1-1/4" x 4", of the alloys were grown by a Bridgman method. The slabs were homogenized in an argon atmosphere at 1316°C for 50 hours. They were then oriented using the back reflection Laue technique, and specimens were EDM wire cut from the slabs in the desired crystallographic orientations. Tensile and compression specimens were machined from the blanks using low stress grinding techniques. The tensile specimens were electropolished in a solution of 10% perchloric acid and 90% methanol at -30°C to remove the residual grinding strains. For compression testing, 0.25" diameter specimens were used. Two different lengths were tested: 0.5", giving a length to diameter (L/D) ratio of 2/1, and 0.75", giving an L/D ratio of 3/1.

For elevated temperature tests, the tensile specimens were surrounded with insulating material and induction heated through the specimen grips. Immediately upon completion of the test, the induction current was turned off and the insulation removed. In this manner, cooling rates on the order of 5°C/s were achieved. The compression specimens were heated in a clam-shell type resistance furnace. After testing the power was turned off and the furnace opened. The cooling rate for these specimens is estimated to be somewhat lower than that of the tensile specimens, on the order of 1.5°C/s.

Transmission electron microscopy (TEM) was used to conduct Burgers vector and line direction analyses in order to identify the nature of the dislocations within the deformed specimens and, thereby, determine the operating slip systems. Additionally, the ALCHEMI [39] technique was used to determine the site occupancy of the vanadium and chromium atoms within the crystal lattice. In this technique, x-ray EDS (Energy Dispersive Spectroscopy) spectra are recorded from thin foil specimens at positive and negative deviations from the Bragg condition. The relative intensities of the elemental peaks are then analyzed to determine the site occupancies of elements in solution.

In the martensitic transformation studies, ultrasonic measurements were performed by Dr. J. Trivisanno of John Carroll University in Cleveland OH. Absolute elastic constants were determined by an ultrasonic pulse echo overlap technique employing a magnesium buffer rod. The temperature dependence of the elastic constants was also measured with an overlap technique, but in this case the lithium niobate transducer was mounted directly to the specimen.

2. Results from "Soft" Orientation Studies

A detailed study of RT deformation of NiAl single crystals in three soft orientations ($\langle 110 \rangle$, $\langle 111 \rangle$, and $\langle 112 \rangle$) was conducted. The Schmid factor favors {100} slip in the $\langle 110 \rangle$ orientation and {110} slip in the $\langle 111 \rangle$ and $\langle 112 \rangle$ orientations. Measured yield stress values are shown in

Table VII along with resolved shear stresses on the most highly stressed $\{110\}$ and $\{100\}$ slip planes for each orientation. In addition to data from the current investigation, values reported by Wasilewski et al [13] are also included. This was the only reference which could be found in which yield stress values for several soft orientations were reported. Stress strain curves for specimens tested in the $\langle 111 \rangle$ and $\langle 110 \rangle$ orientation are shown in Figure 7. For the $\langle 110 \rangle$ orientation, there is a gradual yield followed by a shallow work hardening of approximately 35 MPa/% strain. The $\langle 111 \rangle$ specimens exhibit a much sharper yield, followed by a constant stress region for about 0.5% plastic strain, eventually achieving a work hardening rate identical to that of the $\langle 110 \rangle$ specimens. The $\langle 112 \rangle$ specimen also exhibited a similar work hardening rate.

Slip traces on the surfaces of specimens tested to 10% plastic strain were observed optically and in the SEM. The $\langle 111 \rangle$ oriented specimens had well developed slip lines in directions consistent with $\{110\}$ slip planes (Figure 8a). For the $\langle 110 \rangle$ oriented specimens, only coarse, indistinct traces could be seen, so that an unambiguous determination of slip plane could not be made (Figure 8b). However, the directions of the bands were consistent with $\{100\}$ slip planes.

Table VII Resolved Shear Stress Values for $\{110\}$ and $\{100\}$
Slip Planes from "Soft" Orientation NiAl Crystals

<u>Orientation</u>	<u>Resolved Shear Stress (MPa)</u>			<u>Source</u>
	<u>0.2% YS (MPa)</u>	<u>$\{110\}$</u>	<u>$\{100\}$</u>	
111	264±4.6	124±2.2	87±1.5	Current Study
110	217±0.7	76±0.2	109±0.4	Current Study
112	250	118	83	Current Study
111	145*	68	48	Wasilewski et al [13]
110	290*	100	145	Wasilewski et al [13]
112	200*	94	66	Wasilewski et al [13]

Data represent average and spread for two compression tests for the $\langle 111 \rangle$ and $\langle 110 \rangle$ orientation. The $\langle 112 \rangle$ YS is from a single compression specimen.

* Estimated from stress-strain curves in Figure 1 of Wasilewski et al [13].

TEM micrographs of dislocation structures from $\langle 111 \rangle$ and $\langle 110 \rangle$ oriented specimens are shown in Figure 9. The specimens were tested to ~4% plastic strain at room temperature. The Burgers vectors (**b**) of the dislocations were found to be of the $\langle 100 \rangle$ type, with a single **b** dominating in the area of analysis. Line direction analysis of bent dislocations reveals that most do not lie on slip planes. A few dislocations were found to lie on $\{110\}$ planes for the $\langle 111 \rangle$ oriented specimens and on $\{100\}$ planes for the those oriented along $\langle 110 \rangle$. A common feature for both orientations was the presence of elongated prismatic loops, lying on $\{110\}$ planes ~45° from their Burgers vectors. For the $\langle 111 \rangle$ specimens, these tend to be elongated close to $\langle 110 \rangle$ directions, while those in the $\langle 110 \rangle$ specimens tend to lie close to $\langle 100 \rangle$ directions. In each case

NiAl Compression Stress-Strain Curves

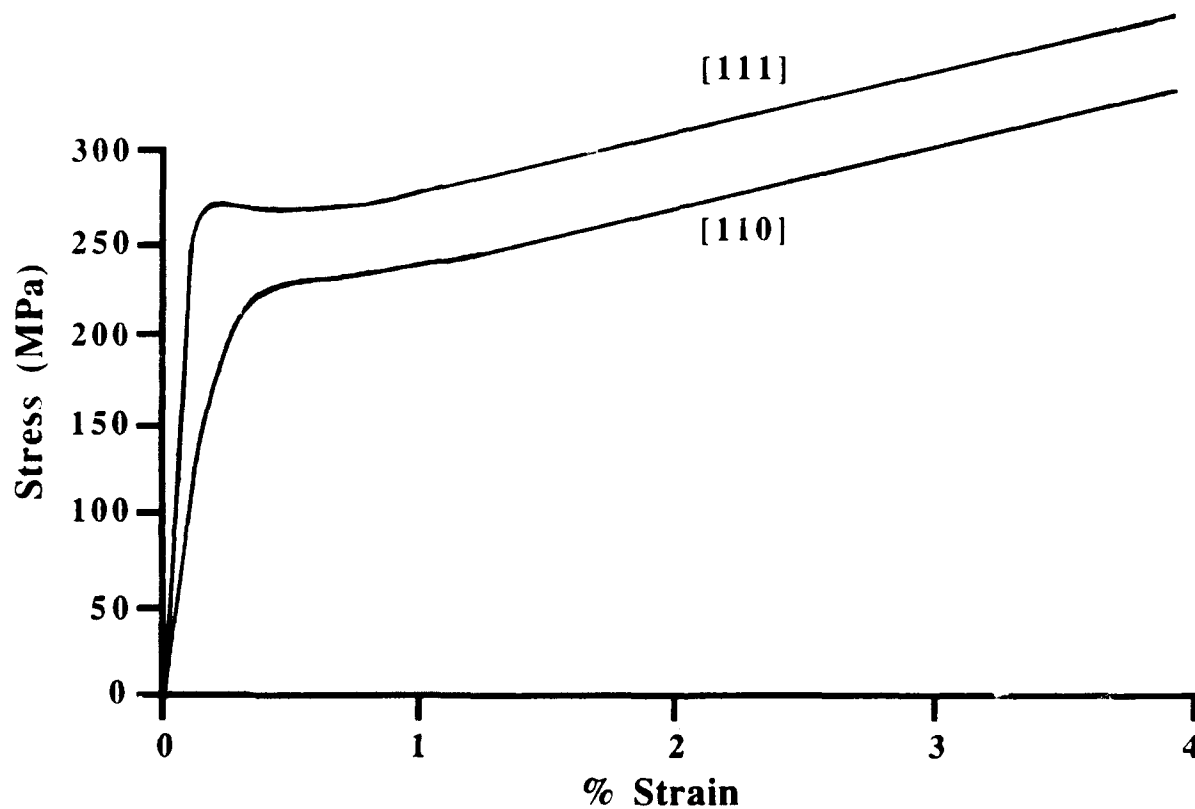
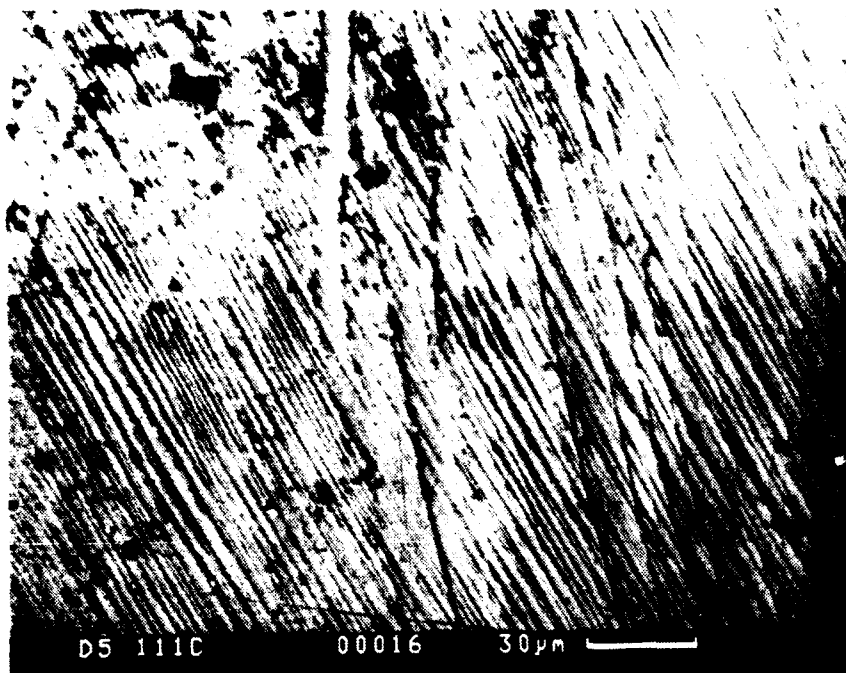
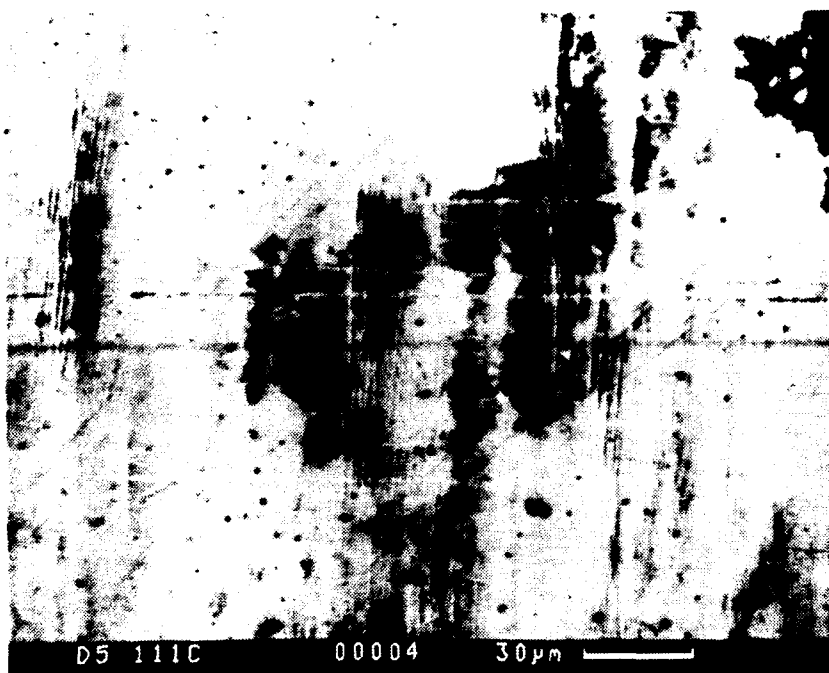


Figure 7. Stress-strain curves for two "soft" oriented NiAl crystals tested in RT compression.



a

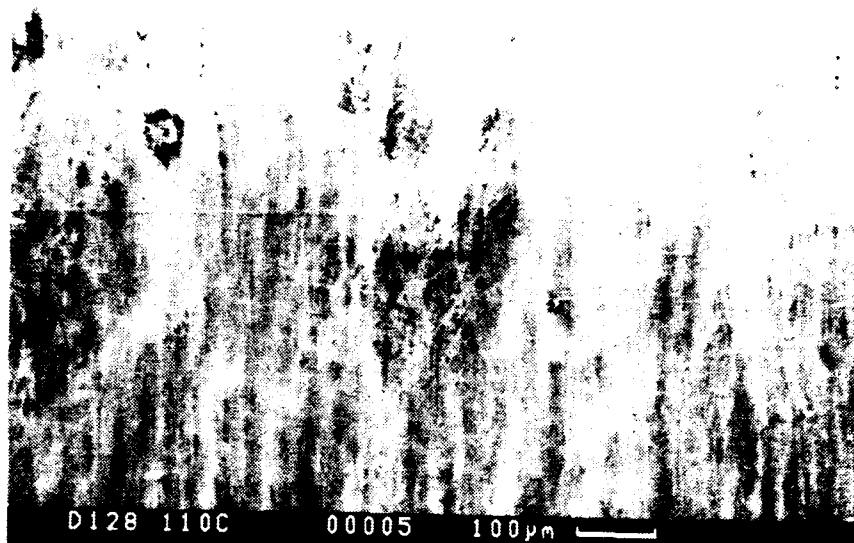
SEM $[01\bar{1}]$



b

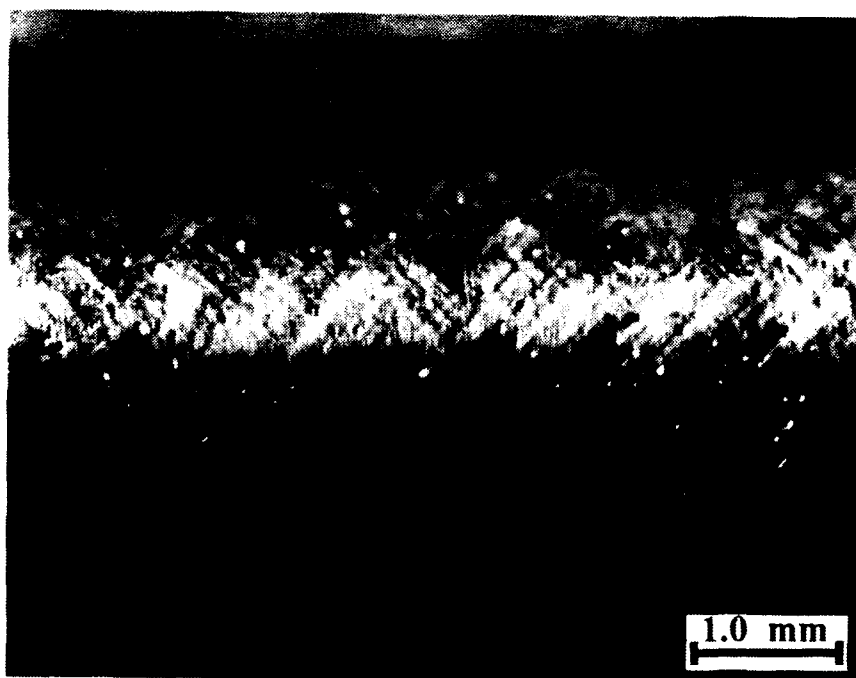
SEM $[\bar{1}2\bar{1}]$

Figure 8. Surfaces of RT compression specimens. a) and b) SEM micrographs of $[111]$ specimen showing distinct slip traces. c) SEM micrograph of $[110]$ specimens showing absence of visible slip traces. d) Optical micrograph of $[110]$ specimen showing broad indistinct bands.



c

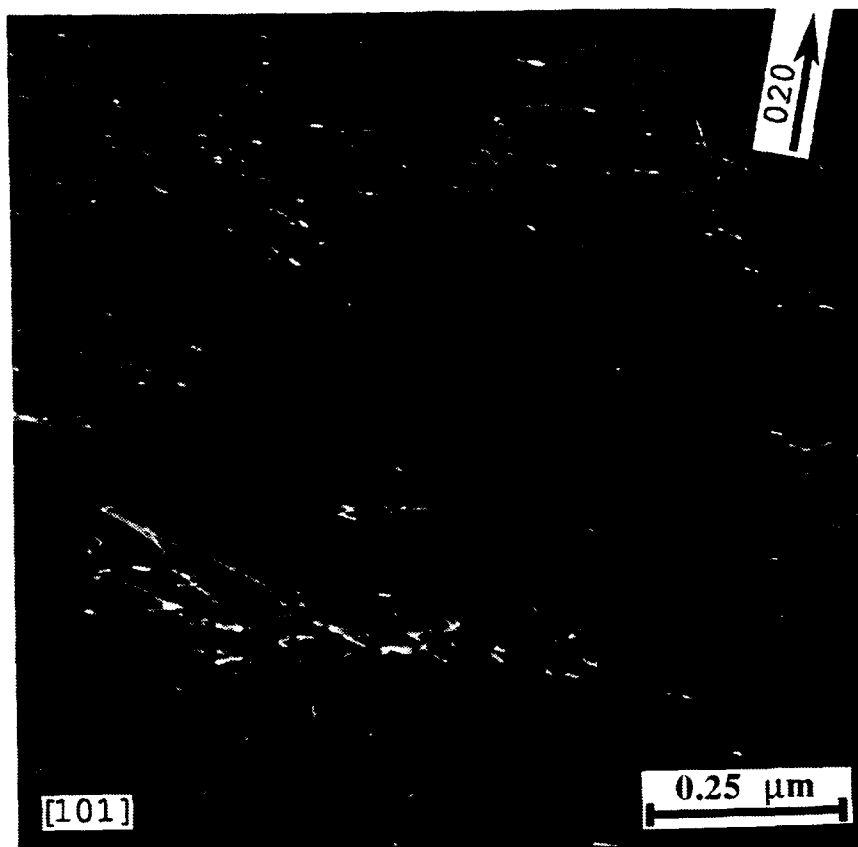
SEM $[1\bar{1}0]$



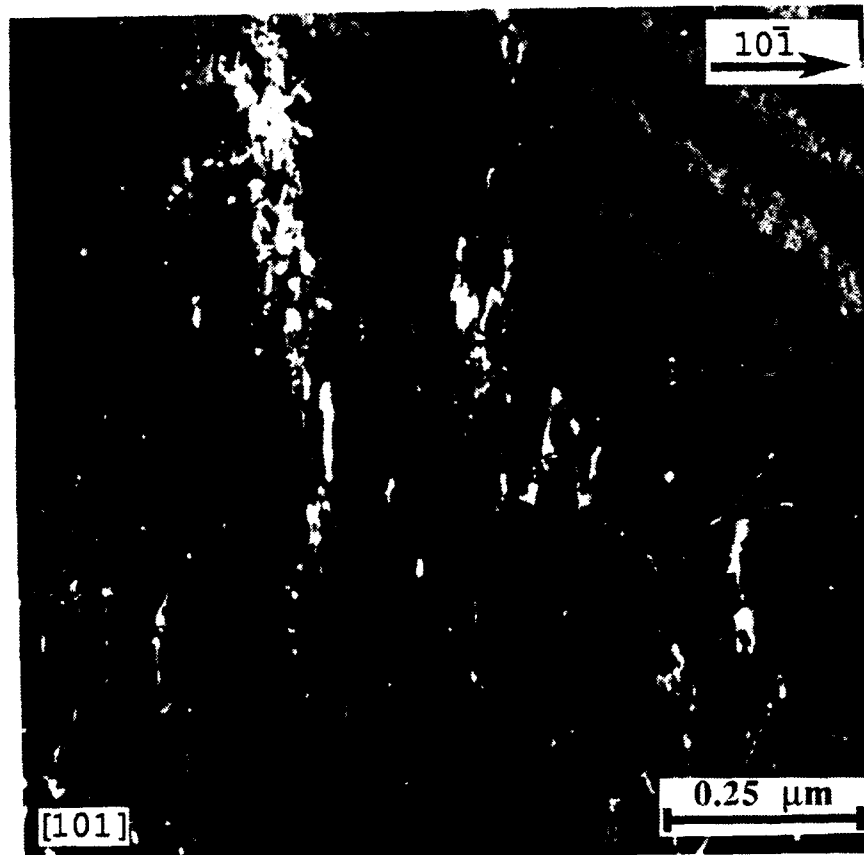
d

Optical Micrograph

Figure 8 (cont). Surfaces of RT compression specimens. a) and b) SEM micrographs of $[111]$ specimen showing distinct slip traces. c) SEM micrograph of $[110]$ specimens showing absence of visible slip traces. d) Optical micrograph of $[110]$ specimen showing broad indistinct bands.



a



b

Figure 9. Weak beam TEM micrographs of loops in RT compression specimens. a) $[111]$ compression axis: $\mathbf{b}=[010]$ loop elongated along direction near $[10\bar{1}]$. b) $[101]$ compression axis: $\mathbf{b}=[001]$ loop elongated along direction near $[010]$.

the elongation direction was approximately 90° from the Burgers vector.

Table VIII Resolved Shear Stress Values for {100} Slip Planes as a Function of Temperature

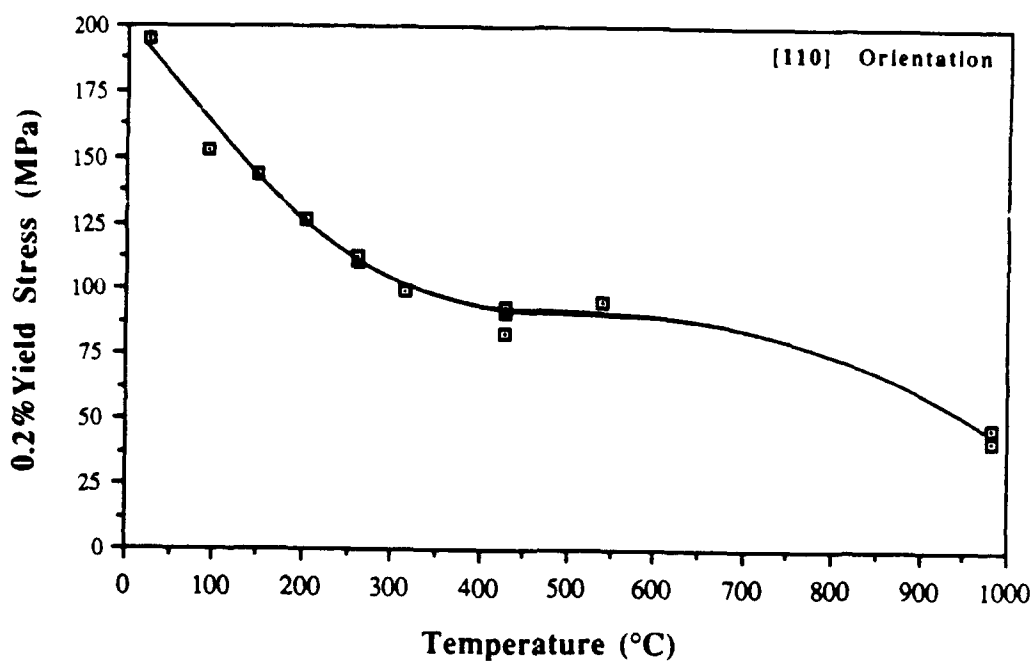
<u>Orientation</u>	<u>Temp. (°C)</u>	<u>0.2% YS (MPa)</u>	<u>Resolved Shear Stress On the {100} Plane (MPa)</u>
110	RT	171±3	86
110	150	129±1.5	65
110	200	119±6	60

Tensile yield stress and plastic elongation to failure data have been measured in <110> oriented specimens. These data are shown in Figure 10. In order to determine the effect of temperature on the relative CRSS values for the {100} and {110} planes, a study was initiated in which compression testing is being conducted at -196°C, RT, and near the DBTT (150 and 200°C) in both <110> and <111> orientations. All specimens were taken from one single crystal casting. Some preliminary results for the <110> orientation are listed in Table VIII. This study will be continued under the follow-on AFOSR contract.

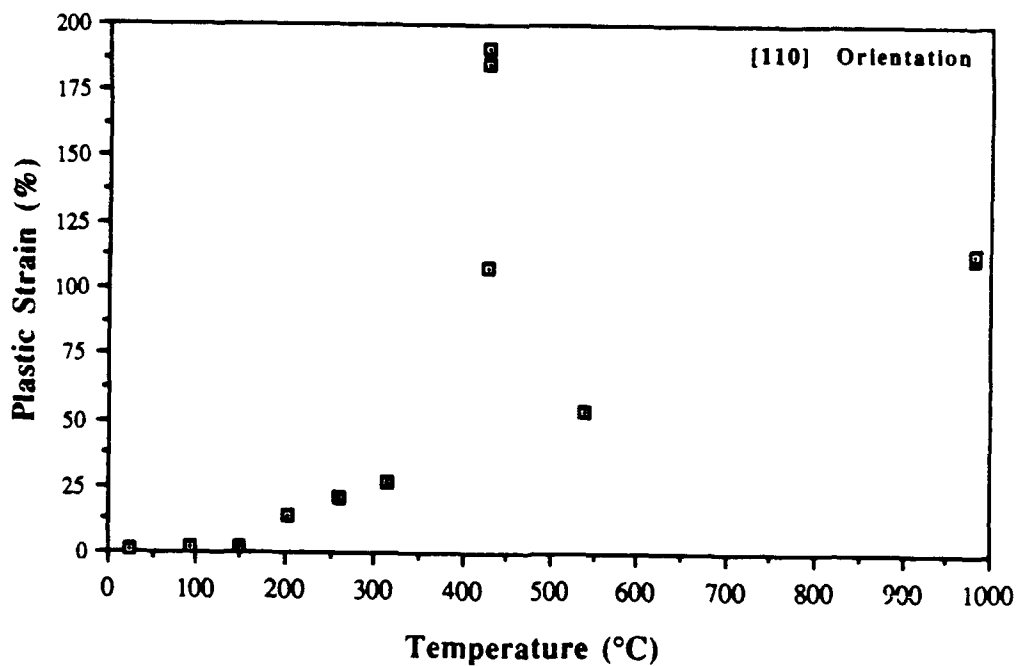
3. Results from Microalloying Effect Studies

Although an in depth investigation of the microalloying effect will be the subject of a follow-on study, some preliminary work on this phenomenon was performed under the current program. Specifically, two compositions were investigated in RT compression and tensile tests: a 0.05%Ga alloy and one containing 0.1%Mo (both in at%). Both of these alloys had been found to display increased tensile ductility over stoichiometric NiAl in <110> orientated specimens. The Ga containing alloy exhibited a slight decrease in yield strength compared to the binary compound, while the Mo addition resulted in increased yield strength.

Specimens of these two alloys were tested in compression in both <110> and <111> orientations, in order to determine if the relative values of CRSS for the {100} versus {110} slip planes are different from those of the binary compound. Results from these tests are given in Table IX in the form of CRSS values for the two slip planes and work hardening rates for the different orientations (the values for the binary compound are from the same specimens for which CRSS values are reported in Table VII). Although some differences in work hardening rates and the CRSS ratios are apparent between the stoichiometric and microalloyed materials, these are well within the normal scatter for these alloys. Thus, apart from changes in yield strength and increased ductility, no significant differences are observed in the RT stress-strain behavior of the microalloyed materials versus the binary compound.



a



b

Figure 10. a) 0.2% yield strength (compression and tension) and b) tensile elongation data as a function of temperature for [110] oriented tensile and compression specimens.

Table IX CRSS and Work Hardening Rates (WHR) for NiAl Alloys

<u>Alloy</u>	<u><100>/{110}*</u>		<u><100>/{100}**</u>		<u>CRSS Ratio</u> <u>{110}/{100}</u>
	<u>CRSS</u>	<u>WHR</u> [†]	<u>CRSS</u>	<u>WHR</u> [†]	
NiAl	124	36	109	34	1.22
+0.05%Ga	90	49	82	33	1.16
+0.1%Mo	154	52	145	42	1.13

*Measured in <111> compression

**Measured in <110> compression

[†]MPa/%strain @ 2% plastic strain

Low temperature heat treatments (800°C/50hrs.) have also been found to increase RT ductility in NiAl. This was first observed in polycrystalline specimens [40], and work at GEAE has confirmed a ductility enhancement in "soft" oriented single crystal specimens (see Figure 11). The increased ductility is accompanied by a decrease in yield strength.

Resistivity measurements were taken at RT and 80 K on specimens from the same single crystal slab which received both the standard homogenization heat treatment (1316°C/50hrs.) and a subsequent low temperature heat treatment (800°C/50hrs.). These measurements were also taken on the 0.05% Ga alloy discussed above (given the standard heat treatment). The temperature independent contribution to the resistivity (usually associated with point defect concentrations) was reduced in both specimens, compared to that of the binary compound given the standard heat treatment alone, so that the ratio of the RT to low temperature resistance was increased, as shown in Table X. This indicates that the point defect concentration has been reduced. One possibility is that the concentration of excess vacancies produced during the homogenization heat treatment is reduced, either by annealing out during the low temperature heat treatment or by interactions with the microalloying element. However, the slabs used for this study are furnace cooled from the homogenization treatment, resulting in a relatively slow cooling rate. Also, density measurements of the as-homogenized and heat treated material revealed no significant change in density (associated with differences in vacancy concentration) resulting from the low temperature anneal. Another possibility is that interstitials are removed from the matrix by gettering and/or clustering around the microalloying element or by reacting with other impurities during the low temperature anneal, thus reducing their strengthening effect. Clearly more work is required to understand this phenomenon, and it is likely that the microalloying and heat treatment effects are related. This will be studied under the follow-on AFOSR contract.

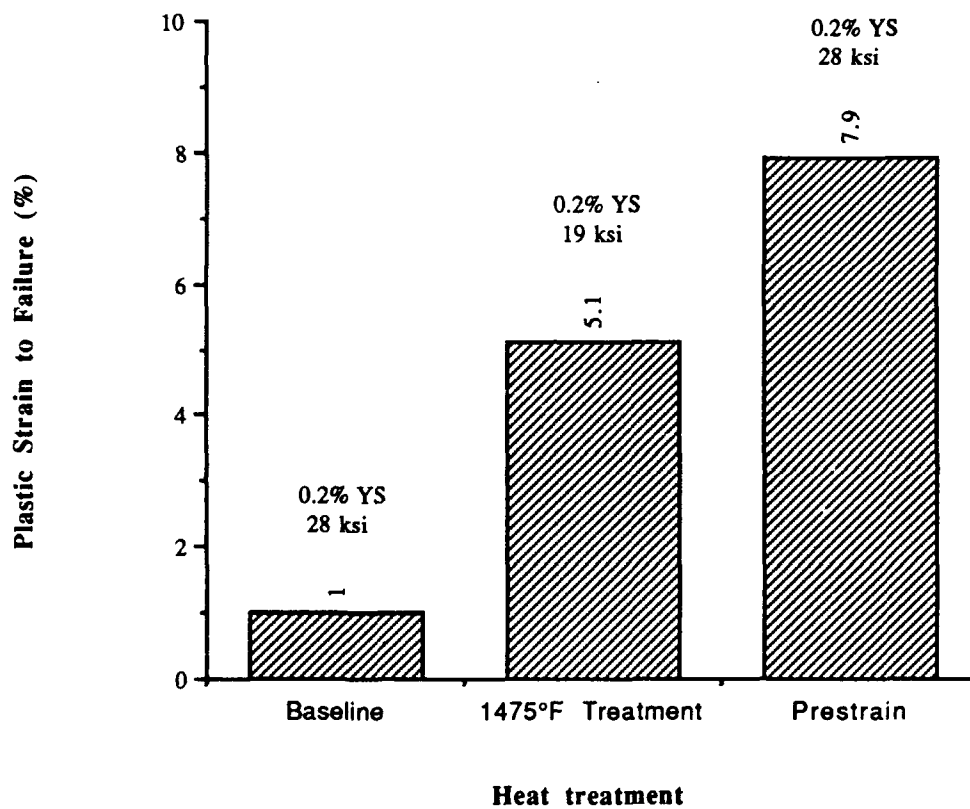


Figure 11. Bar chart showing the effect of low temperature heat treatment on $\langle 110 \rangle$ tensile ductility in a stoichiometric NiAl alloy.

Table X Results from Resistivity Measurements

<u>Alloy</u>	<u>Heat treatment[†]</u>	<u>Resistivity Ratio(RT/80K)</u>
NiAl	std. HT	2.53
NiAl	std. HT + 800°C/50hrs.	3.20
+0.05%Ga	std. HT	2.74

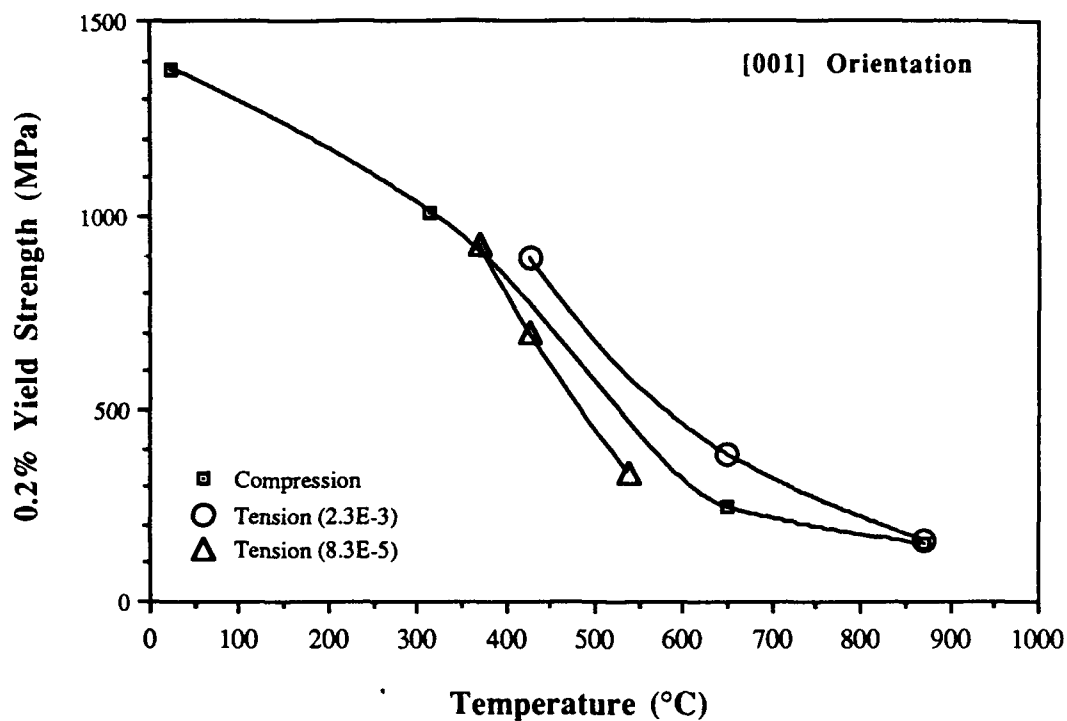
[†]std. HT: 1316°C/50hr.

4. Results from "Hard" Orientation Studies

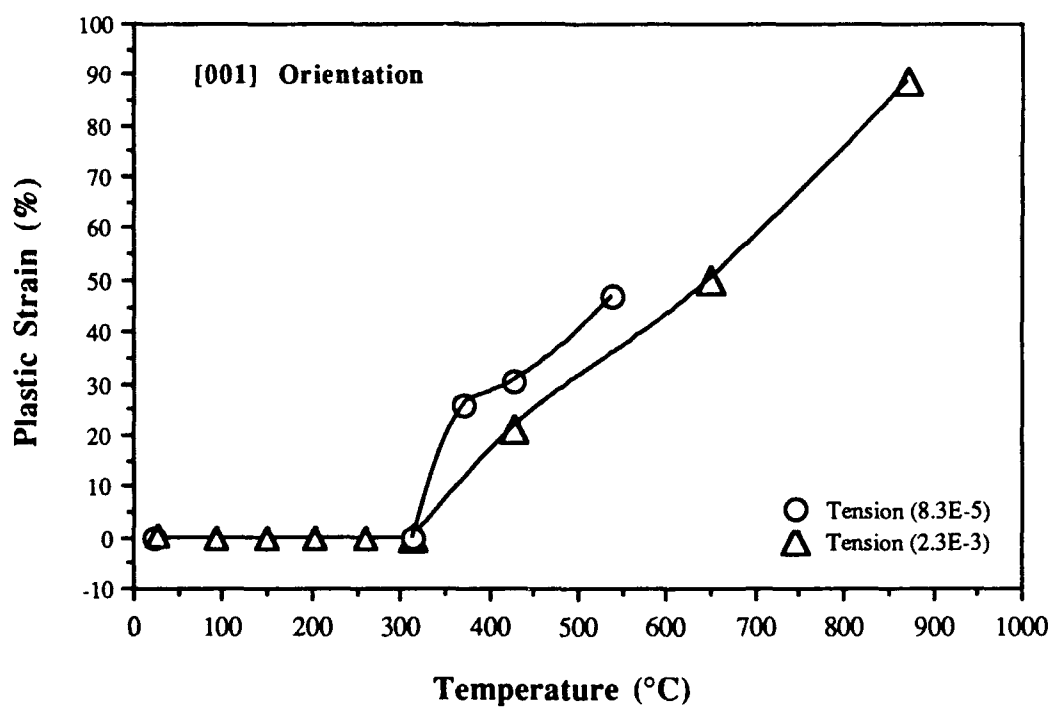
Stoichiometric NiAl was tested in tension and compression from RT to 871°C in the [001] ("hard") orientation. The compression specimens kinked at all temperatures, although substantial uniform deformation was also observed at the higher temperatures. The compressive 0.2% yield strength (YS) as a function of temperature is shown in Figure 12. The majority of the tests were conducted on 3/1 L/D specimens. RT compression tests on 2/1 L/D specimens were also performed in [001] and [110] orientations and strength values were consistent with those obtained from the longer specimens.

The [001] oriented tensile specimens failed without yielding at temperatures up to and including 316°C. From 371 to 649°C, the specimens underwent yielding and a corresponding yield drop (ie. upper and lower yield point). No yield drop was observed at 871°C. Plastic strain to failure and 0.2% yield stress data as a function of temperature for stoichiometric NiAl [001] tensile specimens are also shown in Figure 12. Data for two different strain rates are shown. The higher strain rate resulted in slightly higher yield stress values. The 0.2% YS measured in tension decreased with increasing temperature and the ductile to brittle transition temperature (DBTT) for the stoichiometric NiAl was determined to be between 316 and 371°C.

TEM foils obtained outside the kinked regions of [001] oriented 3/1 L/D compression specimens tested between RT and 427°C revealed dislocation distributions similar to those of the untested material. At 649°C and 871°C, high densities of dislocations were observed. The vast majority of the dislocations in the unkinked regions were found to possess <100> Burgers vectors. These are largely in the form of loops, drawn out along <100> directions perpendicular to their Burgers vectors. In Figure 13, for example, $\mathbf{b}=[100]$ and $\mathbf{b}=[010]$ loops are elongated along [010] and [100] directions, respectively. Some $\mathbf{b}=\langle 110 \rangle$ (with Burgers vectors both perpendicular and 45° to the stress axis) and even occasional $\mathbf{b}=\langle 111 \rangle$ dislocation segments were found, usually as parts of loose tangles involving nodal reactions with $\mathbf{b}=\langle 100 \rangle$ dislocations. However, a few $\mathbf{b}=\langle 110 \rangle$ dislocations were observed which possess Burgers vectors expected to contribute to deformation of the [001] oriented specimen (eg. [101]) and were bowed out on slip



a



b.

Figure 12. a) 0.2% yield strength data as a function of temperature for [001] oriented compression and tensile specimens. The strain rate for compression testing was 3.3×10^{-5} /s. Data for two different strains rates are shown for the tensile specimens: 8.3×10^{-5} /s and 2.3×10^{-3} /s. b) Plastic elongation values for the tensile test specimens in (a).

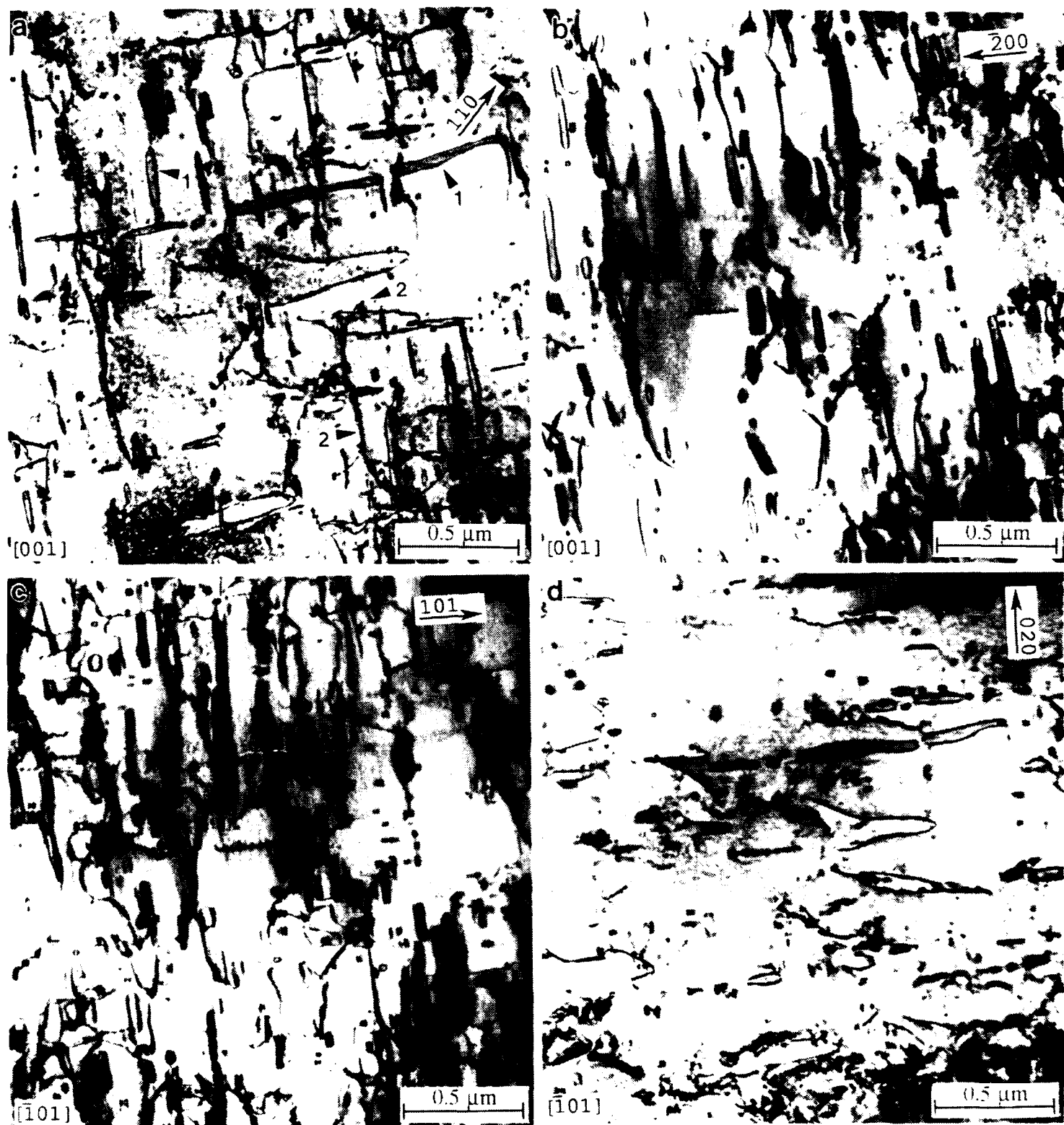


Figure 13. TEM micrographs of an [001] oriented compression specimen tested to 1.8% plastic strain at 649°C, showing elongated $b=\langle 100 \rangle$ loops (1) and $b=[101]$ dislocations bowed out on a $(10\bar{1})$ plane (2).

planes. The dislocation densities in the 871°C specimen were considerably lower than in the 649°C specimen, indicating that recovery has taken place. This may have occurred during cool down of the specimen after the test or resulted from dynamic recovery occurring during testing.

Since other investigations in which $\langle 111 \rangle$ slip was observed at RT were performed on compression specimens with L/D ratios less than 3/1 [13,16,41], a limited number of specimens with 2/1 L/D were tested at RT. Although some kinking did occur during testing, sufficient uniform yielding was obtained to extract 0.2% YS values. TEM of foils taken from the unkinked regions revealed well defined bands of $\mathbf{b}=\langle 111 \rangle$ dislocations, as shown in Figure 14.

The dislocation structures in specimens tested in tension were similar to those of the compression specimens at the same temperature. Below the ductile to brittle transition temperature (DBTT), the dislocation distribution was similar to the untested material, consistent with the lack of plasticity observed during testing. Foils from the 427 and 649°C specimens were found to contain high dislocation densities. As in the case of the compression specimens, $\mathbf{b}=\langle 100 \rangle$ dislocations dominate the microstructure, a large fraction in the form of prismatic loops lying on or near $\{110\}$ planes 45° from their Burgers vectors and elongated along $\langle 100 \rangle$ directions. Again, occasional $\mathbf{b}=\langle 110 \rangle$ dislocations were observed to be bowed out on $\{110\}$ slip planes. An example is given in Figure 15, from a 649°C specimen, for which testing was interrupted after 1.5% plastic strain. At 871°C, dynamic recovery during testing is evident (Figure 16). Sub-boundaries surrounding regions of relatively low dislocation density dominate the microstructure. These boundaries, consisting of nets of $\mathbf{b}=\langle 100 \rangle$ dislocations, are reminiscent of those observed in creep specimens [42]. It is possible that this recovery took place after testing (ie. during cool down). This is considered unlikely, however, due to the rapid cooling associated with the induction heating technique and immediate removal of insulation at the completion of each test.

It was found that considerable tensile elongation could be obtained in $[001]$ oriented specimens even at relatively fast strain rates at elevated temperatures. As seen in Figure 12, an elongation to failure of ~20% was obtained at 427°C at a strain rate of $2.3 \times 10^{-3}/s$. Figure 17 shows the dislocation structure in a tensile specimen tested at 427°C, at a strain rate of $8.3 \times 10^{-5}/s$, but interrupted after only 0.5% plastic strain. Distinct slip bands are observed. The centers of these bands contain $\mathbf{b}=\langle 100 \rangle$ and $\mathbf{b}=\langle 110 \rangle$ dislocations. On the outer edges, where fewer dislocation interactions are expected, primarily $\mathbf{b}=\langle 110 \rangle$ dislocations are observed, all exhibiting the same Burgers vector within a given slip band. The Burgers vectors of these dislocations and the $\{110\}$ slip planes on which they lie are each 45° from the $[001]$ tensile axis, resulting in a Schmid factor of 0.5. Most appear to be gliding roughly perpendicular to their Burgers vectors (ie. in the screw orientation), and many have trailing $\mathbf{b}=\langle 100 \rangle$ loops. For example, the dislocations in Figure 17 have $[10\bar{1}]$ Burgers vectors and are bowed out on (101) planes. Some of these have trailing $\mathbf{b}=[100]$ loops (designated by arrows in (b) and (d)), elongated along $[010]$ and lying near the $(10\bar{1})$ plane. The loop labeled "1" in 17(b) connects two different $\mathbf{b}=[10\bar{1}]$ dislocations. No dissociation of the $\mathbf{b}=\langle 110 \rangle$ dislocations, either into $\langle 100 \rangle$ or $1/2\langle 111 \rangle$ components, was observed along the bulk of the dislocation line in weak beam micrographs.

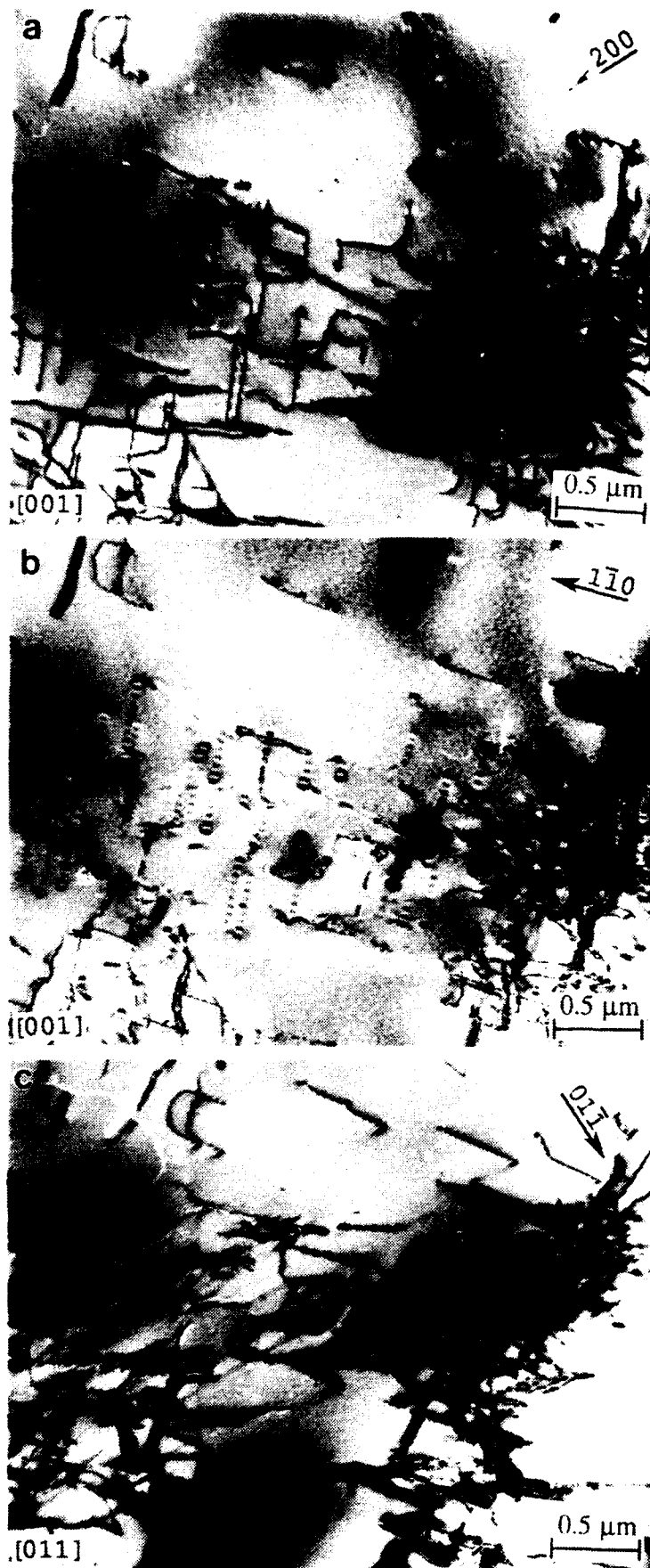


Figure 14. TEM micrographs showing $\mathbf{b}=\langle 111 \rangle$ dislocations in a $[001]$ oriented compression specimen, with a 2/1 L/D ratio, tested to 1.6% plastic strain at room temperature. Dislocations with $\mathbf{b}=[11']$, lying on $(11\bar{2})$ slip planes, are out of contrast for the $(1\bar{1}0)$ and $(01\bar{1})$ g-vectors.

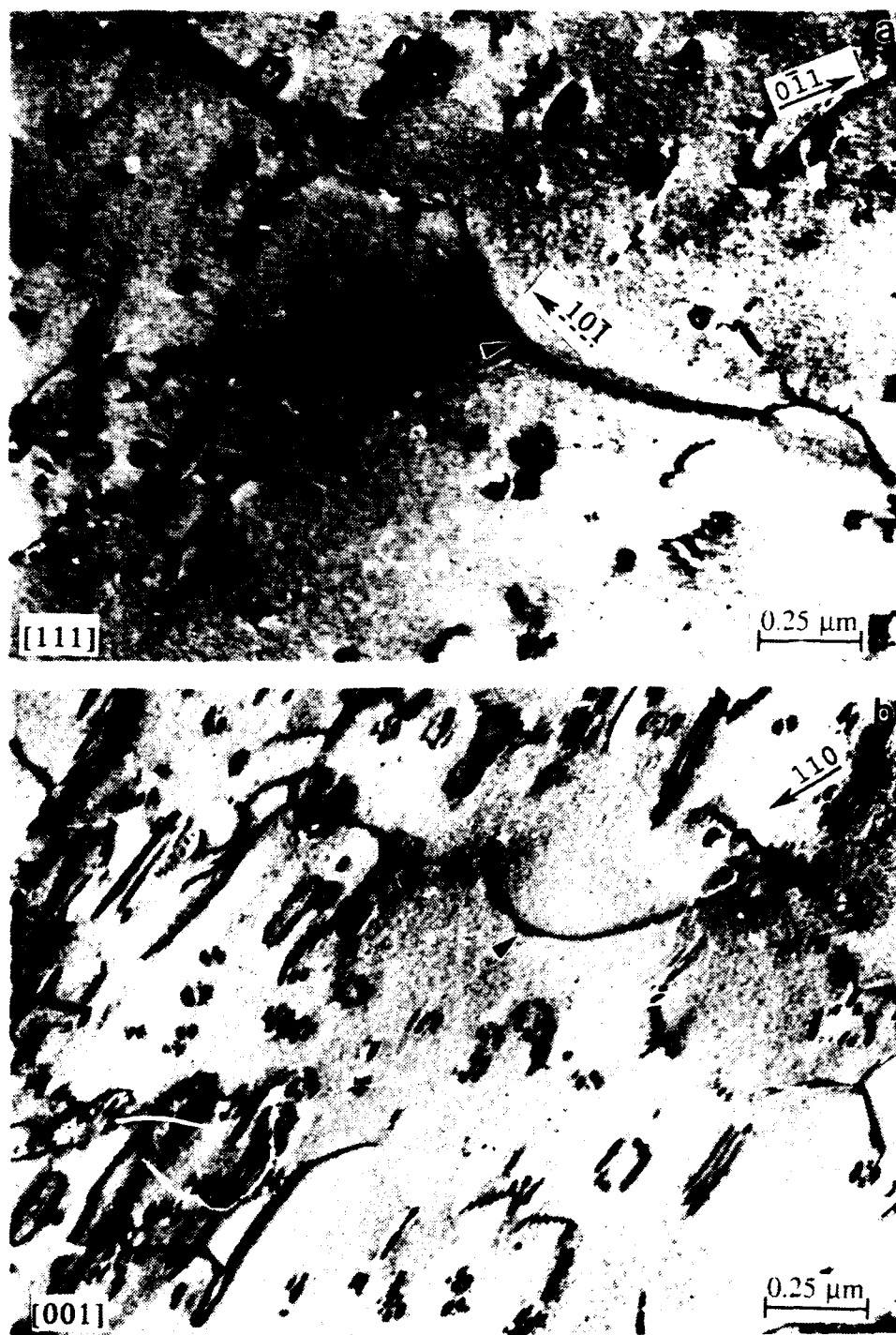


Figure 15. TEM micrographs of an [001] oriented tensile specimen tested to 1.5% plastic strain at 649°C (strain rate = 2.3×10^{-3} /s) showing a $\mathbf{b}=[10\bar{1}]$ dislocation bowed out on a (101) plane (arrow). The $[10\bar{1}]$ direction is shown in (a). The $\mathbf{b}=[10\bar{1}]$ dislocation is out of contrast in (c) and (d).

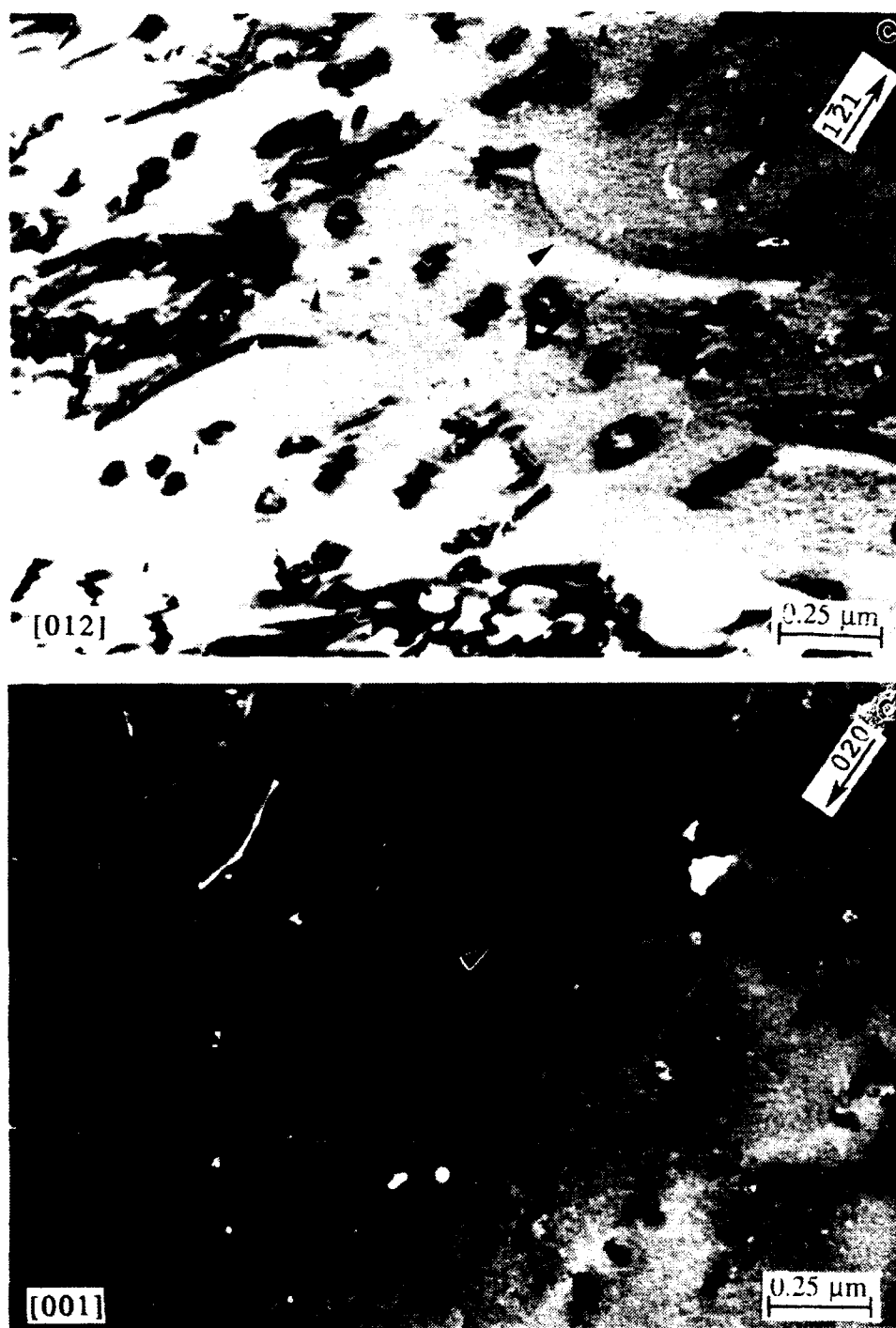


Figure 15 (cont.). TEM micrographs of an [001] oriented tensile specimen tested to 1.5 % plastic strain at 649°C (strain rate = 2.3×10^{-3} /s) showing a $\mathbf{b}=[10\bar{1}]$ dislocation bowed out on a (101) plane (arrow). The $[10\bar{1}]$ direction is shown in (a). The $\mathbf{b}=[10\bar{1}]$ dislocation is out of contrast in (c) and (d).

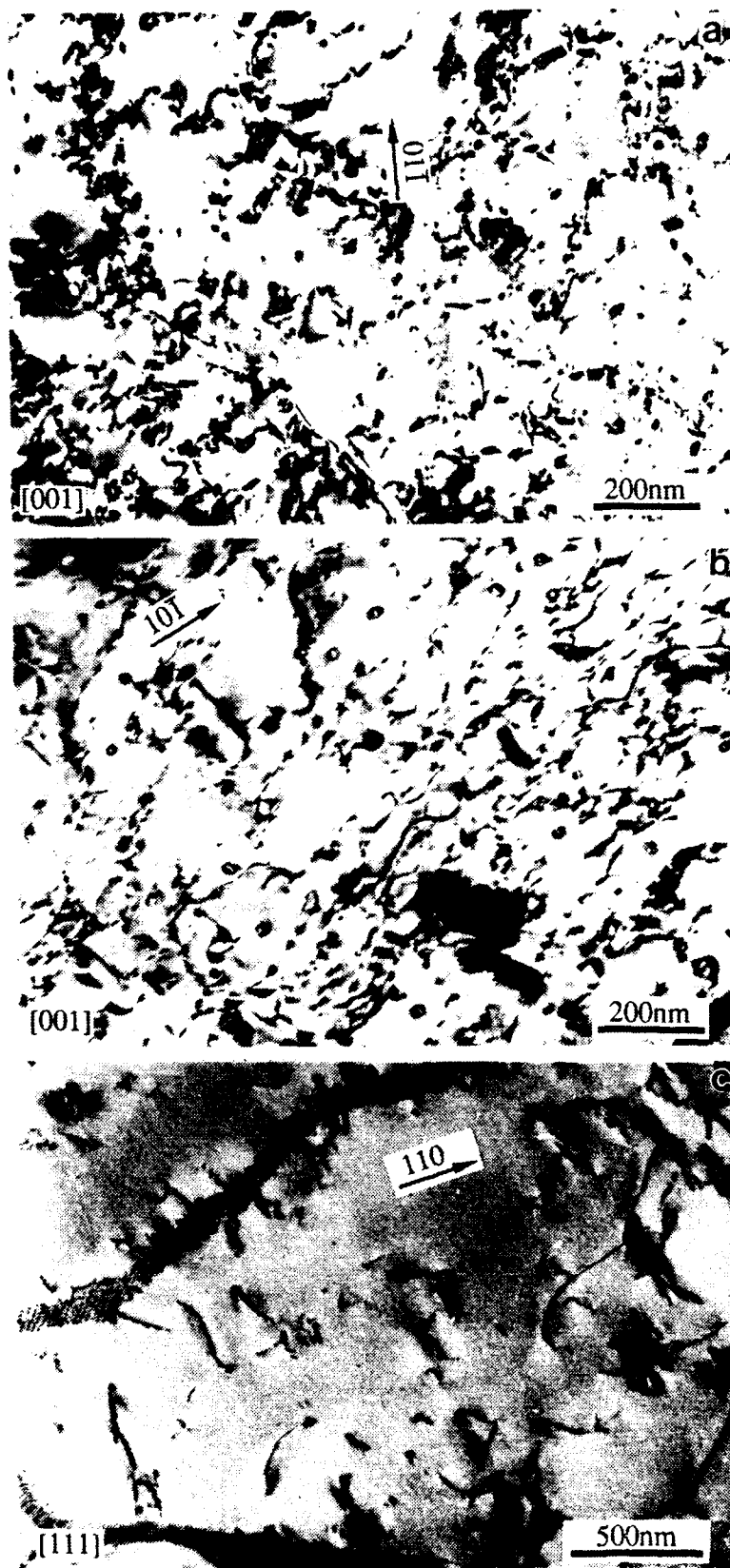


Figure 16. TEM micrographs showing the general dislocation structure in stoichiometric NiAl $\langle 100 \rangle$ tensile specimens tested at a) 427, b) 649, and c) 871°C (strain rate = 2.3×10^{-3} /s).

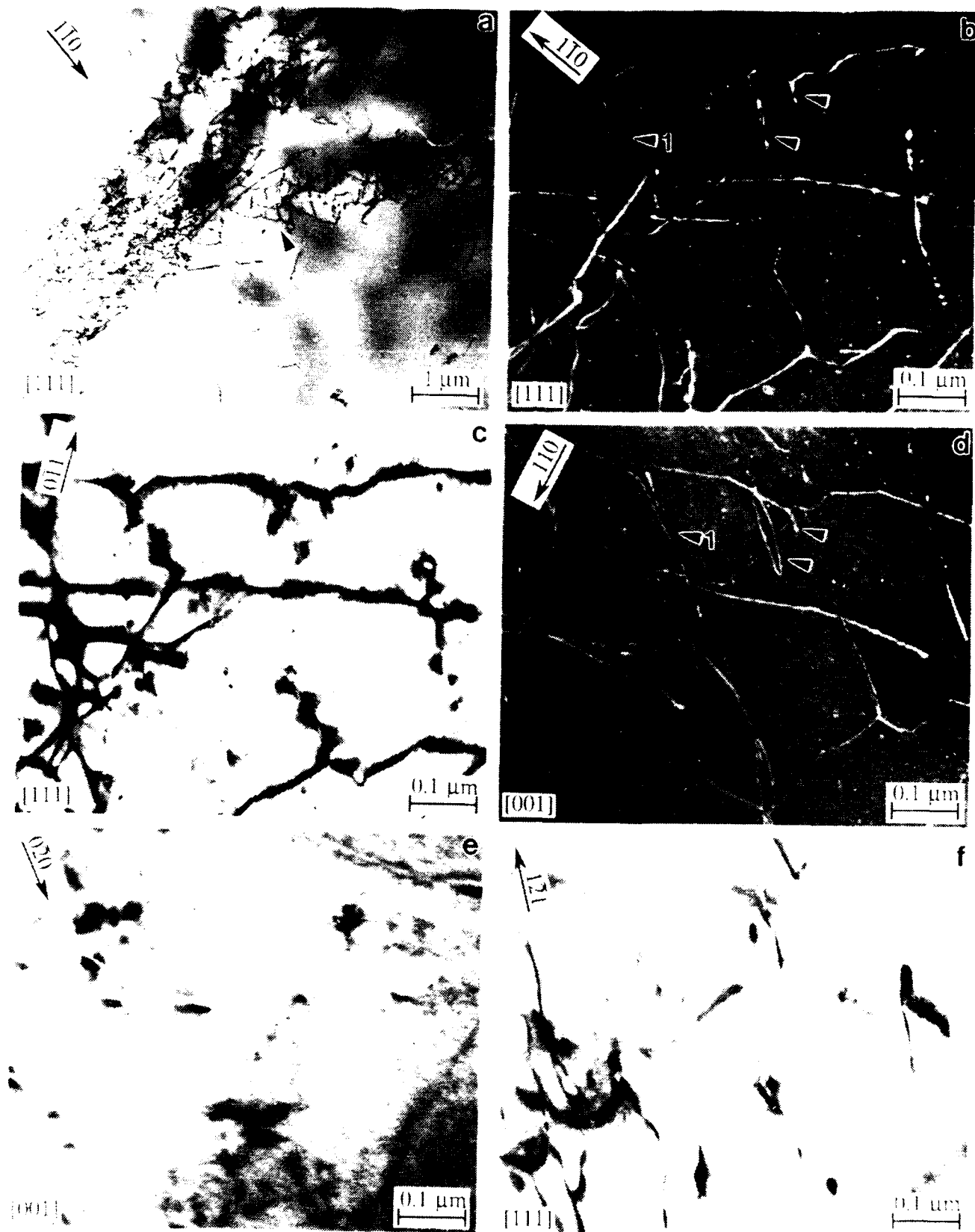


Figure 17. Bright field (a, c, e, f) and weak beam (b, d) TEM micrographs of an $[001]$ oriented tensile specimen tested at 427°C to 0.5% plastic strain (strain rate = $8.3 \times 10^{-5}/\text{s}$). The arrow in the low magnification image of (a) shows the area analyzed in subsequent micrographs (note that there is an $\sim 180^{\circ}$ rotation between the low and high magnification micrographs). Loops with $\mathbf{b}=[100]$, marked with arrows in (b) and (d), are seen trailing $\mathbf{b}=[10\bar{1}]$ dislocations which are bowed out on (101) planes. See text for details.

5. Results from Investigations of Alloying Effect on APB Energy

As discussed in Section IVA, the band structure calculations predict a significantly lower value of APBE (250 mJ/m²) when vanadium substitutes on the nickel site, and still a marked decrease in APBE when V is substituted on the Al site (550 mJ/m²). Examination of the Ni-Al-V phase diagram [43], along with the reported existence of a Ni₂AlV Heusler phase [30], indicates that vanadium substitutes for aluminum. In order to determine the site occupancy of the V atoms in the NiAl structure, ALCHEMI experiments were performed in the TEM using a {100} superlattice reflection. As shown in Table XI, EDS spectra taken at positive and negative deviations from Bragg (s_g) reveal that the intensity of the Al peak relative to that of Ni is increased for positive s_g , consistent with the lower atomic number of Al [39]. The V peak intensity is also seen to increase in spectra recorded under positive s_g conditions. The peak intensity ratios reveal that the V intensity "follows" that of the Al, so that the I_V/I_{Al} ratio remains relatively unchanged with the change in diffracting condition, while the I_V/I_{Ni} ratio shows a two-fold increase for positive versus negative s_g . This indicates that the V is sitting on the Al sites. Therefore, alloys with up to 10at% V substituted for Al were produced. Optical observations showed these alloys to be predominantly single phase, as expected from published phase diagrams [43]. In 5 and 10at% V alloys precipitation was observed in specimens tested at 649 and 871°C (see below).

Table XI ALCHEMI EDS Data for V in NiAl

s_g	I_{Ni}	I_{Al}	I_V	I_V/I_{Ni}	I_V/I_{Al}
negative	143354	37725	4738	0.0331	0.126
positive	104643	58292	8032	0.0768	0.138

The V additions to NiAl had a significant effect on mechanical properties. The NiAl+V compression specimens displayed kinking, as did the NiAl specimens, and were more brittle than the stoichiometric NiAl. As seen in Figure 18, the 0.2% compressive yield strength of the NiAl+V alloys increased with increasing vanadium content. This effect was also observed in the tensile specimens. The NiAl+V tensile specimens were considerably stronger and more brittle than stoichiometric NiAl specimens. Both the DBTT and 0.2% YS for the NiAl+V alloys increased with increasing vanadium additions as shown in Figures 19 and 20, respectively. The ductile to brittle transition temperature (DBTT) was substantially increased with vanadium additions.

As in the case of stoichiometric NiAl, the vast majority of the dislocations in the NiAl+V tensile specimens were of the $\langle 100 \rangle$ type. The 5% V specimens also revealed the presence of fine precipitates which apparently formed during testing. A TEM micrograph of the 649°C tensile specimen is given in Figure 21a. Very fine precipitates, of the order of 1 nm, along with some larger particles in the 10 nm range, were observed in this specimen. The larger particles generally were surrounded by $\langle 100 \rangle$ dislocation loops. Faint reflections at the $1/2\langle 111 \rangle$ positions of the B2 structure indicate that the precipitates consist of the Heusler ($L2_1$) phase (see Figure 21b). In

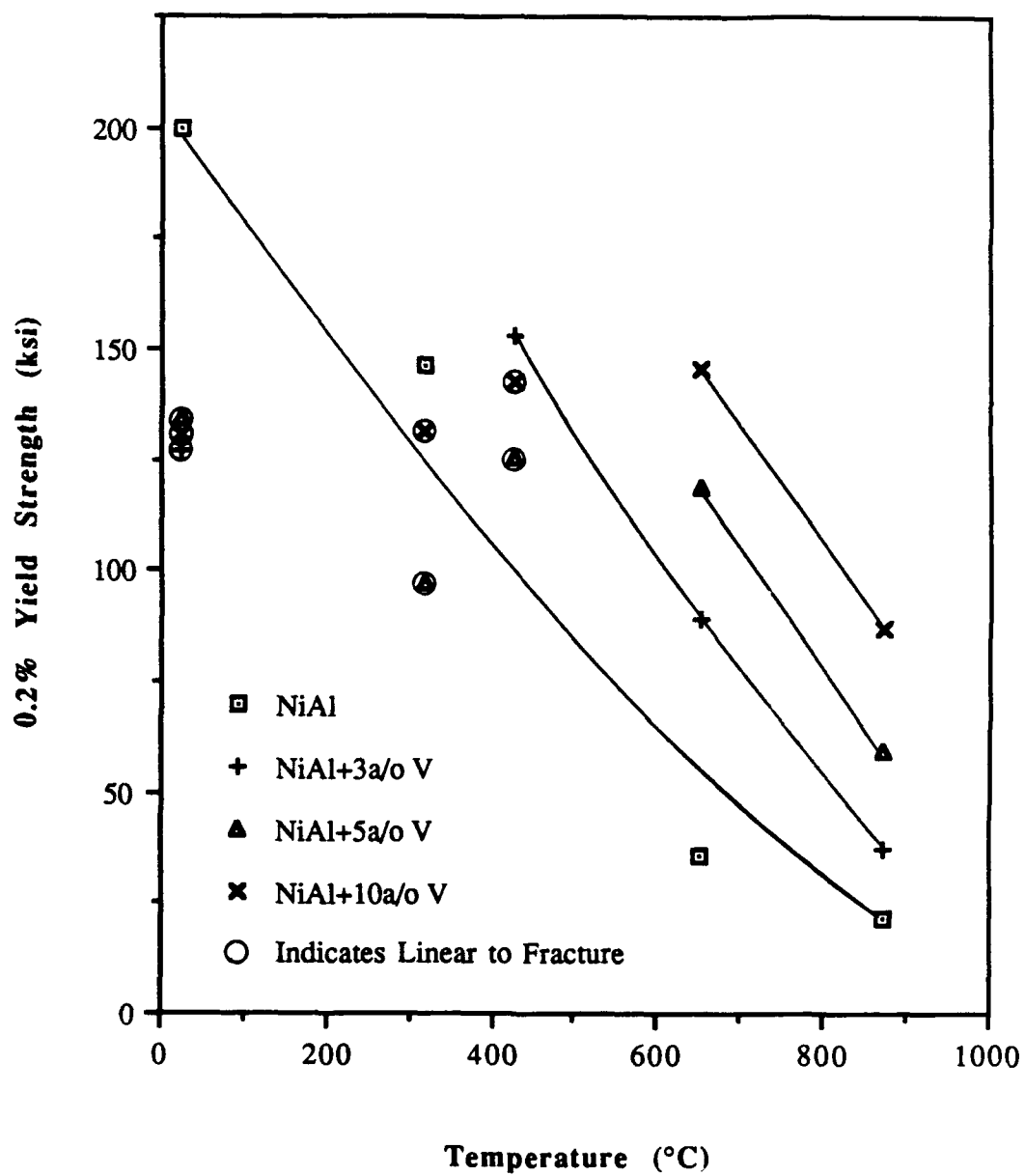


Figure 18. Increasing the vanadium content in NiAl increased the 0.2% compression yield strength.

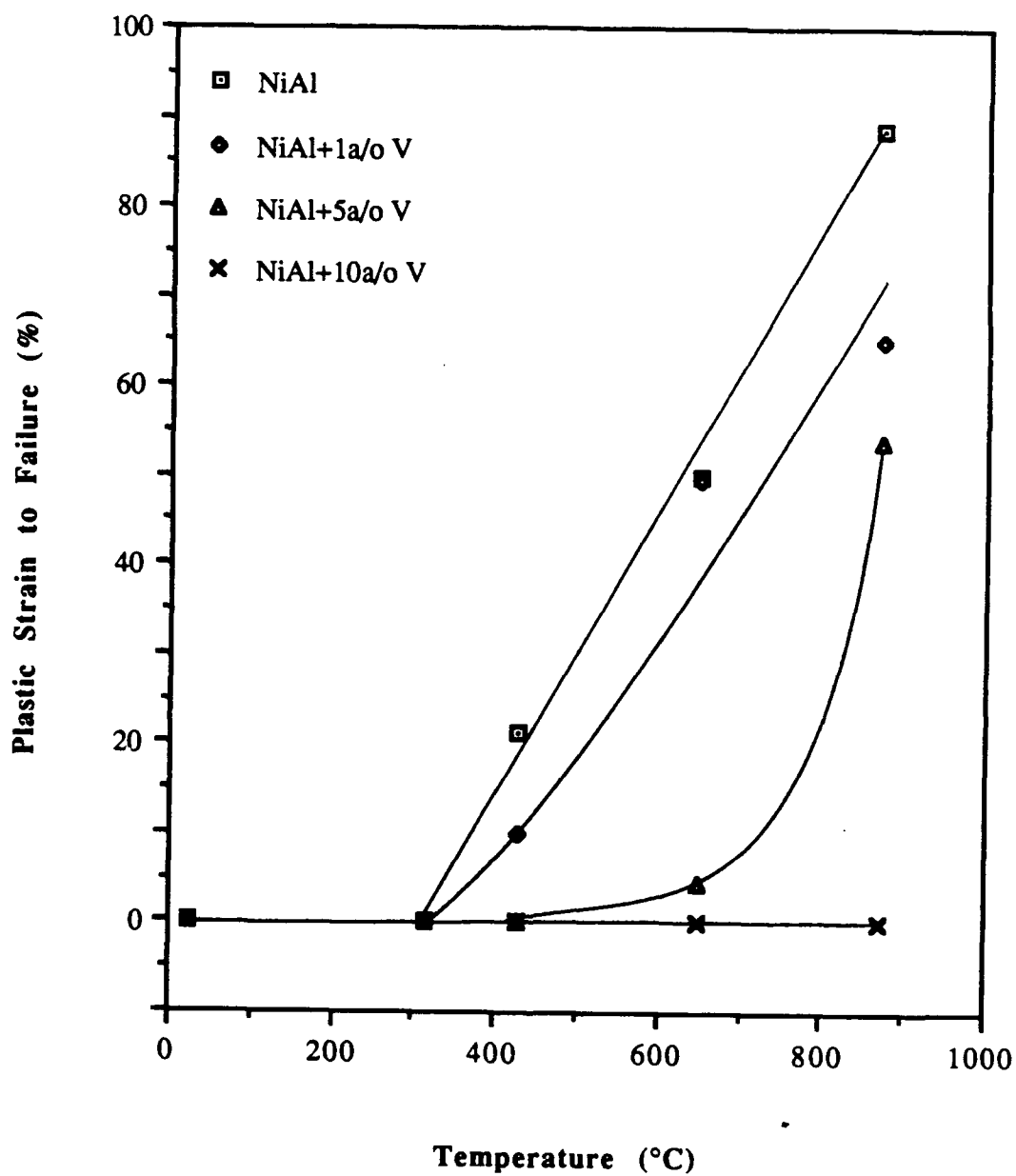


Figure 19. Increasing the vanadium content in NiAl decreased the plastic strain to failure and increased the ductile to brittle transition temperature.

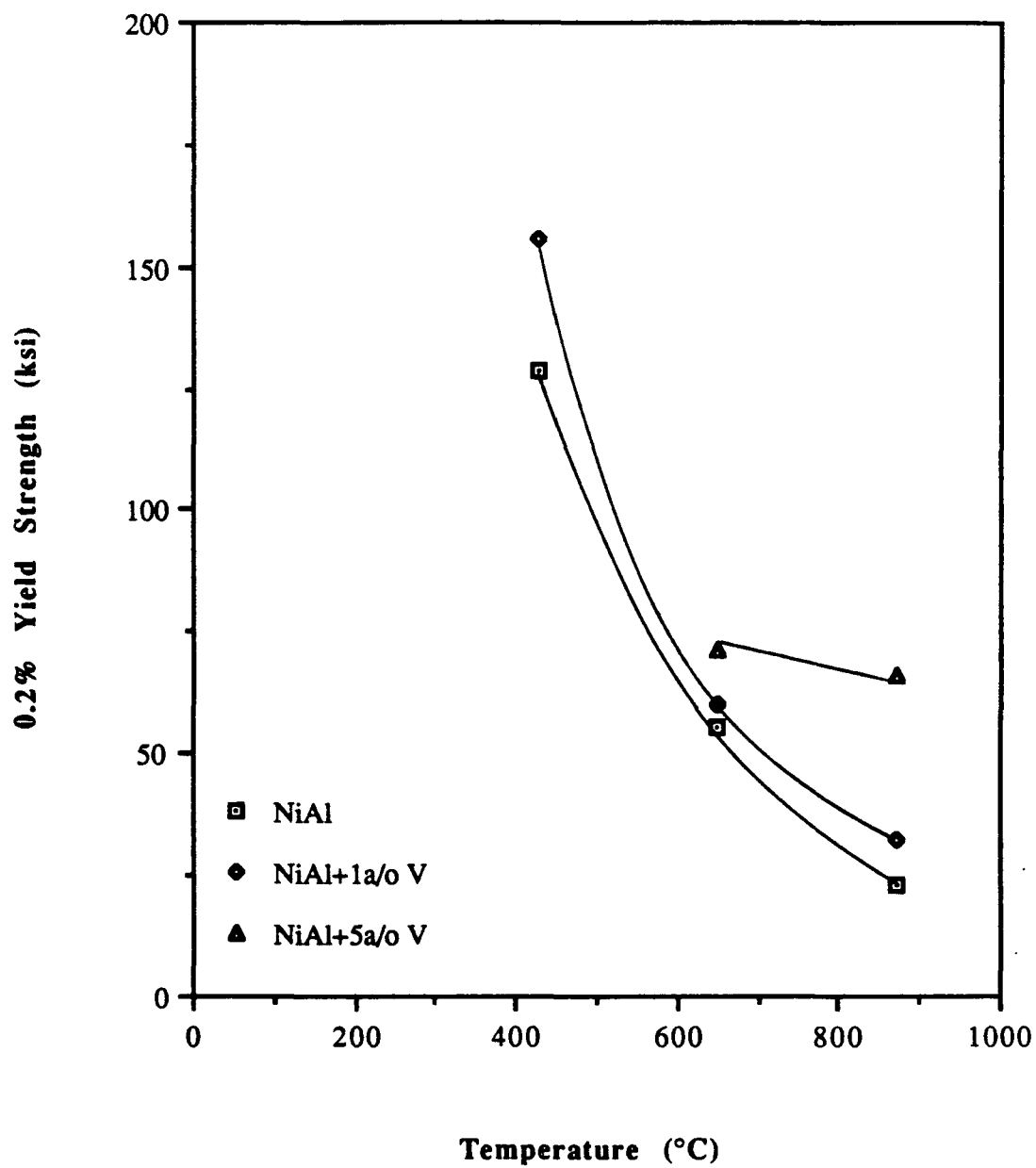
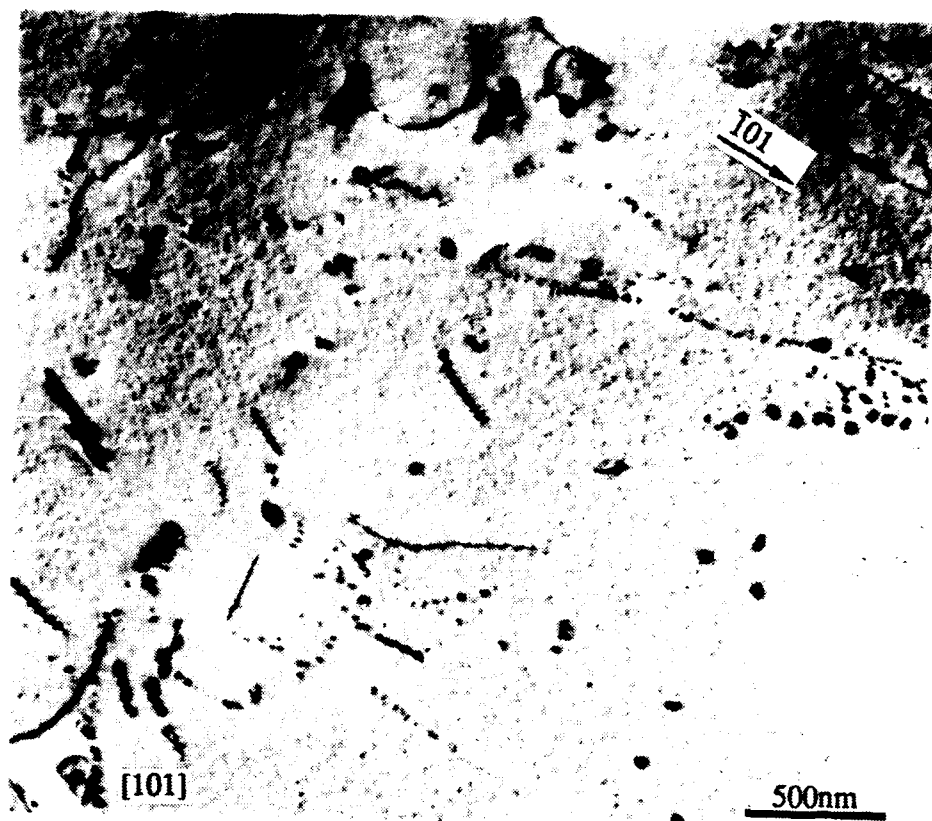
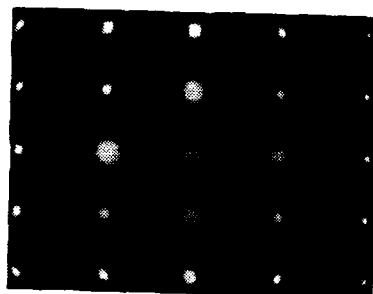


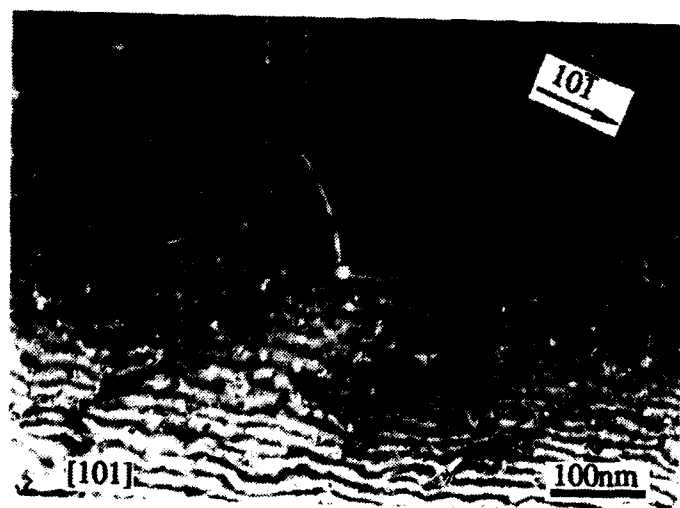
Figure 20. Increasing the vanadium content in NiAl increased the 0.2% tensile yield strength and increased the ductile to brittle transition temperature.



a



b



c

Figure 21. NiAl+5at% V tensile specimens: a) TEM micrograph showing dislocation structure in 649°C specimen, b) $\langle 110 \rangle$ SAD pattern from 649°C specimen showing weak reflections at $1/2\langle 111 \rangle B2$ positions, indicating the presence of Heusler phase, c) Weak beam TEM micrograph of 871°C specimen showing pinning of dislocations by precipitates.

addition, faulted loops were observed on {110} planes. These are believed to be associated with the precipitation reaction, but a complete analysis was not performed. In the 871°C <001> tensile specimen, the number of 10 nm diameter precipitates had increased and they no longer appear to possess an orientation relationship with the matrix. Detailed analysis of these precipitates was not performed. Pinning of the dislocations by the particles was also observed, as seen in Figure 21c.

The addition of Cr to NiAl has been reported to promote the <111> slip vector both on polycrystalline [44] and [001] oriented directionally solidified material [45]. In these studies, the solubility of Cr in the matrix was exceeded, as evidenced by the presence of α -Cr particles. Thus, it is not clear whether the promotion of <111> slip is due to these particles or the Cr in solution. In the current investigation, a systematic study of the Cr effect was conducted, including careful measurements of critical resolved shear stresses (CRSS) for <100> and <111> slip systems in stoichiometric NiAl and alloys containing three different levels of Cr. In addition, an alloy containing 0.45at% Ti and 0.05at% Zr was evaluated.

A 45.15Ni - 49.1Al - 5.75Cr (in at%) alloy was initially prepared. This composition is similar to that studied in previous investigations [44,45]. It was found to contain α -Cr particles having a cube-on-cube orientation relationship with the matrix and a very small lattice mismatch. The mismatch value can be estimated to be approximately 0.8% from the spacings of dislocation nets at the α -Cr/matrix interface, which form to accommodate the mismatch strain. Previous investigations of the NiAl/Cr system have identified the interface nets as consisting of square arrays of $\mathbf{b}=\langle 100 \rangle$ dislocations [46]. Hexagonal arrays were observed, but not analyzed. In the current investigation, these hexagonal arrays were analyzed, and found to consist of $\mathbf{b}=\langle 100 \rangle$ and $\mathbf{b}=1/2\langle 111 \rangle$ dislocations, as presented in Figures 22 and 23. Figures 22a-22d show crossed $\mathbf{b}=[100]$ and $[010]$ edge dislocations, with dissociations into $\mathbf{b}=1/2\langle 111 \rangle$ segments as the interface curves away from the (001) plane. The extensions of the net to the upper right (as viewed in a-d) are visible in Figures 22e-22g. Two invisibilities for the $[100]$, $[010]$, $[111]$, and $[1\bar{1}\bar{1}]$ segments provide positive identification of these Burgers vectors. The $[1\bar{1}\bar{1}]$ and $[\bar{1}11]$ Burgers vectors are determined from single invisibilities and from consideration of nodal reactions within the networks. These interfacial networks may serve as sources for $\mathbf{b}=\langle 111 \rangle$ dislocations during deformation, provided the $\mathbf{b}=1/2\langle 111 \rangle$ dislocations can combine to form $\mathbf{b}=\langle 111 \rangle$ segments and escape from the interface networks. After being strained in compression along $[001]$, $\mathbf{b}=\langle 111 \rangle$ dislocations were observed in the matrix and were associated with α -Cr particles. However, there was no conclusive evidence, such as the observation of $\mathbf{b}=\langle 111 \rangle$ dislocations bowing out from the interface nets into the matrix, that the particle/matrix interfaces served as sources for these dislocations (see Figure 24).

In order to separate the effects of the α -Cr precipitates from those of the Cr in solution, alloys with lower Cr levels were prepared. A 2at% Cr alloy (50Ni - 48Al - 2Cr, in at%), solution heat treated for 50 hours at 1316°C, is shown in Figure 25. Although the number of large, undissolved primary precipitates was considerably reduced, this alloy does contain a fine dispersion of α -Cr precipitates. The precipitates are approximately 40nm in diameter and were found to possess the

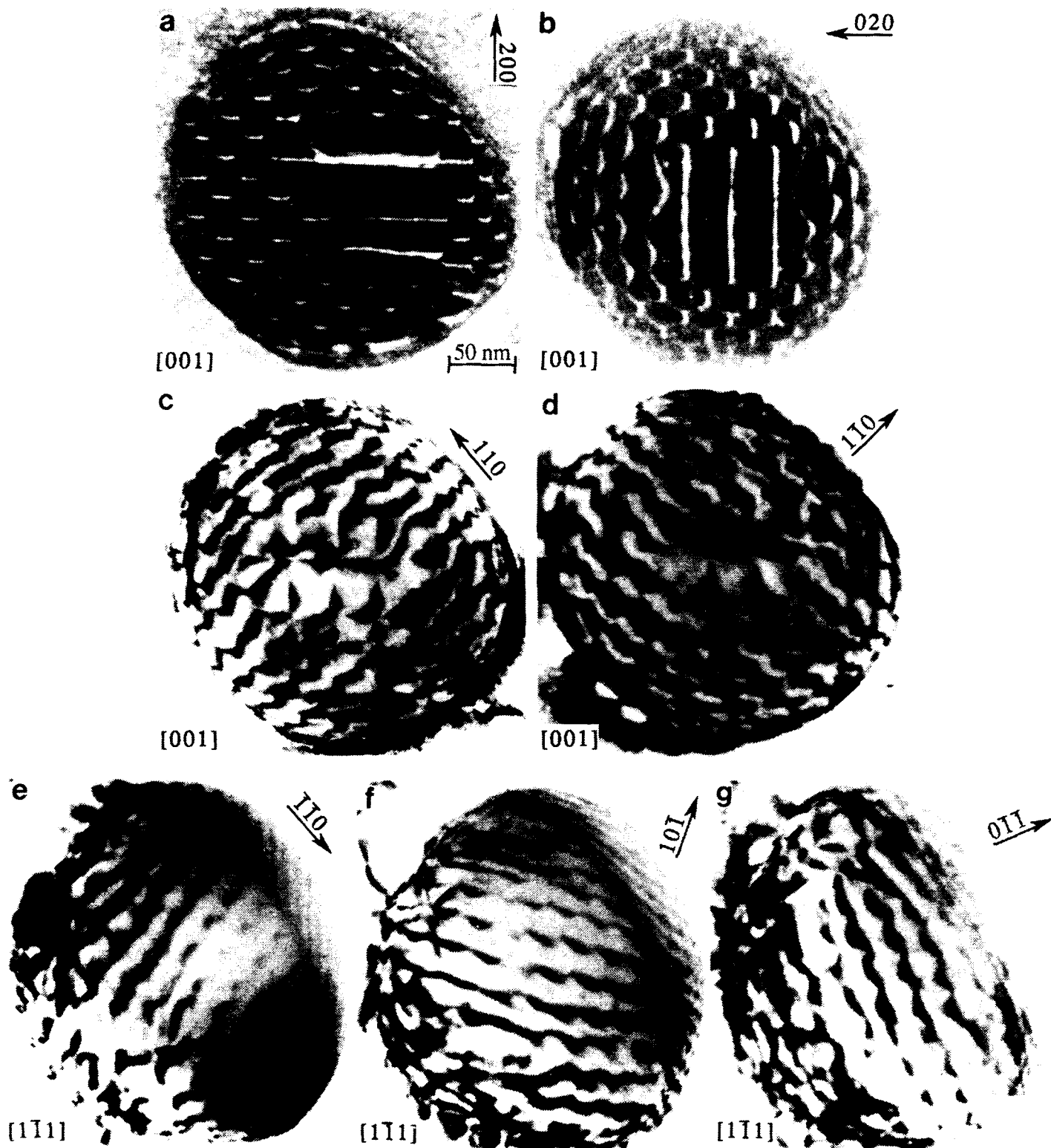


Figure 22. Dislocation array observed on the interfaces of α -Cr precipitates in the 5.75at% Cr alloy. a) and b) are weak beam TEM micrographs, the remainder are bright field TEM micrographs. Note that the foil has been tilted in (e)-(g), so that the central area of (a)-(d), containing the square arrays of $\mathbf{b}=[100]$ and $\mathbf{b}=[010]$ dislocations, is now on the lower left side of the particle image.

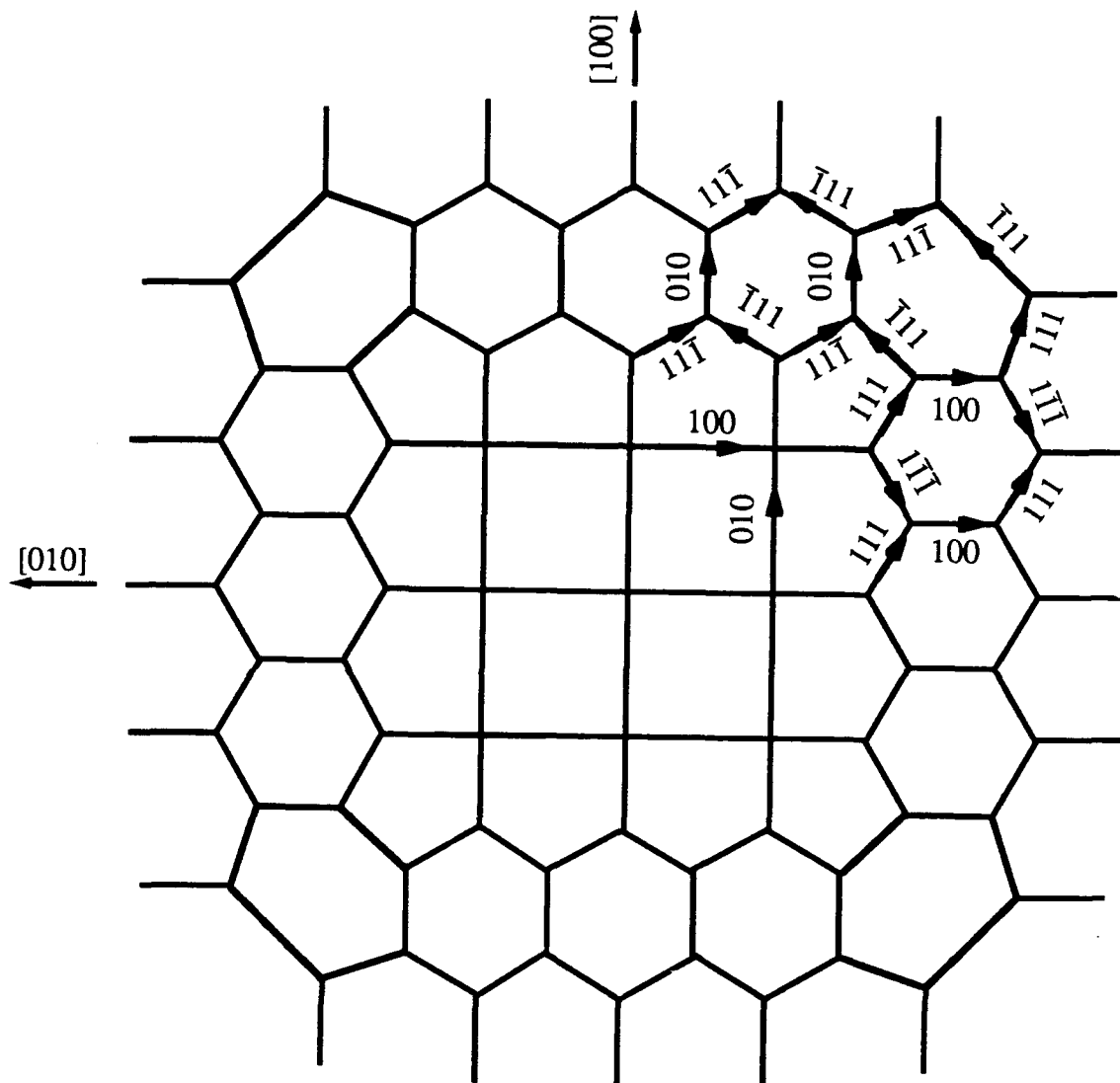


Figure 23. Schematic representation of the interfacial dislocation array shown in Figure 22. The actual dislocation array shown in Figure 22 differs slightly from this idealized version; however, the fundamental nature of the net is the same. The net lies on a (001) plane, with the $[100]$ and $[010]$ direction are indicated on the drawing. The dislocations labeled $\langle 111 \rangle$ actually possess $1/2\langle 111 \rangle$ Burgers vectors.

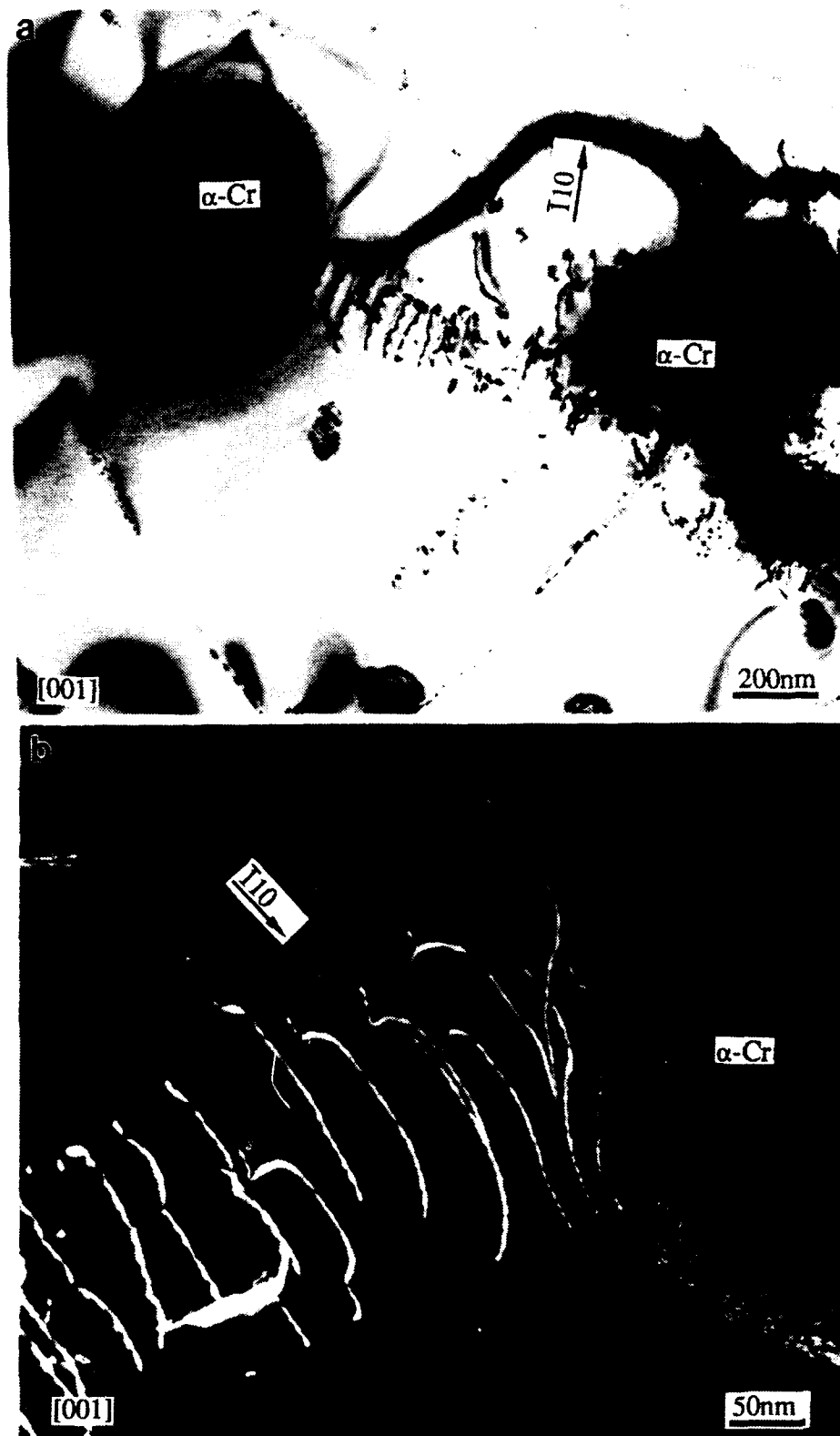


Figure 24. Bright field (a) and high magnification weak beam (b) TEM micrographs showing $b=\langle 111 \rangle$ dislocations and α -Cr precipitates in a RT $[001]$ compression tested 5.75at% Cr specimen. Note that the dislocations in (b) appear to be moving toward the particle, as evidenced by the direction of bowing.



Figure 25. Fine cooling α -Cr precipitates in the NiAl matrix of the 2at% Cr alloy.

same cube-on-cube orientation relationship with the matrix as do the larger particles in the 5.75at%Cr alloy. The small size of the precipitates indicates that the 2at% Cr is in solution at the heat treatment temperature, but the alloy becomes supersaturated during cooling. EDS analysis in the analytical electron microscope (AEM) determined the remaining Cr in the matrix to be approximately 1at%. Subsequently, a 1at% Cr alloy (50Ni - 49Al - 1Cr, in at%) was prepared which does not contain the fine dispersion.

Table XII ALCHEMI EDS Data for Cr in NiAl

Sg	I _{Ni}	I _{Al}	I _{Cr}	I _{Cr} /I _{Ni}	I _{Cr} /I _{Al}
negative	160639	51692	2020	0.0126	0.0391
positive	102603	72466	2468	0.0241	0.0341

Results from an ALCHEMI experiment, using a {100} superlattice reflection, are presented in Table XII, where peak intensities for spectra recorded under both positive and negative deviations from the Bragg condition (sg) are listed. As in the case of V presented above, the peak intensity ratios reveal that the Cr intensity "follows" that of the Al, so that the I_{Cr}/I_{Al} ratio remains relatively unchanged with the change in diffracting condition, while the I_{Cr}/I_{Ni} ratio shows a two-fold increase for positive versus negative sg. This indicates that the Cr is sitting on the Al sites.

Compression testing as a function of temperature was performed on 1at% Cr 3/1 L/D ratio specimens. Three specimens were tested at room temperature (RT), and one specimen for each temperature at 316, 427, 649, and 871°C. The 316 and 427°C specimens displayed kinking. The degree of kinking was reduced at 427°C, and some uniform deformation was observed at this temperature. Barreling, with no observed kinking, occurred at RT, 649, and 871°C. This was not the case for stoichiometric NiAl compression specimens, which kinked to some degree at all temperatures. As will be discussed below, the absence of kinking for the RT specimen is believed to arise from a different mechanism from that active at high temperatures. The 0.2% YS values for the chromium containing alloy are shown in Figure 26, along with values for stoichiometric NiAl. The strain rates used for the two alloys were slightly different; however, RT tests for NiAl tested at 8.3x10⁻⁵/s gave similar values to those obtained at the slower strain rate. RT compression specimens with 2/1 L/D ratios were also tested in [001] and $\bar{1}10$ orientations for both the NiAl and 1% Cr alloys. Strength values from these tests were consistent with those obtained from the longer specimens.

RT compression testing was also performed on 0.05at% and 0.2at% Cr specimens (with the Cr substituted for Al). Two specimens of each orientation and length were tested. Both of the 0.2at% Cr 3/1 specimens and one of the 0.05at% Cr 3/1 specimens kinked during testing. A limited amount of kinking was observed in one of the two 2/1 specimens, near the ends, for each

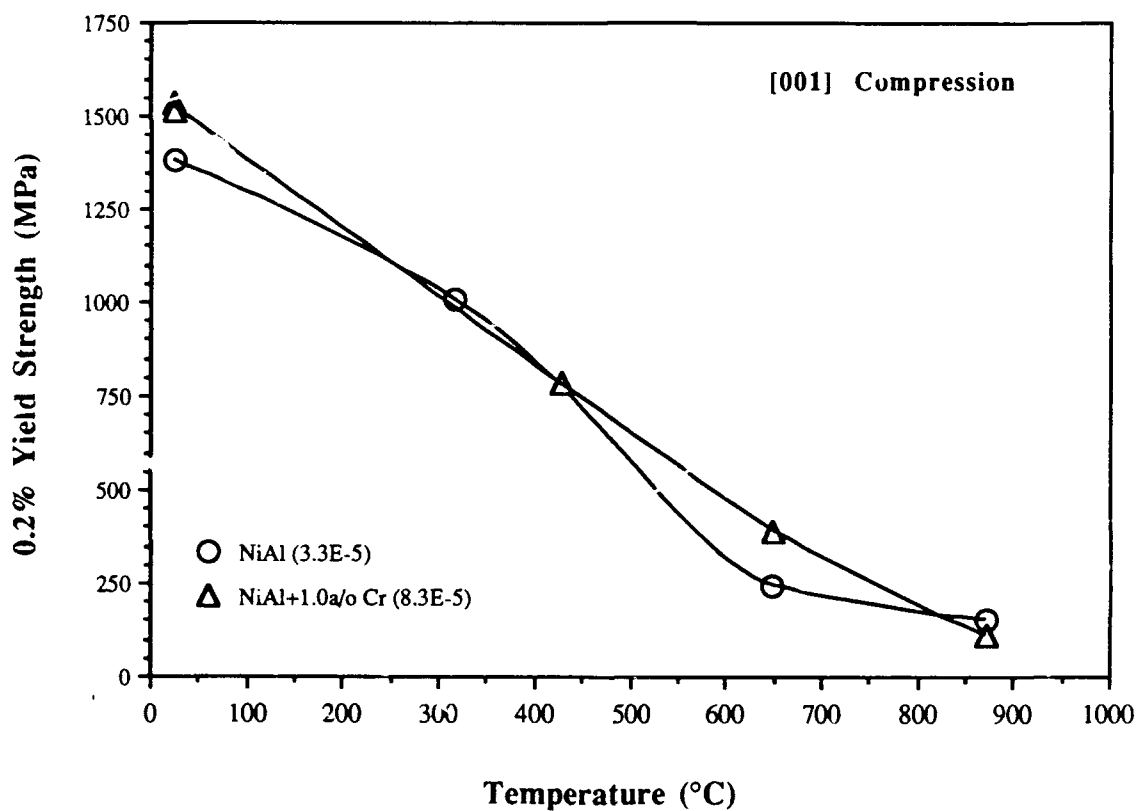


Figure 26. 0.2% compression yield strength as a function of temperature for stoichiometric NiAl and the 1% Cr alloy in the [001] orientation. The strain rate was 3.3×10^{-5} /s for the NiAl specimens and 8.3×10^{-5} /s for the NiAl+Cr specimens. Additional RT tests on NiAl specimens tested at 8.3×10^{-5} /s gave similar yield stress values.

alloy. However, these specimens appear to have an increased resistance to kinking as compared to the 3/1 specimens and stoichiometric NiAl specimens of both geometries.

TEM examination of the 3/1 RT compression specimens of the 1at% Cr alloy revealed the presence of broad slip bands containing $\mathbf{b}=\langle 111 \rangle$ dislocations, as shown in Figure 27. The dislocation density was found to be much lower outside these bands, where only $\langle 100 \rangle$ Burgers vectors were observed. The $\mathbf{b}=\langle 111 \rangle$ dislocations are in the form of very straight screw segments connected by more jagged edge sections. This observation is consistent with previous results for $\mathbf{b}=\langle 111 \rangle$ dislocations in RT deformed binary NiAl [16]. Weak beam micrographs taken using several different beam directions did not reveal any dissociation into $1/2\langle 111 \rangle$ superpartials (see Figure 28). The dislocations were found to be lying on $\{112\}$ planes. The nature of these dislocations, their Burgers vectors, slip plane, and lack of resolvable dissociation, is similar to that observed in the stoichiometric NiAl 2/1 specimen. It is interesting to note that binary specimens deformed at 77K exhibit very long screw dipoles, with rare edge segments, when observed normal to the $\{112\}$ slip plane, indicating that the edge segments are more mobile [16]. In the current investigation, RT deformed specimens exhibit a high concentration of edge dipoles, although a substantial representation of screw orientation is observed (Figure 29). This indicates a change in the relative mobilities of screw versus edge with the increase in temperature. At high temperatures, dislocation structures were similar to those observed in the binary specimens, including the observation of dislocations with $\langle 110 \rangle$ Burgers vectors bowed out on $\{110\}$ slip planes (see Figure 30). Thus, $\langle 111 \rangle$ slip was not found to persist at higher temperatures. TEM examination of the $[001]$ oriented RT compression specimens of the 0.05at% and 0.2at% Cr alloys also revealed the presence of $\mathbf{b}=\langle 111 \rangle/\{112\}$ slip bands, similar to those observed in the stoichiometric and 1at% Cr specimens.

The fact that the $\mathbf{b}=\langle 111 \rangle$ dislocations are confined to distinct bands implies that they are being emitted from widely spaced heterogeneous sources. SEM/EDS examination of the specimens revealed the presence of Cr-rich particles. Several of these were located in the TEM by repeated ion milling and subsequent examination. They were found to be the orthorhombic Cr_7C_3 phase by electron diffraction analysis (see Figure 31). Both polycrystalline and single crystal carbide particles were observed. The single crystal carbides were often found to be associated with the slip bands. An example is shown in Figure 32, in which a carbide particle is shown within a slip band of $\mathbf{b}=[11\bar{1}]$ dislocations. The orientation relationship with the matrix for the single crystal carbides is:

$$\begin{aligned} [100]_{\text{ppt}} &\parallel [011]_{\text{matrix}} \\ (001)_{\text{ppt}} &\parallel (11\bar{1})_{\text{matrix}} \end{aligned}$$

Thus, the $[001]$ of the carbide is aligned with the observed $[11\bar{1}]$ slip direction. This interface may serve as a source for the $\mathbf{b}=\langle 111 \rangle$ dislocations in the matrix, bringing about the change in slip system. If this was the case, each carbide would be expected to emit only one type of $\mathbf{b}=\langle 111 \rangle$ dislocation, ie. the $\langle 111 \rangle$ which is aligned with the $[001]$ of the carbide. As shown in Figure 33,

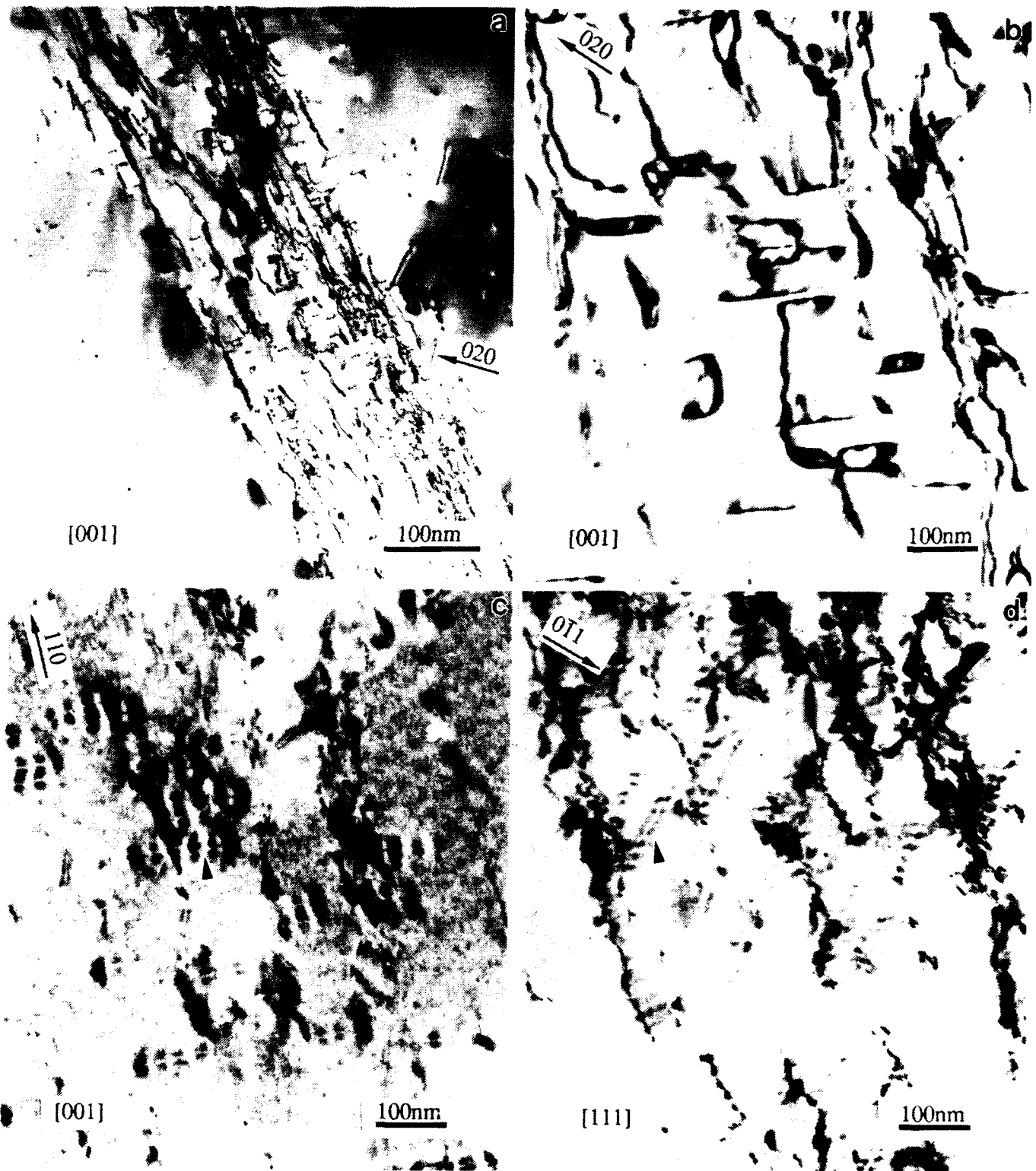


Figure 27. Broad slip band containing $\mathbf{b}=[\bar{1}11]$ dislocations lying on a $(1\bar{1}2)$ plane observed in a $[001]$ oriented 1at% Cr specimen, tested in RT compression to 0.8% plastic strain. The arrows in (c) and (d) show dislocations displaying residual contrast.

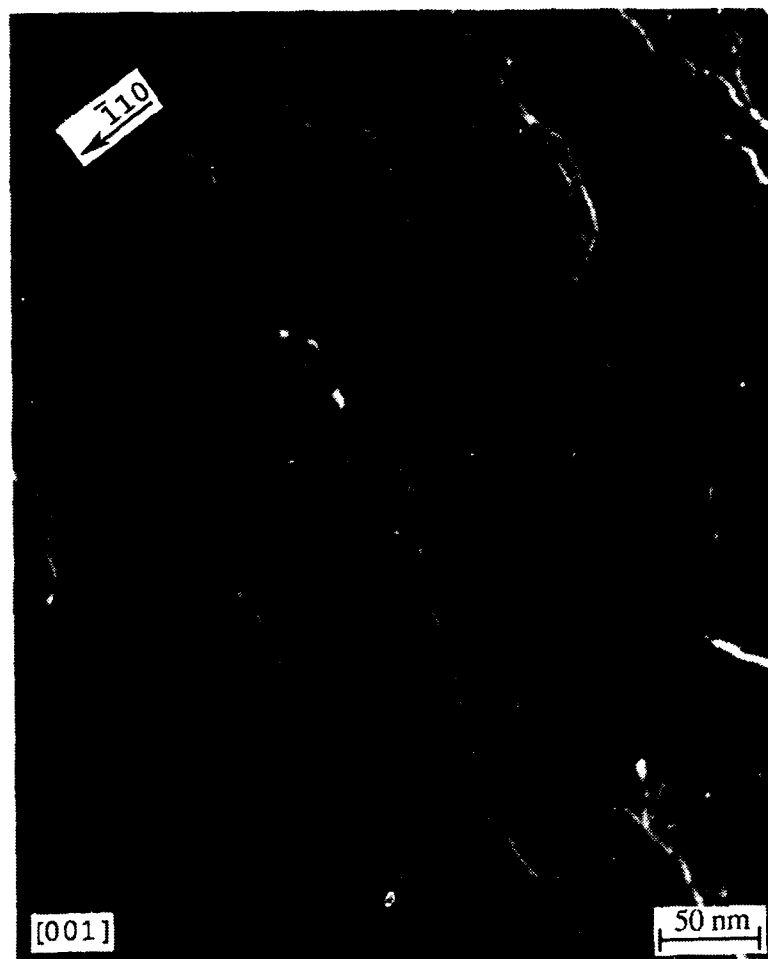


Figure 28. Weak beam micrograph of $\mathbf{b}=[\bar{1}11]$ dislocations inside the dislocation band shown in Figure 27. No dissociation into $1/2[\bar{1}11]$ superpartials is resolved.

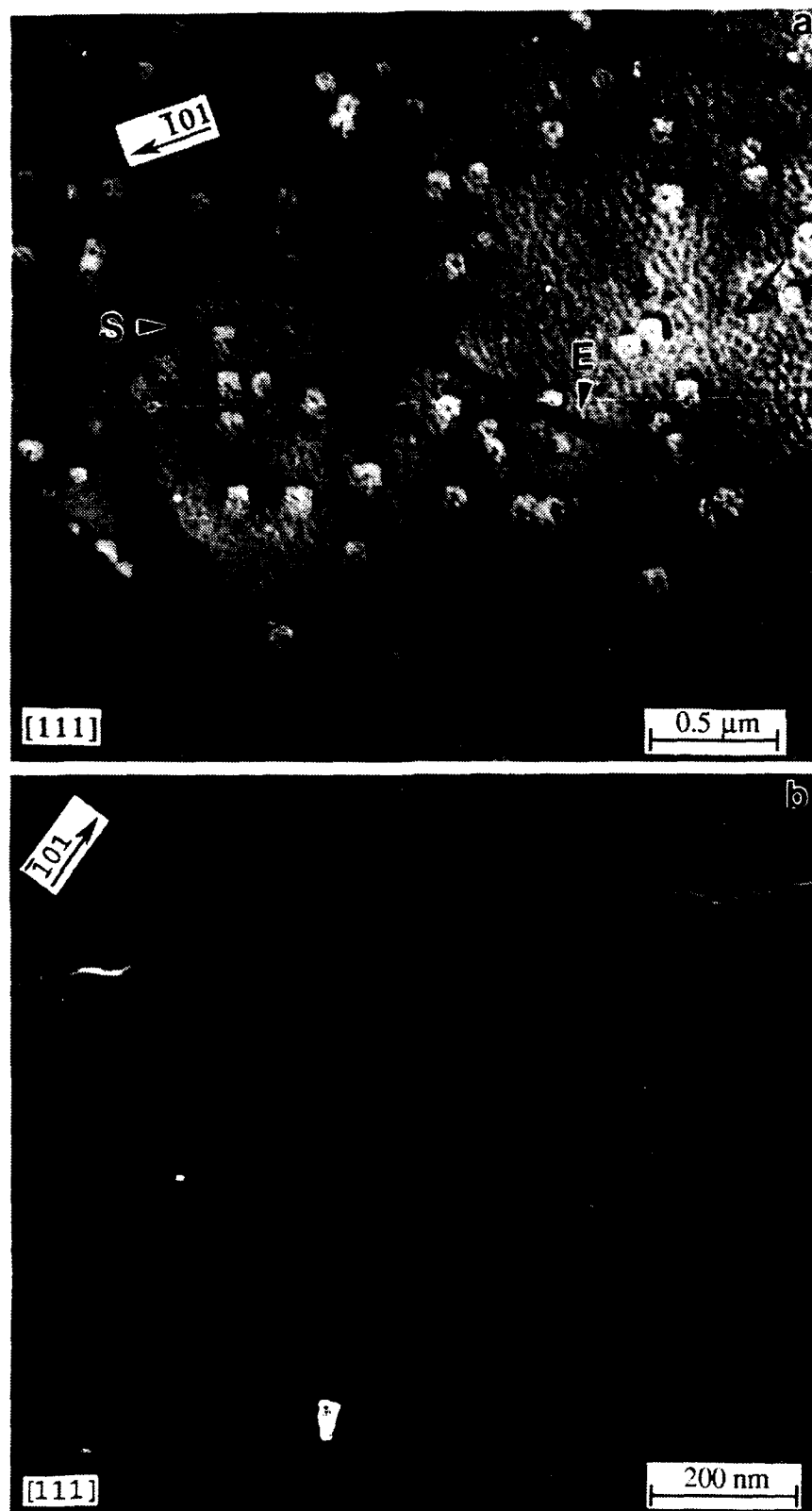


Figure 29. Bright field (a) and weak beam (b) micrographs of $\mathbf{b}=\langle 111 \rangle$ dislocations observed in an $[001]$ oriented 1at% Cr specimen, tested in RT compression to 1.5% plastic strain, showing screw (S) and edge (E) segments. The specimen was cut along a $\{112\}$ plane so that dislocations could be viewed on the slip plane.

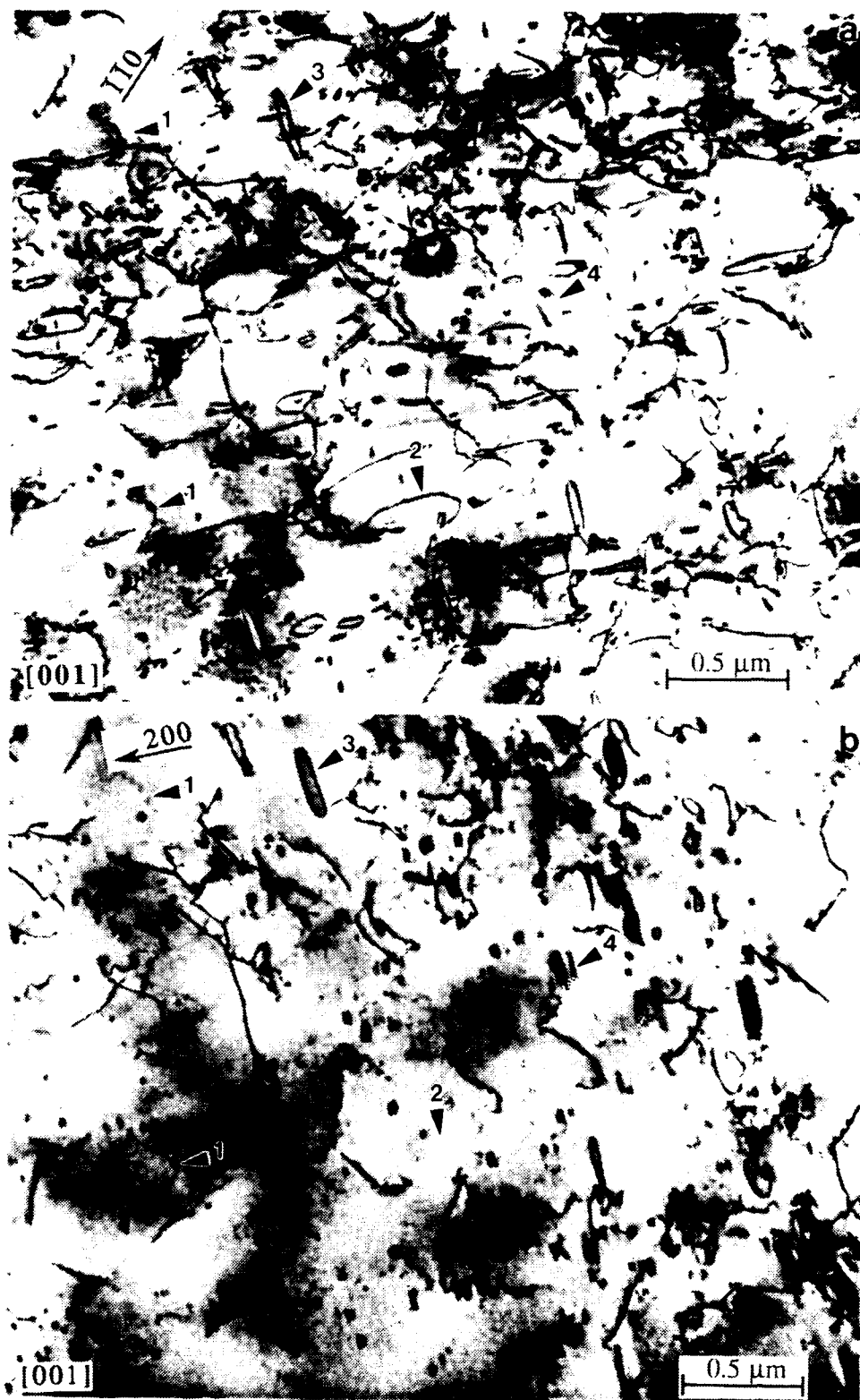


Figure 30. TEM micrographs of a [001] oriented 1at% Cr specimen, tested in compression at 649°C to 0.8% plastic strain, showing predominantly $b=\langle 100 \rangle$ dislocations with some bowed out $b=[011]$ dislocations. The $b=[011]$ dislocations (1) are out of contrast in (b) and (d), the $b=[010]$ dislocations (2) are out of contrast in (b) and (c), the $b=[100]$ dislocations (3) are out of contrast in (d), and the $b=[001]$ dislocations (4) are out of contrast in (a) and (b).

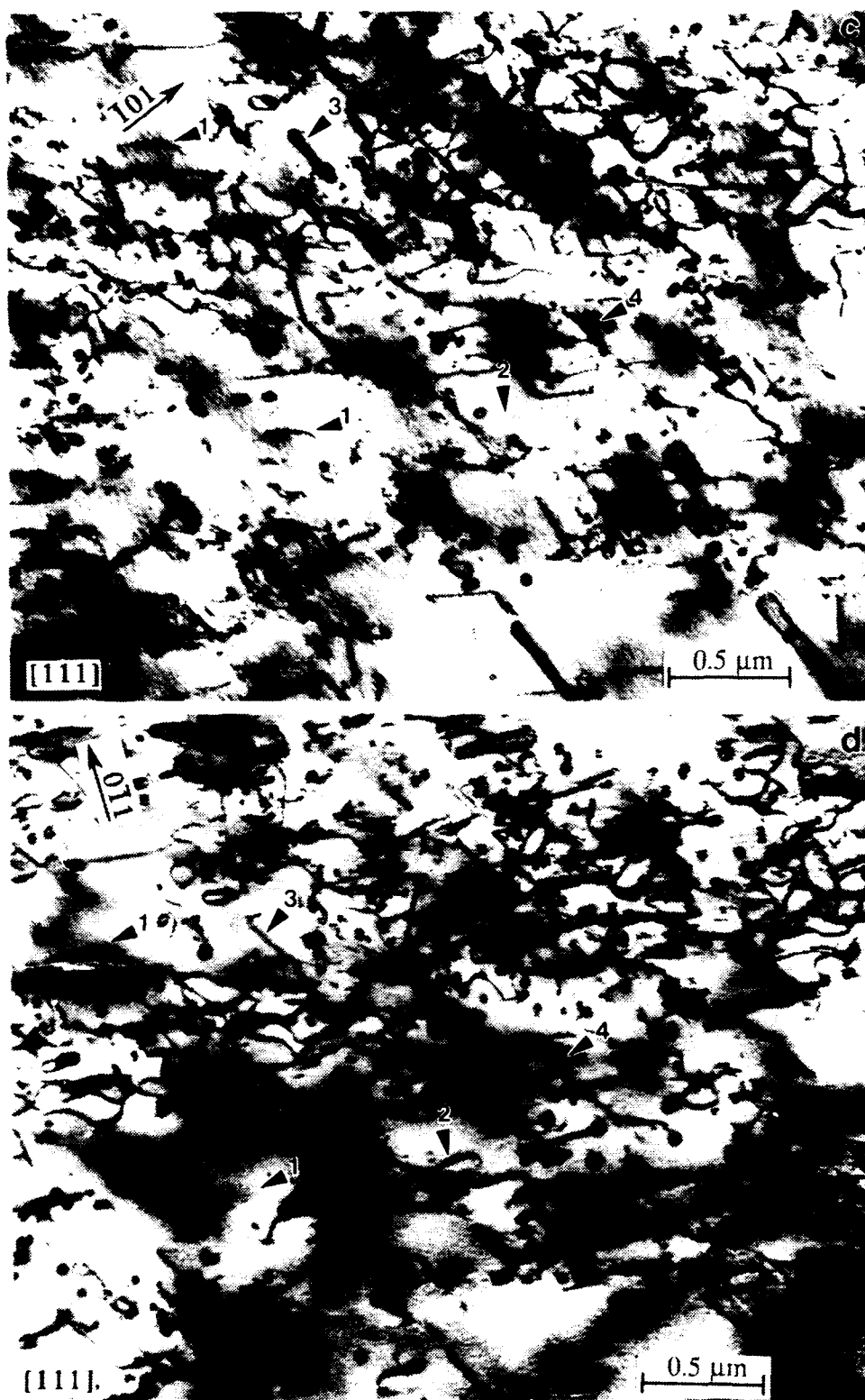


Figure 30 (cont). TEM micrographs of a [001] oriented 1at% Cr specimen, tested in compression at 649°C to 0.8% plastic strain, showing predominantly $\mathbf{b}=\langle 100 \rangle$ dislocations with some bowed out $\mathbf{b}=[011]$ dislocations. The $\mathbf{b}=[011]$ dislocations (1) are out of contrast in (b) and (d), the $\mathbf{b}=[010]$ dislocations (2) are out of contrast in (b) and (c), the $\mathbf{b}=[100]$ dislocations (3) are out of contrast in (d), and the $\mathbf{b}=[001]$ dislocations (4) are out of contrast in (a) and (b).

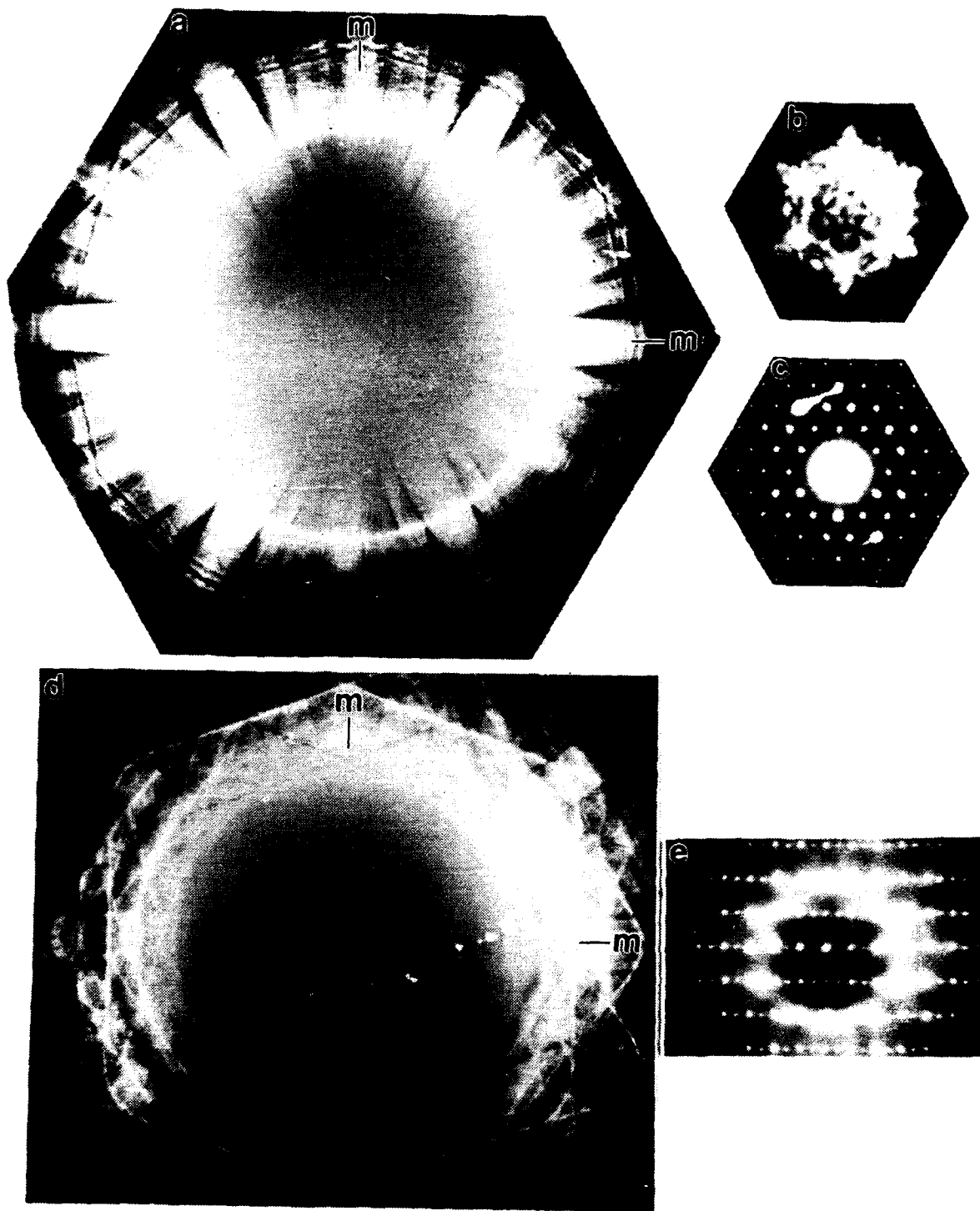


Figure 31. Diffraction data from a Cr_7C_3 particle found in the 1at% Cr alloy. a) and b) are convergent beam electron diffraction (CBED) patterns from the $[100]$ zone axis. c) is a selected area diffraction (SAD) pattern from the $[100]$. d) and e) are CBED and SAD patterns, respectively, of the $[020]$ zone axis.



Figure 32. An example of a single crystal carbide associated with slip bands in a [001] oriented 1at% Cr specimen, tested in RT compression to 0.8% plastic strain.

two different $b=\langle 111 \rangle$ dislocations were sometimes observed being emitted from a single carbide particle. Therefore, although the carbides appear to be acting as dislocation sources, they do not appear to be responsible for the change in slip system from $\langle 100 \rangle$ to $\langle 111 \rangle$. In fact, instances of alumina particles emitting $b=\langle 111 \rangle$ dislocations were also observed in these specimens.

The 1at% Cr containing alloy behaved similarly to stoichiometric NiAl in tension with respect to the temperature dependence of ductility. The Cr containing [001] tensile specimens failed without yielding at room temperature and 316°C. As with stoichiometric NiAl specimens tested at 427 and 649°C, the corresponding chromium containing specimens underwent yielding followed by a yield drop. The 871°C specimen did not show any yield drop after the initial yielding. As can be seen in Figure 34a, the 1at% Cr addition has no effect on the DBTT. Figure 34b shows 0.2% yield strength as a function of temperature. Some increase in strength is observed compared to stoichiometric NiAl. The strengthening effect at elevated temperatures was not seen in the compression data. This apparent difference in compression versus tensile behavior is not understood.

The presence of Cr_7C_3 precipitates in the 1at%Cr alloy, and the effectiveness of low levels of Cr on reducing kinking, suggests that C gettering by the Cr may be responsible for the promotion of $\langle 111 \rangle$ slip in Cr containing alloys. In order to determine the effect of C gettering on slip behavior, an alloy containing 0.45at%Ti and 0.05at%Zr, both potent C getterers, was tested in RT compression in the form of 3/1 L/D ratio specimens. The specimens yielded without kinking, and subsequent TEM examination revealed the presence of slip bands of $b=\langle 111 \rangle$ dislocations, as shown in Figure 35. Testing of $\langle 110 \rangle$ oriented specimens (in tension) was performed and the alloy was found to have been considerably strengthened at room temperature by the alloy additions (see Table XIV in Discussion).

6. Results from Stress Induced Martensite Study

A survey of the literature was conducted to develop an understanding of the existing data on stress induced martensite (SIM) in NiAl alloys. Good correlation has been found between the calculated results of the calculations and data in the literature on M_s temperatures for NiAl alloys. The increasing stability of the martensitic $L1_0$ phase with increasing Ni content mirrors the plot of M_s temperature as a function of stoichiometry presented in Figure 2. Calculations of the difference in the total energy obtained for ternary and quaternary additions to NiAl were made.

Experimental work to investigate the martensite transformation in NiAl alloys was conducted. Binary alloys in the 49-63 at% Ni range were prepared in the form of single crystals and specimens with faces parallel to {100} and {110} crystallographic planes were obtained from these crystals. These binaries specimens were used to obtain baseline data and to establish the technique to measure the strain induced transformation. The crystals were used to obtain single crystal elastic constants and their temperature dependence from RT to M_s . Data are presented in Table XIII. One

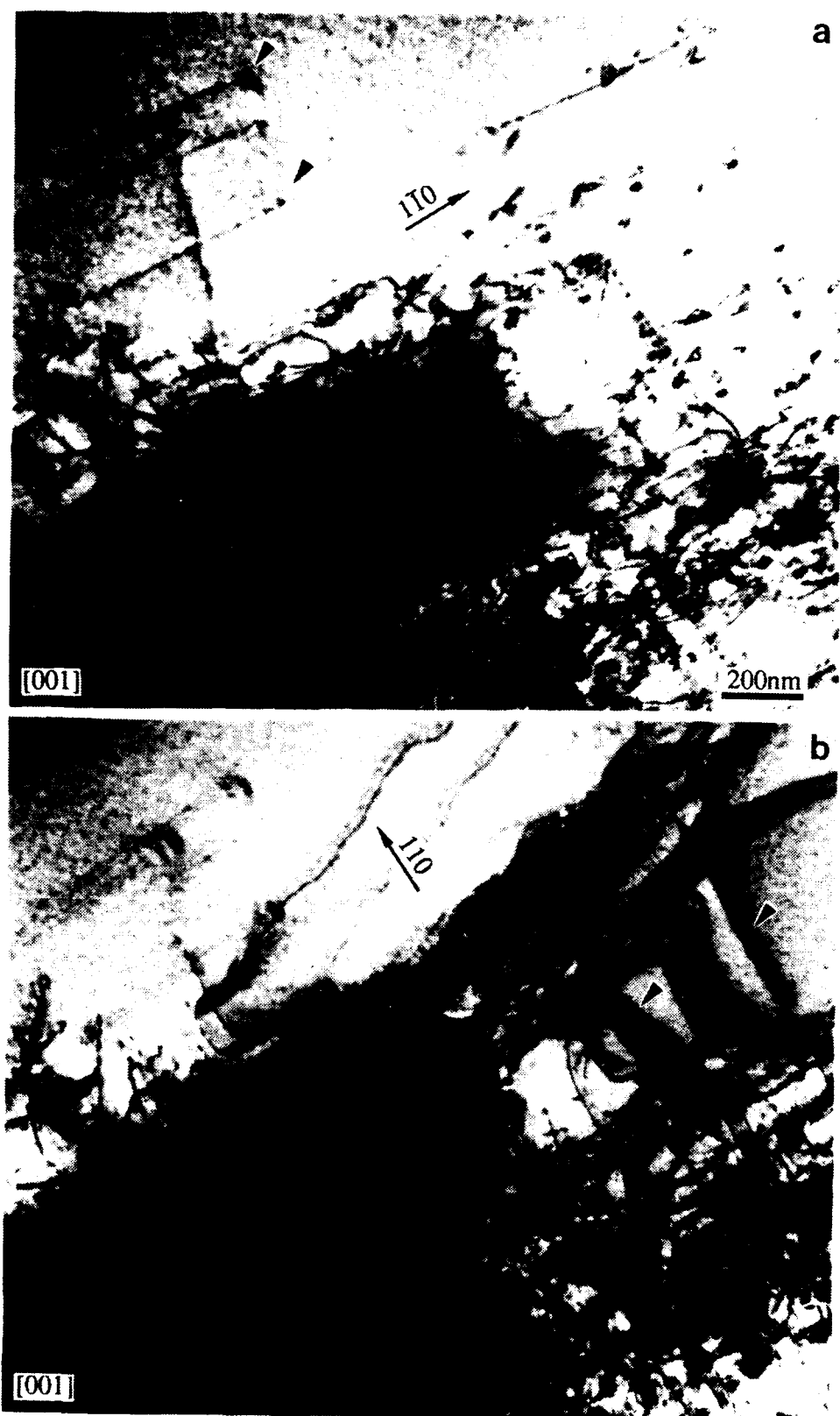
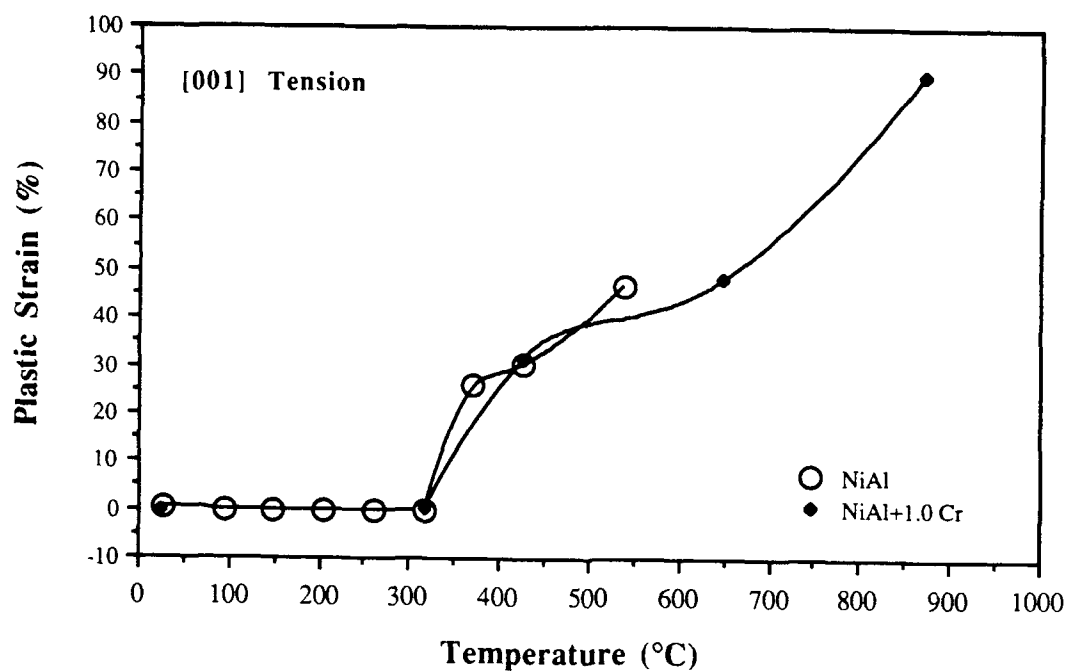
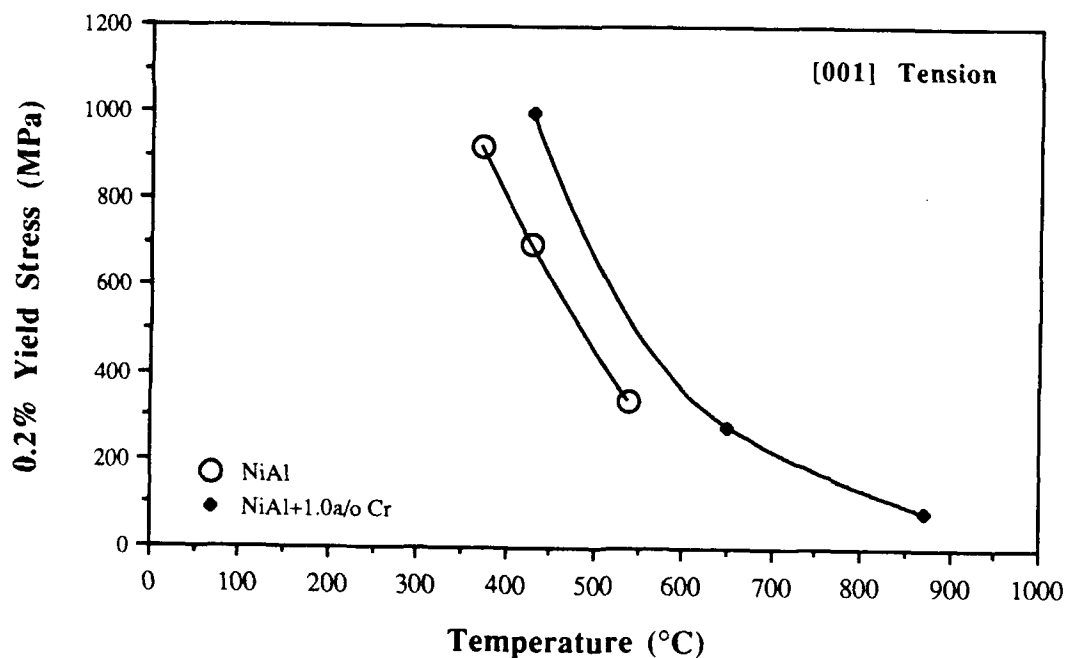


Figure 33. Dislocations with two different $\langle 111 \rangle$ Burgers vectors being emitted from a single crystal carbide particle in a $[001]$ oriented 1at% Cr specimen, tested in RT compression to 0.8% plastic strain. Examples of in contrast $b=\langle 111 \rangle$ dislocations are depicted by arrows.



a



b

Figure 34. (a) Plastic strain to failure and (b) 0.2% yield stress as a function of temperature for stoichiometric NiAl and the 1% Cr alloy in the [001] orientation. The strain rate was 8.3×10^{-5} /s for both alloys. No change in low temperature tensile ductility was observed in the Cr containing specimen.

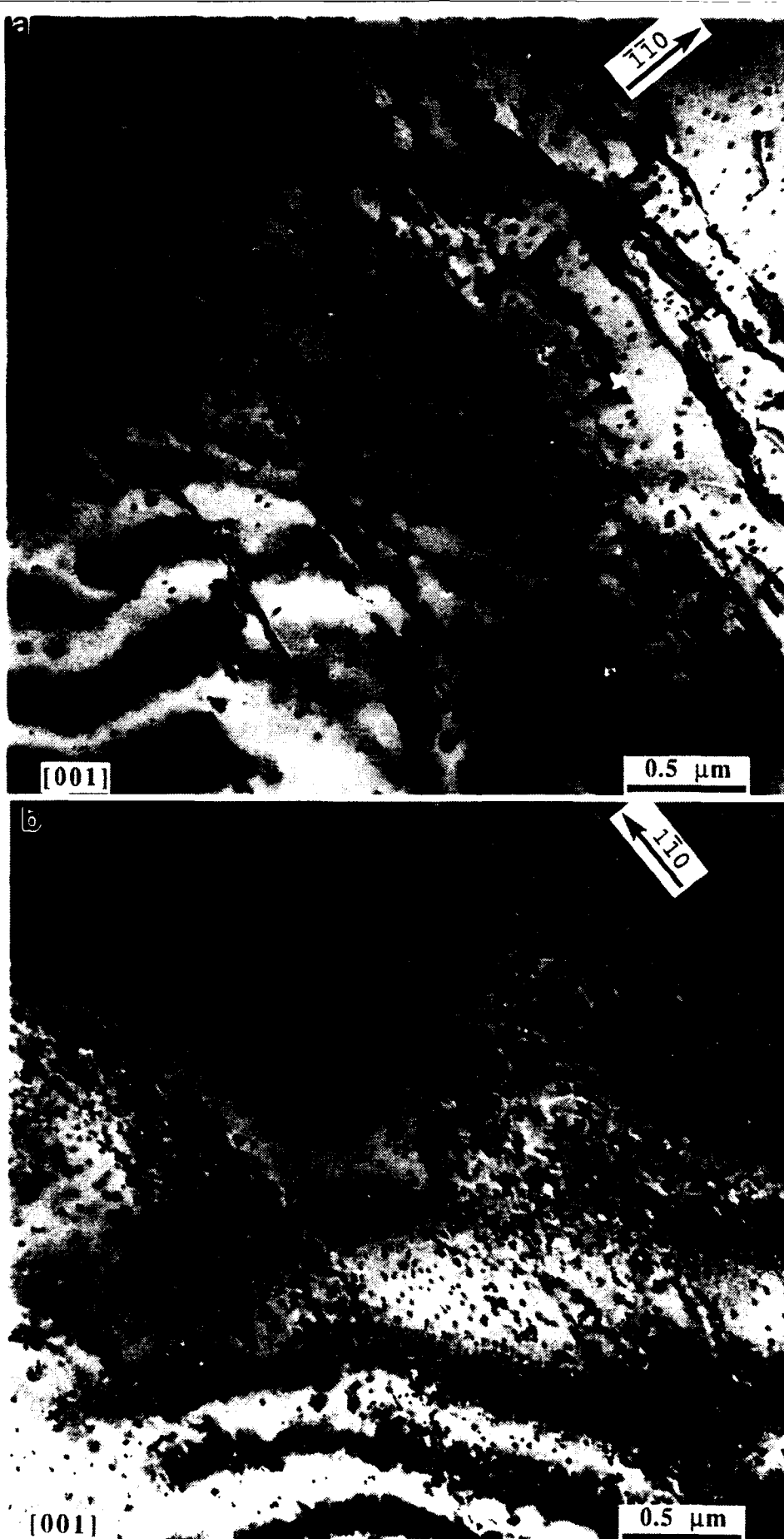


Figure 35. TEM micrographs showing $\langle 111 \rangle$ dislocations in a 0.45at% Ti/0.05at% Zr specimen tested in compression (3/1 L/D) at room temperature in the [001] orientation.

of the elastic constants, $C'=(C_{11}-C_{12})/2$, is a strong function of Ni content and softens as the Ni content is increased. This elastic constant is also a strong function of strain and can go to zero (ie. the lattice becomes unstable) for some critical strain. To determine the conditions for mechanical stability, accurate values of elastic constants, temperature derivatives of the elastic constants and the third order elastic constants are needed.

Table XIII Elastic Constants and Temperature Derivatives in NiAl Alloys at 25°C

	<u>49.4%Ni</u>	<u>62%Ni</u>	<u>62.5%Ni</u>	<u>63%Ni</u>
Density (g/cm ³)	5.964	6.590	6.644	6.657
C_L	2.88	2.84	2.85	2.84
C_{44}	1.16	1.20	1.21	1.21
C'	0.35	0.054	0.045	0.034
dC_L/dT	-4.97	-3.89	-4.72	-4.05
dC_{44}/dT	-1.35	-3.78	-3.00	-2.82
dC'/dT	-0.48	0.88	1.24	0.63
$1/C_L * dC_L/dT$	-1.73	-1.37	-1.65	-1.42
$1/C_{44} * dC_{44}/dT$	-1.61	-3.14	-2.48	-2.33
$1/C' * dC'/dT$	-1.40	16.31	27.54	18.47
Young's Mod.	0.95	0.16	0.13	0.10

Units: Elastic Constants: 10^{12} dynes/cm²

Temperature Derivatives: 10^8 dynes/cm²K

Normalized Temperature derivatives: 10^{-4} K⁻¹

The martensitic transformation temperature for the binary alloys were measured by monitoring the change in the elastic constants (C_{ij}) as a function of temperature using an ultrasonic technique. Alloys with Ni contents in excess of 61 at%Ni were found to undergo a martensitic transformation. The transformation temperatures for the binary alloys are similar to those reported by previous investigators [19,20] and are shown in Figure 2. Plots of C' and $C_L=(C_{11}+C_{12}+2C_{44})/2$ as a function of temperature for the 62 at%Ni alloy are given in Figure 36. The elastic constant C' , associated with the slow transverse mode, softens with decreasing temperature for Ni compositions in excess of 55 at%. Near the M_s , the temperature dependence becomes non-linear for the three independent elastic constants (C' , C_L , and C_{44}) and an increase in the ultrasonic attenuation is also observed. In all cases the elastic constants soften near but above M_s and a dramatic increase in attenuation is observed. The pre-martensitic strains on the (110) faces are sufficiently large to break the acoustic bond as M_s is approached. In order to study this phenomenon, follow-on experiments are planned to use techniques for direct electromagnetic generation of ultrasound.

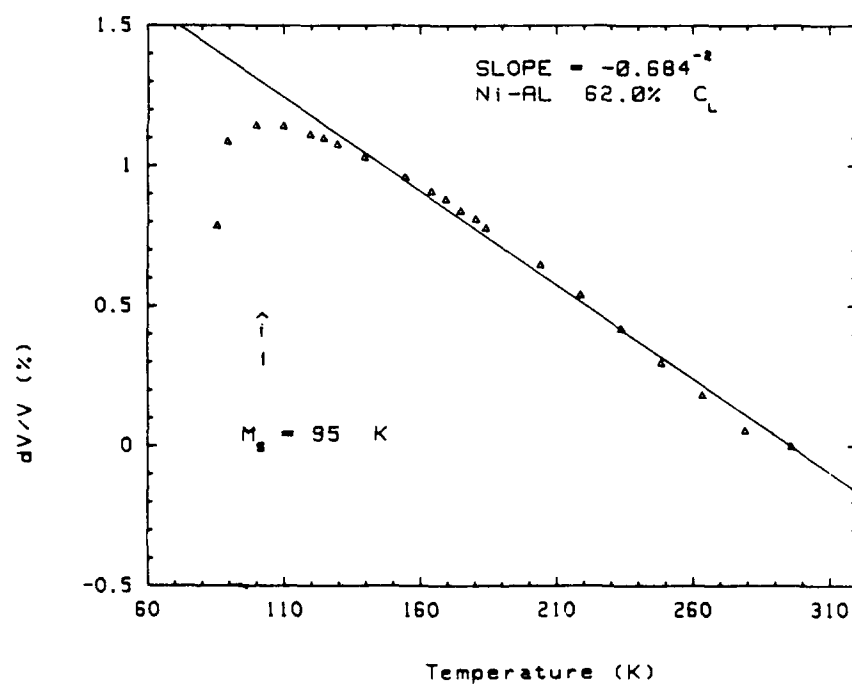
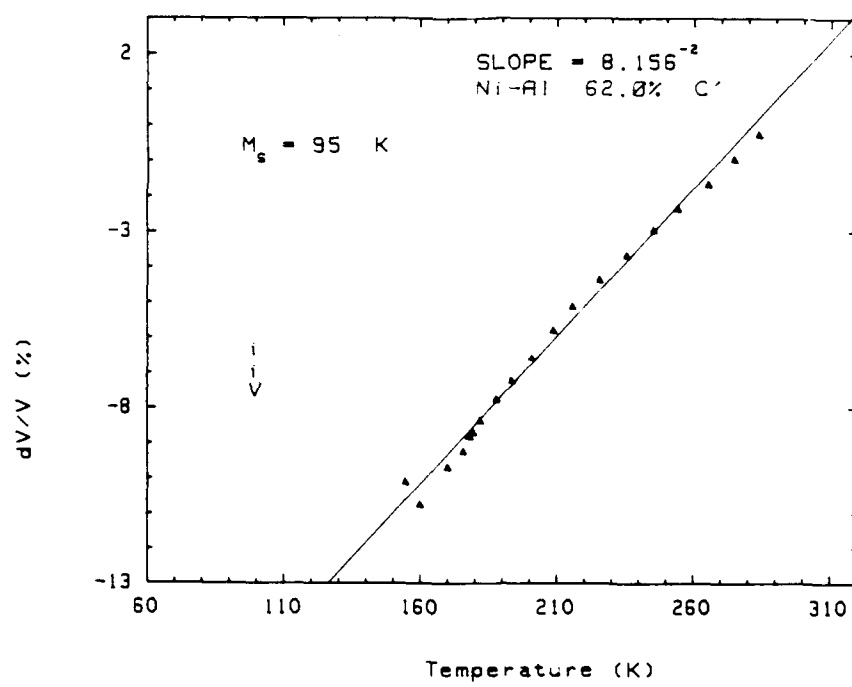


Figure 36. Plots showing the temperature dependence of the elastic constants C' and C_L in a 62 at% Ni alloy. Note the decrease in C' with decreasing temperature and the maximum in C_L at the martensite start temperature (M_s).

Compression specimens of the 49, 60, 62.5, and 63 at%Ni alloys were prepared for in situ straining experiments. In this experiment, the specimens are subjected to stress and monitored for evidence of a martensitic reaction, in order to measure with the ultrasonic technique the amount of strain required to induce the martensitic transformation (SIM) at room temperature. In the strain experiments, the ultrasound attenuation and velocity were monitored as a function of applied stress. For stress applied along [110], no changes in either the velocity or attenuation were observed for stresses as high as 1.5 bar for the C_L and C_{44} modes, while C' increases with applied stress. For stress applied along the {100} C' decreases with applied stress and is more pronounced for the 60%Ni crystal compared to the 49%Ni crystal. Unusual behavior in the attenuation is also observed. Again, C_L and C_{44} are independent of stress. Despite the observed softening of the C' with increased stress along the $\langle 100 \rangle$ direction in the 60%Ni alloy, no evidence of a stress induced martensitic transformation was observed. No measurements were made on the compositions which were found to transform thermally (62.5 %Ni, $M_S=180$ and 63 %Ni, $M_S=280K$) . These measurements are planned as a function of temperature once the pressure derivatives of the elastic constants and the third order elastic constants have been measured.

V. Discussion

A. APB Energy Calculations

The calculations indicate that the bonding between the Ni and Al first nearest neighbors is very strong in NiAl, resulting in an extremely high APB energy. The APB energy is approximately six times that of Ni_3Al , for which experimental and calculated values are in close agreement. Measurements of APB energy in NiAl have not been made, since no dissociation between superpartial dislocations (from which the APB energy is determined) has been detected. However, the high APB energy calculated for NiAl is consistent with both the high melting temperature for the compound and the dominance of the $\langle 100 \rangle$ slip vector. Since the formation and motion of dislocations with $\langle 111 \rangle$ Burgers vectors is expected to be dependent upon the degree of dissociation between $1/2\langle 111 \rangle$ the superpartials, which in turn depends directly on APB energy, it is not surprising that the $\langle 111 \rangle$ slip vector does not operate easily in this material.

Changes in stoichiometry and ternary element additions, particularly Cr, can substantially lower the calculated APB energy. However, the effectiveness of these substitutional elements is highly dependent of their positions in the lattice with respect to the APB plane. The APB energy appears to be largely controlled by the composition of the APB plane itself, so that changes away from this plane have relatively little effect. This is dramatically demonstrated by the results from calculations on non-stoichiometric alloy, presented in Table III. A 75% decrease in APB energy is calculated when Cr is substituted for Al. However, this is for the case where Cr replaces all of the Al atoms on the APB plane. A random distribution of the ternary element in the lattice is expected to be much less effective in reducing the APB energy between $1/2\langle 111 \rangle$ dislocations.

activation of slip directions other than $\langle 100 \rangle$ difficult, but reveal the difficulty of lowering the APB energy by alloying.

B. Charge Density/Bond Directionality

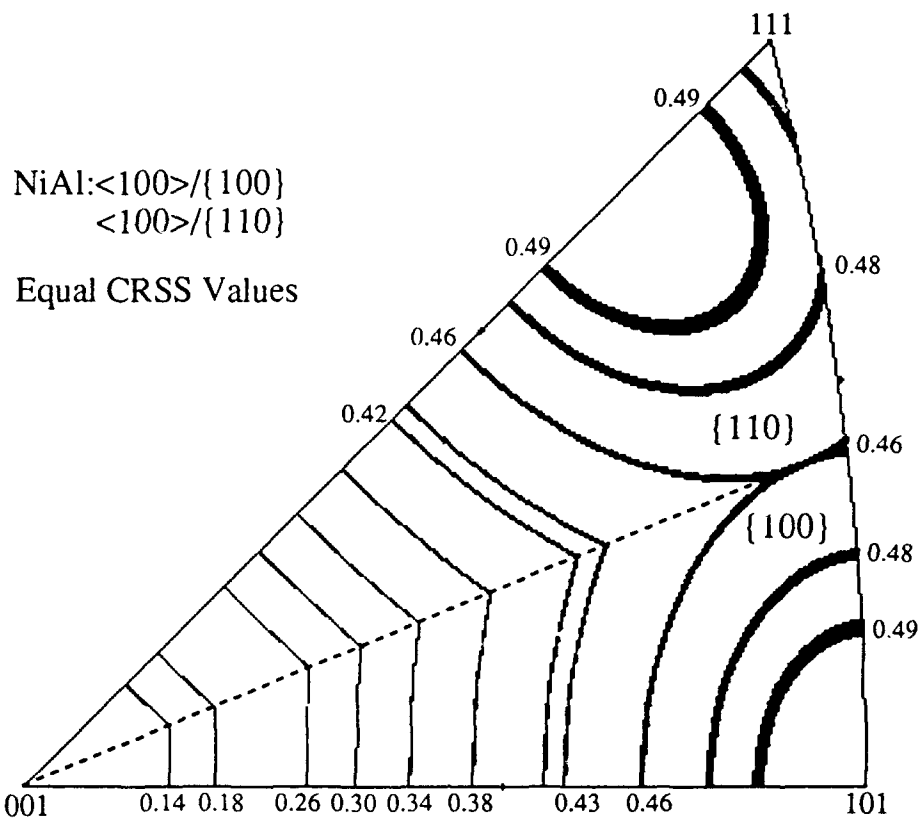
Recently, an explanation of brittle vs. ductile behavior in TiAl [4] and Ti_3Al [5] in terms of charge density distributions and associated bond directionality has been proposed. It has been asserted that pure Ti planes in these structures are highly covalently bonded, giving rise to deep Peierls valleys for dislocations whose line directions are normal to these planes. Experimental evidence has been offered which appears to support this theory. It has been shown that a high percentage of dislocations in these alloys have line directions normal to the pure Ti planes in the structure. The predominate line direction observed in the deformed microstructure is generally the least mobile, left behind by the more mobile segments.

In calculations performed as part of this study, the Ni-Al bonds were found to be both strong and directional. RuAl, a high temperature B2 compound which displays relatively high toughness and ductility was found to have much less directional, comparatively weak Ru-Al bonds. This reduction in both the directionality and strength of the nearest neighbor A-B bonds in RuAl would be expected to facilitate the formation and mobility of dislocation in this structure. It would also be expected to reduce the APB energy, thus lowering the formation energy of $\langle 111 \rangle$ superdislocations. This is consistent with the observed increase in the number of available slip systems in RuAl compared to NiAl [35].

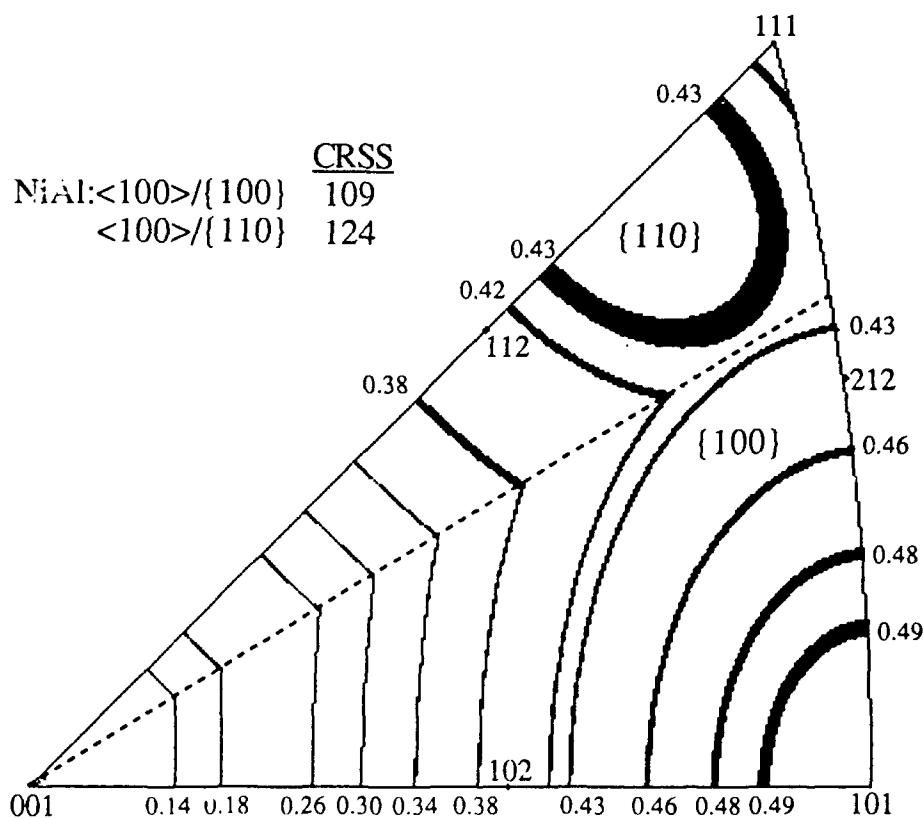
C. "Soft" Orientations

The data in Table VII clearly indicate a violation of Schmid's Law if one slip plane dominates in NiAl. If for the $\langle 111 \rangle$ orientation one assumes that the $\{110\}$ slip planes are active, a critical resolved shear stress (CRSS) of 124 MPa is calculated. If these are still active in the $\langle 110 \rangle$ oriented specimens, the value would drop to 76 MPa. It is more likely that the $\{100\}$ planes dominate in this orientation, with a CRSS of 109 MPa. This value is actually lower than that for the $\{110\}$ planes, contrary to the historical view that $\{110\}$ is the favored slip plane in NiAl at RT.

Schmid factor plots for the two slip systems, $\langle 100 \rangle / \{110\}$ and $\langle 100 \rangle / \{100\}$, are shown in Figure 37. In a), iso-Schmid lines are drawn within a standard stereographic triangle. Above the dotted line, the $\{110\}$ planes have the higher Schmid value, while the $\{100\}$ plane has greater values below the line. Thus, this line represents the boundary between regions in which $\{110\}$ and $\{100\}$ slip are expected to dominate at room temperature. In b), the Schmid values for the $\{110\}$ plane have been normalized by the ratio of CRSS values for $\{100\} / \{110\}$ planes, derived from the $\langle 110 \rangle$ and $\langle 111 \rangle$ oriented compression specimens, respectively (values given above). Note that the region in which $\{100\}$ slip is expected to dominate is significantly larger in this diagram, due to its lower CRSS value.



a



b

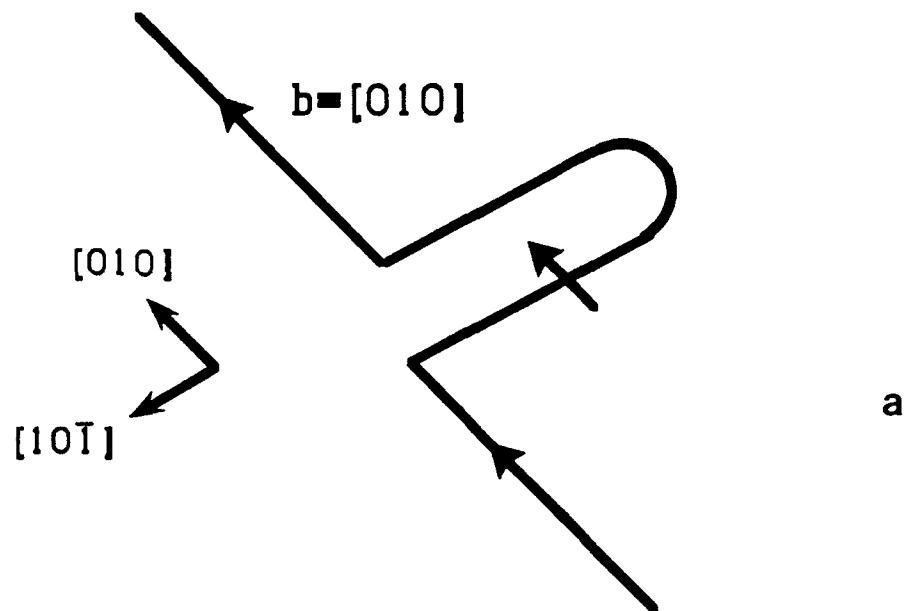
Figure 37. Iso-Schmid factor plots showing the regimes in which {110} and {100} slip planes are expected to be active for the <100> slip vector in NiAl. In (a) the actual Schmid factors are plotted, while in (b) the factors for {110} have been adjusted to reflect the higher CRSS measured for this plane.

The yield stress data from the current investigation differ significantly from those of Wasilewski et al [13]. Their study of the orientation dependence of yield stress suggests that {110} planes are favored in NiAl at RT. However, CRSS values for {110} planes calculated from their data vary significantly depending on the applied stress axis. For example, data from $\langle 111 \rangle$ and $\langle 112 \rangle$ directions, which have equivalent Schmid factors for {110} slip (0.47), give rise to CRSS values of 68 and 94 MPa, respectively. In the current investigation, $\langle 111 \rangle$ and $\langle 112 \rangle$ oriented specimens give rise to similar values of yield stress. One possible explanation for this discrepancy is the extreme sensitivity of NiAl yield stress to slight changes in stoichiometry. The geometry of the castings used in [13] (3/8" diameter rods) would necessitate using different castings, with potentially different compositions, for the various orientations. In the current study, all of the specimens were taken from the same casting.

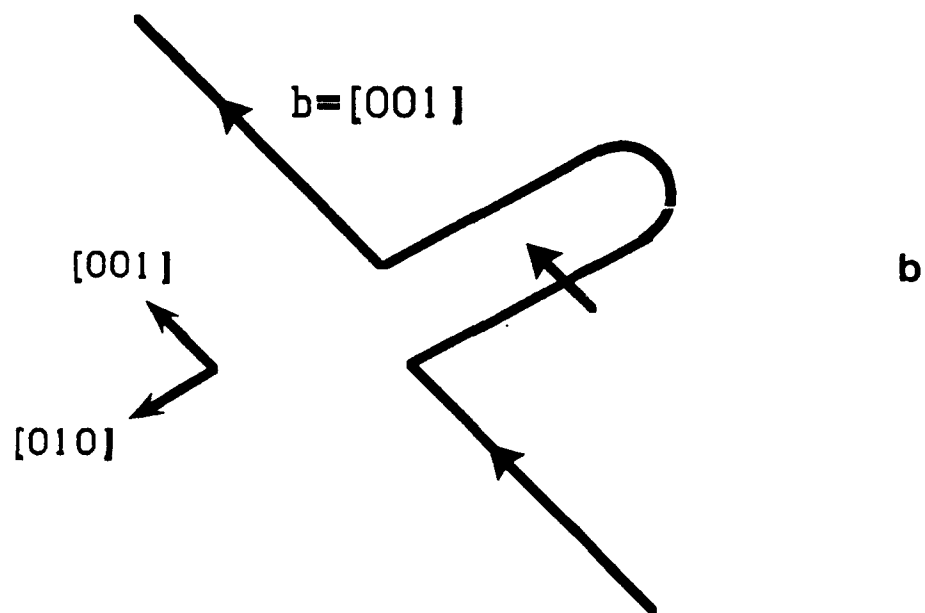
For the $\langle 111 \rangle$ oriented specimens, distinct slip traces are observed on the specimen surface, and trace analysis data are consistent with {110} slip planes. The traces are far more difficult to interpret for the $\langle 110 \rangle$ oriented specimens, although the data available do support slip on {100} planes. Line direction analysis of dislocations in the TEM was also ambiguous with regard to slip plane determination, since most of the dislocations observed appear to be debris, not lying on specific slip planes. This was particularly true for the $\langle 110 \rangle$ oriented specimen.

More information can be gained from the elongation direction of the loops. These may be formed by one of two mechanisms: double cross slip of screw dislocations to form superjogs [47], or dipole trapping of edge segments on parallel slip planes [48]. In the former, the superjogs would be expected to leave behind pinched off loops elongated perpendicular to the direction of motion of a screw dislocation on the slip plane. For the {110} plane this would be a $\langle 110 \rangle$ direction, while for the {100} plane the direction would be $\langle 100 \rangle$, as shown in Figure 38. Dipole trapping would be expected to result in loops elongated in these same directions, since they represent the edge orientation on the two respective slip planes. This mechanism also creates superjogs on the dislocations, resulting in additional loops during subsequent slip as described above. Since cross slip involves a substantial drop in Schmid factor (~30% for both orientations), this would not be expected to occur in the absence of some obstacle to slip. Therefore, it is likely that the initial formation of superjogs results from dipole trapping.

It is interesting to consider the shapes of the stress strain curves for the two soft orientations. For $\langle 110 \rangle$, a gradual yielding is observed, while for $\langle 111 \rangle$ a sharp yield point occurs, followed by a plateau. This may be understood in terms of the dislocation configuration in the unstrained material. The majority of dislocations in NiAl are prismatic loops with $\langle 100 \rangle$ line directions, since this orientation represents a minimum in the line energy for $\mathbf{b} = \langle 100 \rangle$ dislocations in Ni₃Al [49]. Therefore, the initial dislocations are edge in nature, lying on {100} planes. In order to slip on {110} planes, the observed slip plane for $\langle 111 \rangle$ oriented crystals, the dislocations must bow out and cross slip. Thus, the density of potentially mobile dislocations on {110} planes in the starting material is low, giving rise to the sharp yield point and subsequent plateau. This raises the 0.2% yield stress and, therefore, the measured CRSS value for {110} slip. If the $\mathbf{b} = \langle 100 \rangle$ dislocations in the starting material were lying on {110} planes, the yield behavior of the $\langle 111 \rangle$ specimens



slip plane=(101)



slip plane=(100)

Figure 38. Schematic depicting the origin of elongated $b = \langle 100 \rangle$ loops from screw dislocations on two different slip planes. In (a) a (101) slip plane results on loops elongated along a $[101]$ direction. In (b) a (100) slip plane results on loops elongated along a $[010]$ direction.

would be expected to more closely resemble that observed for the $\langle 110 \rangle$ specimens in which dislocations are initially lying on the preferred slip plane. Superimposing the shape of the stress-strain curve for the $\langle 110 \rangle$ specimen in the vicinity of the yield point onto the $\langle 111 \rangle$ curve gives a CRSS value of ~ 115 MPa for the $\{110\}$ slip plane. The validity of a CRSS value calculated in this manner is questionable; however, it is probably true that the CRSS for $\{110\}$ slip is much closer to that for the $\{100\}$ plane than is indicated by the macroscopic yield behavior.

D. Microalloying Effect

Only a preliminary study of this effect has been performed under this investigation. A more thorough investigation is planned in a follow-on program. Results from the current investigation do not indicate any significant change in the stress-strain behavior, other than differences in yield stress and fracture strain. The nature of yielding, orientation dependence of the yield stress, and work hardening behavior remain the same as in the stoichiometric binary compound

Resistivity data (shown in Table X) indicate that some reduction in the total point defect concentration is occurring in the 0.05%Ga alloy; however, there is not a sufficient volume of data for a definite conclusion. The evidence for a reduction in point defect concentration is stronger in the 800°C heat treated material, which displays a dramatic decrease in yield stress, as well as an increase in ductility. It is likely that these two phenomena are related. A more thorough examination of point defects in NiAl based alloys is planned for the follow-on study, in which internal friction measurements will be performed to characterize point defects and study point defect/dislocation interactions.

There is some evidence from the calculations that Mo and Ga additions may also affect the local charge density. Preliminary analysis of the charge density calculations shows that Ga considerably depletes the charge on the Al site when it is added on either Ni or Al sites. This effect is not found in NiAl with the addition of any other 3d transition metal elements. The Ni-Al bonding is expected to be weakened. Mo on the Ni sites causes anti-bonding between constituent atoms. However, Mo on Al sites has substantial second nearest neighbor bonding with Al, and modifies the original directional Ni-Al bonding.

E. "Hard" Orientation

The deformation behavior of $\langle 001 \rangle$ oriented NiAl crystals is highly temperature dependent. At room temperature or below, slip of $\mathbf{b} = \langle 111 \rangle$ dislocations has been observed in compression testing [16]. At intermediate temperatures (RT to $\sim 650^\circ\text{C}$), kinking is generally observed in compression specimens, particularly at strain rates exceeding $10^{-4}/\text{s}$. Kinking has been attributed to geometric softening following local activation of $\langle 100 \rangle$ slip systems [17,18]. Some degree of kinking was observed in compression specimens at all temperatures in the current investigation,

would be expected to more closely resemble that observed for the $\langle 110 \rangle$ specimens in which dislocations are initially lying on the preferred slip plane. Superimposing the shape of the stress-strain curve for the $\langle 110 \rangle$ specimen in the vicinity of the yield point onto the $\langle 111 \rangle$ curve gives a CRSS value of ~ 115 MPa for the $\{110\}$ slip plane. The validity of a CRSS value calculated in this manner is questionable; however, it is probably true that the CRSS for $\{110\}$ slip is much closer to that for the $\{100\}$ plane than is indicated by the macroscopic yield behavior.

D. Microalloying Effect

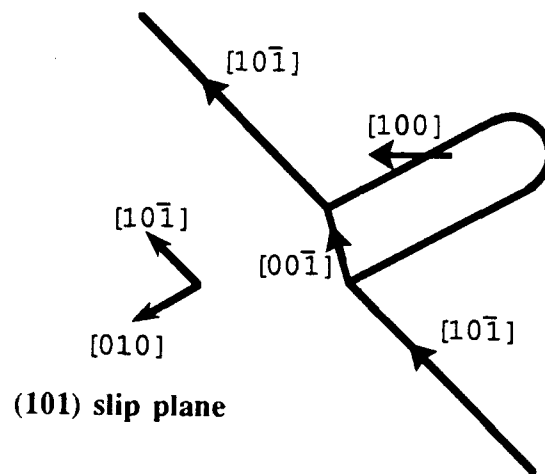
Only a preliminary study of this effect has been performed under this investigation. A more thorough investigation is planned in a follow-on program. Results from the current investigation do not indicate any significant change in the stress-strain behavior, other than differences in yield stress and fracture strain. The nature of yielding, orientation dependence of the yield stress, and work hardening behavior remain the same as in the stoichiometric binary compound.

Resistivity data (shown in Table X) indicate that some reduction in the total point defect concentration is occurring in the 0.05%Ga alloy; however, there is not a sufficient volume of data for a definite conclusion. The evidence for a reduction in point defect concentration is stronger in the 800°C heat treated material, which displays a dramatic decrease in yield stress, as well as an increase in ductility. It is likely that these two phenomena are related. A more thorough examination of point defects in NiAl based alloys is planned for the follow-on study, in which internal friction measurements will be performed to characterize point defects and study point defect/dislocation interactions.

There is some evidence from the calculations that Mo and Ga additions may also affect the local charge density. Preliminary analysis of the charge density calculations shows that Ga considerably depletes the charge on the Al site when it is added on either Ni or Al sites. This effect is not found in NiAl with the addition of any other 3d transition metal elements. The Ni-Al bonding is expected to be weakened. Mo on the Ni sites causes anti-bonding between constituent atoms. However, Mo on Al sites has substantial second nearest neighbor bonding with Al, and modifies the original directional Ni-Al bonding.

E. "Hard" Orientation

The deformation behavior of $\langle 001 \rangle$ oriented NiAl crystals is highly temperature dependent. At room temperature or below, slip of $b=\langle 111 \rangle$ dislocations has been observed in compression testing [16]. At intermediate temperatures (RT to $\sim 650^\circ\text{C}$), kinking is generally observed in compression specimens, particularly at strain rates exceeding $10^{-4}/\text{s}$. Kinking has been attributed to geometric softening following local activation of $\langle 100 \rangle$ slip systems [17,18]. Some degree of kinking was observed in compression specimens at all temperatures in the current investigation.



Slip Dissociation of a $\mathbf{b}=[10\bar{1}]$ Dislocation at a Superjog

Figure 39. Schematic showing a $\mathbf{b}=[10\bar{1}]$ screw dislocation on (101) slip plane with a $\mathbf{b}=[100]$ dipole loop extending from a superjog. Note that the $\mathbf{b}=[00\bar{1}]$ segment is also in the screw orientation and therefore can move with the $\mathbf{b}=[10\bar{1}]$ dislocation. See text for details.

occur in the presence of obstacles to slip.

Loops of this orientation could also be formed by other mechanisms including climb of $b=\langle 100 \rangle$ loops. At higher temperatures, where no yield drop is observed and the yield stresses of the two orientations approach each other, climb is believed to dominate the deformation. At the 871°C, the highest testing temperature for which TEM analysis was performed, the dislocation structure indicates that climb is strongly contributing to deformation. The evidence is particularly convincing for the tensile specimens, which were cooled rapidly following testing and display dislocation structures similar to those observed in creep studies of NiAl [42]. Dislocation climb can accommodate a compressive strain in the [001] direction by the expansion of $b=[100]$ and $b=[010]$ vacancy loops at the expense of shrinking $b=[001]$ loops. Interactions between [010] oriented segments of expanding $b=[100]$ loops would also result in dipole loops elongated along [010] and oriented on $(10\bar{1})$ planes. Some contribution to deformation by climb may be occurring at 649°C; however, the observation of bowed out $\langle 110 \rangle$ dislocations in the TEM indicates that slip is still active.

Dipole trapping or double cross-slip involving only $b=\langle 100 \rangle$ dislocations can also result in loops of the type observed, if the movement of $b=\langle 100 \rangle$ dislocations is contributing to deformation. A $b=[100]$ dislocation gliding in the screw orientation on an (001) plane would leave behind loops on or near a $(10\bar{1})$ plane elongated in the [010] direction, as observed in [110] oriented single crystals deformed at room temperature. This could occur during later stages of deformation in [001] oriented specimens. The initial movement of $b=\langle 110 \rangle$ dislocations will geometrically soften the specimen with respect to the $\langle 100 \rangle$ systems, by rotation of the lattice away from [001]. The critical resolved shear stress for $\langle 100 \rangle$ slip is significantly lower than that for $\langle 110 \rangle$. Therefore, $\langle 100 \rangle$ slip will become active even at relatively small deviations from the [001] orientation. The observation of a yield drop at intermediate temperatures in the [001] tensile specimens appears to be consistent with this mechanism. Geometrical softening has previously been proposed as a mechanism for deformation in [001] oriented tensile specimens at elevated temperatures, from the local activation of $\langle 100 \rangle$ slip, resulting from non-axial stresses around local inhomogeneities in the specimen [53]. This mechanism is similar to that responsible for kinking in [001] oriented NiAl crystals tested in compression [17,18].

The rotation from the [001] axis necessary to activate $\langle 100 \rangle$ slip may be estimated from the yield stress data. From the [001] 0.2% yield stress value of 783 MPa at 427°C, the critical resolved shear stress (CRSS) for a $[10\bar{1}]$ slip vector on a (101) plane is calculated to be 392 MPa. Testing of [110] oriented specimens, in which the $\langle 100 \rangle$ slip vector operates, results in a 0.2% yield stress value of 90 MPa at this temperature. If one assumes that slip is occurring on {100} planes in this orientation (these planes are favored over the {110}'s by a 43% higher Schmid factor), a CRSS of 47 MPa is calculated. The ratio of the CRSS values for $\langle 110 \rangle / \langle 100 \rangle$ slip is thus equal to 8.4. A rotation away from the [001] of $\sim 3.4^\circ$ would be required for the CRSS on a $\langle 100 \rangle$ slip system to be reached. The plastic strain necessary to achieve this rotation may also be calculated [54]. If a single $\langle 110 \rangle$ slip system operates, $\sim 6\%$ plastic strain would be needed.

Operation of multiple slip systems, generally observed in the specimens from this study, would result in an even higher required plastic strain. In fact, the [001] orientation is expected to be rather stable, since rotations associated with one slip system (eg. $[10\bar{1}]/(101)$) would be expected to lower its Schmid factor more rapidly than that of others (eg. $[0\bar{1}1]/(011)$) and two slip systems for which the slip direction and plane are simply exchanged (eg. $[10\bar{1}]/(101)$ and $[101]/(10\bar{1})$) have equal Schmid factors for all orientations. Thus, at 427°C, $\langle 100 \rangle$ slip would only be expected to operate after considerable plastic strain, if at all, and the observed yield drop is more likely due to the initially low concentration of $\mathbf{b}=\langle 110 \rangle$ dislocations in the material. Specimen misorientation and bending strains from misalignment may reduce the amount of plastic strain required, however, care was taken in this study to minimize these effects. Another possibility is that localized deformation within the slip bands results in high local plastic strains and associated rotations. This would be expected to result in inhomogeneous deformation, with premature failure by rapid softening within a few slip bands. This was not observed experimentally. The deformation was relatively uniform, with no gross slip bands on the gauge surface. It appears that the slip bands (seen in the 0.5% plastic strain specimen) broaden with subsequent deformation as dislocation interactions harden the interiors of the bands, resulting in a relatively uniform dislocation distribution.

At 649°C the ratio of the CRSS values for the two slip systems is much smaller and, therefore, the rotation required to initiate $\langle 100 \rangle$ slip even greater. As seen in Figure 40, the plastic strain at which the yield drop occurs actually decreases with increasing temperature. The [001] yield strength also decreases rapidly in this temperature range. Thus, it would appear that both the initial generation and the multiplication of $\mathbf{b}=\langle 110 \rangle$ dislocations is facilitated at higher temperatures.

F. Cr Effect

Results from the current investigation demonstrate that Cr sits on Al sites in the NiAl lattice, at least for the 1% Cr composition studied, in which Cr is substituted for Al in the alloy [†]. Theoretical calculations of the effect of Cr in NiAl predict a decrease in APB energy when Cr occupies the Al sites (see Table II). Thus, $\mathbf{b}=\langle 111 \rangle$ dislocations might be expected in NiAl alloys containing Cr, since a lower APB energy will promote dissociation into $1/2\langle 111 \rangle$ superpartials, with a resultant lowering of the formation energy of $\mathbf{b}=\langle 111 \rangle$ superdislocations. In fact, it appears that the addition of as little as 0.05at% Cr to NiAl promotes $\langle 111 \rangle$ slip at room temperature in favorably oriented specimens, although the results for the low Cr levels (ie. 0.2 and 0.05%) are not as clear as for the 1% Cr alloy. It should be noted, however, that the calculations were performed for an alloy composition with high amounts of Cr dissolved in the NiAl matrix (16.7at%). It has been experimentally found that the actual solubility is quite low (~1 at%). The question arises as to whether the very low levels of Cr actually present within the NiAl matrix are sufficient to produce the required reduction in APB energy, or to affect the electronic structure of

[†] It should be noted that the site occupancy may be different for other compositions (for example, if Cr was substituted for Ni in the alloy composition).

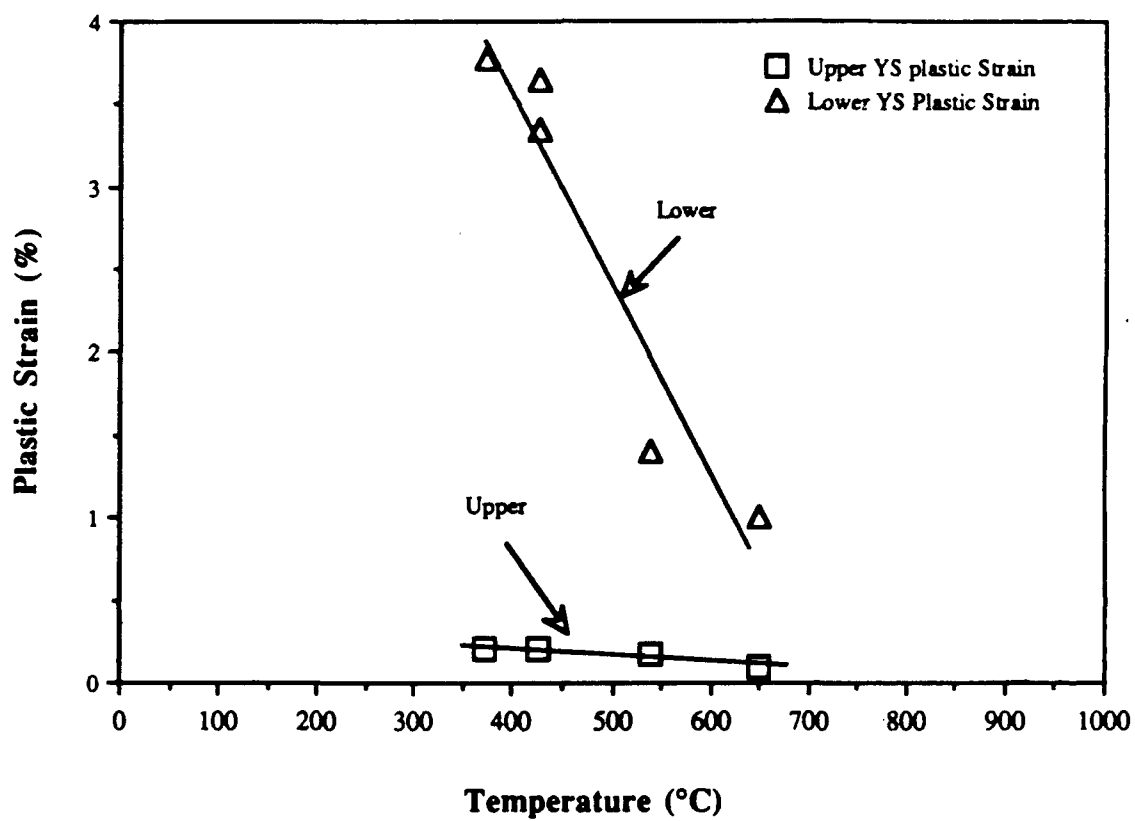


Figure 40. Plot of plastic strain values at the peak yield stress and lower yield point as a function of temperature in [001] oriented tensile specimens.

the compound in such a way as to promote the activation of the $\langle 111 \rangle$ slip system. No experimental evidence for lower APB energy, in the form of $1/2\langle 111 \rangle$ dissociation of $b=\langle 111 \rangle$ dislocations, was observed in any of the Cr containing alloys, although small separations of superpartials, beyond the resolution limits of the weak beam technique, still may be occurring.

Since neither the α -Cr precipitates (which are not present in the low Cr specimens) nor the carbides appear to promote $\langle 111 \rangle$ slip in the alloys, it is concluded that the addition of Cr results in an inherent propensity for this slip system in the alloyed NiAl matrix. Although the alloying additions do appear to promote $\langle 111 \rangle$ slip in NiAl, there is no evidence of solute softening, since the critical resolved shear stress (CRSS) for $\langle 111 \rangle$ slip is not reduced, but in many cases increased by the solute (see below). One possible explanation of the results is the differential proportional hardening of the $\langle 100 \rangle$ versus the $\langle 111 \rangle$ slip systems. In $\langle 001 \rangle$ oriented compression specimens, $\langle 111 \rangle$ slip and kinking are competitive deformation processes. As discussed above, kinking can be thought of as a $\langle 100 \rangle$ slip phenomenon. Thus, even though the alloying additions result in hardening of the $\langle 111 \rangle$ slip systems with respect to stoichiometric NiAl, if the $\langle 100 \rangle$ systems are proportionately strengthened to a greater extent, $\langle 111 \rangle$ slip would be promoted.

In Table XIV, the measured CRSS values for the alloys studied are listed for both $\langle 111 \rangle/\{112\}$ and $\langle 100 \rangle/\{001\}$ slip. It can be seen that the Ti/Zr and 1at%Cr alloys, which demonstrated a strong propensity for $\langle 111 \rangle$ slip, have significantly reduced ratios of $\langle 111 \rangle$ to $\langle 100 \rangle$ CRSS values. This is not true for the low Cr alloys, however, which display CRSS values not significantly different from that of the stoichiometric compound (ie. within the variation in the data). These alloys also displayed some increased resistance to kinking over stoichiometric NiAl; however, the evidence is not as conclusive as with the 1% Cr and Ti/Zr alloys, for which kinking was not observed in either short or long compression specimens.

Table XIV CRSS Ratios For NiAl Alloys

	CRSS (MPa) $\langle 100 \rangle/\{001\}$	CRSS (MPa) $\langle 111 \rangle/\{112\}$	Ratio $\langle 111 \rangle/\{112\}$ to $\langle 100 \rangle/\{001\}$
Stoichiometric NiAl	114	623	5.5
NiAl+1% Cr	178	721	4.1
NiAl+0.2% Cr	102	635	6.2
NiAl+0.05% Cr	100	685	6.9
NiAl+0.45%Ti+0.05%Zr	265	773	2.9

†† The data for $\langle 100 \rangle/\{001\}$ slip were obtained from $\langle 110 \rangle$ oriented specimens in which the $\{001\}$ slip plane is favored over the $\{110\}$ by a 43% higher Schmid factor. The slip plane expected to operate during kinking is $\{110\}$. Comparisons of yield stresses of $\langle 111 \rangle$ versus $\langle 110 \rangle$ specimens for NiAl shows roughly similar CRSS values for the two slip planes (see Section*), so that the proposed model should not be greatly affected.

For these more dilute alloys, it is possible that the Cr addition has decreased the Peierls stress for $\langle 111 \rangle$ dislocations; however, the CPSS may still be high due to a limited number of sources. If this is the case, local stress concentrations might be relieved by the movement of $b = \langle 111 \rangle$ dislocations, thus preventing the onset of kinking, without macroscopic softening of the $\langle 111 \rangle$ slip system. A reduction in the Peierls stress might result directly from the Cr in solution, or from the gettering of carbon from the matrix. However, no clear evidence for these effects has been found in this investigation.

G. Stress Induced Martensite

One of the problems in studying the stress induced martensite (SIM) phenomenon is that the martensitic reaction is often reversible, i.e. the martensite which forms to accommodate strain at temperatures above the martensite start temperature (M_s) reverts back to the parent phase when the stress/strain is removed. Thus, evidence for the reaction is not necessarily present in the microstructure of the deformed material. It is therefore desirable to observe the martensitic reaction during testing. Observing the martensite transformation can be accomplished by monitoring a change in the elastic constants as a function of temperature or strain with ultrasonic techniques.

The original purpose of the investigation was to determine the effect of alloying on the SIM phenomenon in NiAl alloys. Initial experiments were aimed at measuring M_s in binary alloys. Alloys with an M_s slightly below room temperature are good candidates for in-situ straining experiments because lower strains will be required to induce the transformation at room temperature. The 62.5 and the 63.0 at% Ni binary alloys were selected for the strained induced test because their measured transformation temperatures are 180K and 280K, respectively. The softening of the C' elastic constant with stress along the $\langle 100 \rangle$ direction in the 60% specimen may indicate some pre-martensitic behavior; however, no evidence for an actual transformation was observed.

Although the calculations do indicate that some ternary alloys might promote the martensitic transformation in NiAl alloys, the most potent element appears to be Ni. The Ni rich martensite compositions are not only high in density, but did not exhibit desirable strength or ductility in internally funded work performed at GEAE. For the quaternary additions investigated, the Nb/V alloy is the best candidate for a higher temperature martensite transformation. However, the concentration of Nb used for the calculations greatly exceeds its maximum solubility (~1-2 at%).

VI. Conclusions

The objective of this program was to investigate the deformation behavior of NiAl, with specific emphasis on reasons for its limited room temperature ductility and possible approaches to

increase that ductility. In addition, the program represents an attempt to use sophisticated, first principles calculations of electronic structure in crystalline solids to approach an engineering problem. The application of these calculative techniques to such complicated problems as deformation and phase stability in metallic systems has only recently become feasible, due to enormous advances in the last decade in both the theory and computational equipment.

Theoretical techniques such as those employed in this study can be used not only to help explain experimental observations, but to increase the fundamental understanding of materials behavior, predict that behavior and, ultimately, serve as a guide to future materials development efforts. Considerable information about materials can be gained from such calculations in areas such as electronic structure, phase stability, defect structures, and the influence of alloying on these properties. How these individual factors influence the complex deformation processes which lead to engineering level properties such as ductility is a more difficult question. A firm experimental base is necessary to determine the right questions to address theoretically. Also, more sophisticated calculation techniques are needed to model the complexities of deformation behavior. Therefore, continued experimental and theoretical work, both individually and in conjunction, are required.

In this program, considerable progress was made in both the theoretical and experimental areas to further the understanding of deformation in NiAl based alloys. Correlations between the calculations and experimental work were made in many areas. However, much more work will be required to bridge the gap between first principles models of electronic structure and engineering properties such as ductility.

Specific findings from the investigation are listed below.

- Charge density calculations indicate strong directional bonding and orbital hybridization between Ni and Al atoms in the NiAl structure.
- Based on first principles calculations, the APB energy, associated with $\langle 111 \rangle$ slip in NiAl, is extremely high compared to that of other aluminides (eg. FeAl, RuAl, Ni₃Al, TiAl and Ti₃Al). This is associated with strong directional bonding between Ni and Al first nearest neighbor atoms.
- The substitution of Cr on Al sites in the NiAl lattice is calculated to significantly lower the APB energy when the Cr atoms are placed on the APB plane.
- Results from the calculations on the relative stabilities of B2 and L1₀ (martensite phase) in NiAl have correctly predicted the effect of stoichiometry on the transformation. Some discrepancies have been found in other aspects of the calculations. Experimental work to monitor the martensitic reaction using ultrasonic techniques has yielded results which are consistent with those of previous investigators.
- Ternary elements that promote the martensite transformation generally must be substituted on the

Al sublattice. None of the ternary additions investigated was calculated to be as effective in promoting the martensite transformation than excess Ni in the binary compound. Two quaternary alloys were calculated to have a stable martensitic phase; however, neither composition could be made experimentally, due to improper site preference and/or solubility limits.

- Single crystal stoichiometric NiAl is not ductile when tested in tension at RT, even in "soft" oriented crystals. Plastic elongation in $\langle 110 \rangle$ oriented specimens, for example, is generally slightly less than 1%.

- Slip in NiAl tested at RT in soft orientations proceeds in the $\langle 100 \rangle$ direction on either $\{110\}$ or $\{100\}$ planes, depending on orientation. CRSS values for the two planes, calculated from the 0.2% yield stress, are approximately equal, with the $\{100\}$ plane slightly favored. CRSS values based on yield stress may be artificially high for the $\{110\}$ planes, due to the configuration of the dislocations in the untested material. In the absence of either unambiguous slip traces or dislocations clearly lying on slip planes, analysis of dislocation debris in the form of elongated loops can yield information concerning active slip planes.

- $\langle 001 \rangle$ oriented compression specimens of stoichiometric NiAl generally deform by kinking, a $\langle 100 \rangle$ slip phenomenon, when tested at RT. The use of 2/1 L/D specimens can result in the suppression of kinking and the activation of $\langle 111 \rangle$ slip.

- In the "hard" $\langle 001 \rangle$ orientation tensile specimens fail without yielding at RT. At higher temperatures ($\geq 371^\circ\text{C}$), considerable plastic flow occurs in both "soft" and "hard" orientations. Above the DBTT, plastic deformation in the $\langle 001 \rangle$ orientation results from glide of $\mathbf{b} = \langle 110 \rangle$ dislocations. At higher temperatures ($\geq 871^\circ\text{C}$), climb mechanisms become more active.

- Results from dislocation analysis in the elevated temperature $\langle 001 \rangle$ specimens stress the importance of the application of care in interpreting dislocation structures in even moderately deformed materials. Often it is primarily the debris that one is studying in these specimens, not the actual slipping dislocations. In this case, intermediate temperature deformation is found to result from the movement of $\mathbf{b} = \langle 110 \rangle$ dislocations, which leave behind $\mathbf{b} = \langle 100 \rangle$ debris.

- The addition of low levels of Cr to NiAl promotes $\langle 111 \rangle$ slip in $\langle 001 \rangle$ oriented compression specimens tested at RT. Other alloying additions can also promote this behavior. For the 1at%Cr and 0.45at%Ti+0.05at%Zr alloys, this can be attributed to proportionately differential hardening of the $\langle 100 \rangle$ versus the $\langle 111 \rangle$ slip systems. The effect of lower Cr levels is still not understood.

- At elevated temperatures, deformation mechanisms in the Cr containing alloys revert back to those of stoichiometric NiAl

- The activation of the $\langle 111 \rangle$ slip direction is not a sufficient criterion for RT ductility improvement in NiAl alloys.

References

1. R. Darolia, *J. Materials* **43** #3, 44 (1991).
2. J. H. Xu, C. L. Fu, and A.J. Freeman (to be published).
3. J.H. Xu and A.J. Freeman, *J. Mat. Res.* **6**, 1188 (1991).
4. B.A. Greenberg, V.I. Anisimov, Y.N. Gornostirev, and G.G. Taluts, *Scripta Met.* **22**, 859 (1988).
5. S.A. Court, J.P.A. Lofvander, M.H. Loretto, and H.L. Fraser, *Phil. Mag.* **59**, 289 (1989).
6. M.J. Marcinkowski, Electron Microscopy and Strength of Materials, edited by G. Thomas and J. Washburn, 333 (New York: Interscience, 1963).
7. H. Saka, M. Kawase, A. Nohara, and T. Imura, *Phil. Mag.* **50** #1, 65 (1984).
8. W.A. Rachinger and A.H. Cottrell, *Acta metall.* **4**, 109 (1956).
9. A. Ball and R.E. Smallman, *Acta metall.* **14**, 1517 (1966).
10. D.I. Potter, *Mater. Sci. Eng.* **5**, 201 (1969).
11. M.G. Mendiratta and C.C. Law, *J. Mat. Sci.* **22**, 607 (1987).
12. A. Ball and R.E. Smallman, *Acta metall.* **14**, 1349 (1966).
13. R.J. Wasilewski, S.R. Butler, and J.E. Hanlon, *Trans. AIME* **239**, 1357 (1967).
14. R.T. Pascoe and C.W.A. Newey, *Met. Sci. J.* **2**, 138 (1968).
15. R.T. Pascoe and C.W.A. Newey, *Phys. Stat. Sol.* **29**, 357 (1968).
16. M.H. Loretto and R.J. Wasilewski, *Phil. Mag.* **23**, 1311 (1971).
17. H.L. Fraser, R.E. Smallman, and M.H. Loretto, *Phil. Mag.* **28**, 651 (1973).
18. H.L. Fraser, R.E. Smallman, and M.H. Loretto, *Phil. Mag.* **28**, 667 (1973).
19. S.Chakravorty and C.M. Wayman, *Met Trans.* **7A**, 555 (1976).
20. J. L. Smialek and R.F. Hehemann, *Met Trans.* **4**, 1571 (1973).
21. K. Enami, and S Nenno, *Met Trans.* **2**, 1487 (1971).
22. A. Nagasawa, K. Enami, Y. Ishino, Y. Abe, and S. Nenno, *Scripta Met.* **8**, 1055 (1974).
23. P. Veyssiere, *Phil. Mag.* **50A**, 189 (1984).
24. R.C. Crawford and I.L.F. Ray, *Phil. Mag.* **35**, 549 (1977).
25. P.R. Monroe and I. Baker, *Scripta Metall.* **23** #4, 495 (1989).
26. H. Pops, *Met Trans.*, **1**, 251 (1970).
27. H.A. Mohamed and J. Washburn, *Met Trans* **7A**, 1041 (1976).
28. G.M. Michal and R. Sinclair, *Acta Cryst.*, **B37**, 1803 (1981).
29. A.G. Rozner, and R.J. Wasilewski, *Jour Inst of Metals* **94**, 169 (1966).
30. P. Villars and L.D. Calvert, Pearson's Handbook of Crystallographic Data for Intermetallic Phases, (American Society for Metals, Metals Park, Ohio, 1986).
31. R.J. Wasilewski, *Trans. Met. Soc.* **236**, 455 (1966).
32. R.L. Fleischer, D.M. Dimiduk, and H.A. Lipsitt, *Ann. Rev. Mat. Sci.* **19**, 231 (1989).
33. J.J. Begot, R. Caudron, P. Faivre, A. Lasalmonie, and P. Costa, *J. Physique Lett.*, **35**,

L225 (1974).

34. W. Buhrer, R. Gotthard, A. Kulik, O. Mercier, and F. Staub, *J. Phys.* **F13**, L77 (1983).
35. R.L. Fleischer, R.D. Field, and C. L. Briant, *Met Trans* **22A**, 403 (1990).
36. R.N.W. Obrowski, *Metall.* **17**, 108 (1963).
37. O. Kubaschewski, E.L. Evans, and C.B. Alcock, *Metall. Thermochem.* 4th ed. (Pergamon Press, Oxford, 1967).
38. A.E. Carlsson, High Temperature Ordered Intermetallic Alloys II, Materials Research Society Symposium Proceedings **81**, 39 (1987).
39. J. Tafto and J.C.H. Spence, *Science* **218**, 49 (1982).
40. W. Wang, R.A. Dodd, P.R. Strutt, *Met. Trans.* **3**, 2049 (1972).
41. R.R. Bowman, R.D. Noebe, and R. Darolia, Proceedings of the 2nd Annual HITEMP Review, NASA Conference Publication 10039, 47-1 (1989).
42. J. Bevk, R.A. Dodd, and P.R. Strutt, *Met. Trans.* **4**, 159 (1973).
43. Y. Y. Pan and P. Nash, to be published in Bulletin of Alloy Phase Diagrams.
44. C.C. Law, M.J. Blackburn, Final Report, June 1984-March 1987, AFWAL-TR-87-4102 (1987).
45. D.B. Miracle, S. Russell, and C.C. Law, High Temperature Ordered Intermetallic Alloys III, Materials Research Society Symposium Proceedings **133**, 225 (1989).
46. J.L. Walter, H.E. Cline, and E.F. Koch, *Trans. Met. Soc. AIME* **245**, 2073 (1969).
47. W.G. Johnson and J.J. Gilman, *J. Appl. Phys.* **31**, 632 (1960).
48. A.S. Tetelman, *Acta Met.* **10**, 813 (1962).
49. C.H. Lloyd and M.H. Loretto, *Phys. Stat. Sol.* **39**, 163 (1970).
50. A. Lasalmonie, *J. Mat. Sci.* **17**, 2419 (1982).
51. J.T. Kim and R. Gibala, High Temperature Ordered Intermetallic Alloys IV, Materials Research Society Symposium Proceedings **213**, 261 (1991).
52. D.B. Miracle, *Acta Met.* **39** #7, 1457 (1991).
53. R. Darolia, D.F. Lahrman, and R.D. Field, High Temperature Ordered Intermetallic Alloys III, Materials Research Society Symposium Proceedings **133**, 113 (1989).
54. D.K. Bowen and J.W. Christian, *Phil. Mag.* **12**, 369 (1965).

Publications Supported by this Research Effort

- R. Darolia, D.F. Lahrman, R.D. Field, and A.J. Freeman, "Alloy Modelling and Experimental Correlation for Ductility Enhancement in NiAl", High Temperature Ordered Intermetallic Alloys III, Materials Research Society Symposium Proceedings **133**, 113 (1989).
- T. Hong and A.J. Freeman, "Electronic Structure and Mechanical Properties of Intermetallics: APB Energies in Ni-Al Based Systems", High Temperature Ordered Intermetallic Alloys III, Materials Research Society Symposium Proceedings **133**, 75 (1989).
- A.J. Freeman, T. Hong, and J.H. Xu, "A Computational Metallurgical Approach to the Electronic Properties and Structural Stability of Intermetallic Compounds", in Atomistic Simulation of Materials - Beyond Pair Potentials, V. Vitek and D.J. Srolovitz eds. (Plenum Press, NY), 41 (1989).
- R. D. Field, D.F. Lahrman, and R. Darolia, "Room Temperature Deformation in "Soft" Orientation NiAl Single Crystals", High Temperature Ordered Intermetallic Alloys IV, Materials Research Society Symposium Proceedings **213**, 255 (1991).
- A.J. Freeman, T. Hong, W. Lin, and J.H. Xu, "Phase Stability and Role of Ternary Additions on Electronic and Mechanical Properties of Aluminum Intermetallics", High Temperature Ordered Intermetallic Alloys IV, Materials Research Society Symposium Proceedings **213**, 3 (1991).
- R. Darolia, "NiAl Alloys for High-Temperature Structural Applications", *J. Materials* **43** #3, 44 (1991).
- L. Zhou, P. Cornely, J. Tivisano, and D.F. Lahrman, "An Ultrasonic Study of the Martensitic Phase Transformation in NiAl Alloys", Proceedings of the IEEE Ultrasonic Symposium (1991) (to appear).
- T. Hong and A.J. Freeman, "Effect of Anti-Phase Boundaries on the Electronic Structure and Bonding Character of Intermetallic Systems: NiAl", *Phys. Rev. B* **43** (1991) (to appear).
- R. D. Field, D.F. Lahrman, and R. Darolia, "Slip Systems in <001> Oriented NiAl Single Crystals", accepted for publication in *Acta Met.*
- R. D. Field, D.F. Lahrman, and R. Darolia, "The Effect of Alloying on Slip Systems in <001> Oriented NiAl Single Crystals", accepted for publication in *Acta Met.*
- R. Darolia, D.F. Lahrman, R.D. Field, J.R. Dobbs, K.M. Chang, E. Goldman, and D. Konitzer, "Deformation and Fracture of NiAl Alloys for High-Temperature Structural Applications", Proceedings of NATO Workshop on Ordered Intermetallics (to appear).

Publications Continued...

- A.J. Freeman, "First-Principles Calculations of Phase Stability and Role of Ternary Additions in Electronic and Mechanical Properties of Aluminide Intermetallics", Proceedings of NATO Workshop on Ordered Intermetallics (to appear).
- T. Hong and A.J. Freeman, "Effect of Stoichiometry on the Structural Properties and the Electronic Structure of Intermetallics: Anti-Phase Boundary Energies in FeAl and NiAl", submitted to *J. Mat. Res.*

Presentations

- "Electronic Structure and Mechanical Properties of Intermetallics: APB Energies in NiAl", T. Hong, APS Meeting, New Orleans, March 1988.
- "Alloy Modeling and Experimental Correlation for Ductility Enhancement in NiAl", R. Darolia, D.F. Lahrman, R.D. Field and A.J. Freeman, MRS Fall Meeting, Boston MA, Nov. 1988.
- "Electronic Structure and Mechanical Properties of Intermetallics: APB Energies in Ni-Al Based Systems", T. Hong and A.J. Freeman, 1988 MRS Fall Meeting, Boston MA, Nov. 1988.
- "Promotion of a Martensitic Transformation in NiAl by Ternary Additions?", W. Lin, T. Hong, and A.J. Freeman, APS Meeting, St. Louis, March 1989.
- "A Computational Metallurgical Approach to the Electronic Properties and Structural Stability of Intermetallic Compounds", A.J. Freeman, T. Hong, and J.H. Xu, World Materials Congress, Chicago, Sept. 1989.
- "The Effect of Cr Additions on Slip Behavior in NiAl", R. Darolia, D.F. Lahrman, R.D. Field and A.J. Freeman, TMS Fall Meeting Indianapolis, Oct. 1989.
- "Computational/Theoretical Approach to the Design of New Materials", A.J. Freeman, S.P. Tang, A. Continenza, and C. Li, Intl. Conf. on Computer Appl. to Matls. Sci. & Eng., Tokyo, Aug. 1990.
- "Room Temperature Deformation in "Soft" Orientation NiAl Single Crystals", R. D. Field, D.F. Lahrman, and R. Darolia, MRS Fall Meeting, Boston MA, Nov. 1990.
- "Phase Stability and Role of Ternary Additions on Electronic and Mechanical Properties of Aluminum Intermetallics", A.J. Freeman, T. Hong, W. Lin, and J.H. Xu, MRS Fall Meeting, Boston MA. Nov. 1990.
- "An Ultrasonic Study of the Martensitic Phase Transformation in NiAl Alloys", L. Zhou, P. Cornely, J. Tivisano, and D.F. Lahrman, IEEE Ultrasonic Symposium, Waikiki, Dec. 1990.
- "Flow and Fracture Behavior of Single Crystal NiAl", R. Darolia, D.F. Lahrman, and R.D. Field, NATO Workshop on Ordered Intermetallics, Irsee, Germany, June 1991.
- "First-Principles Calculations of Phase Stability and Role of Ternary Additions in Electronic and Mechanical Properties of Aluminide Intermetallics", A.J. Freeman, NATO Workshop on Ordered Intermetallics, Irsee, Germany, June 1991.